Analysis of PWM-induced current ripples in electromagnetic actuators for position self-sensing techniques

Dissertation zur Erlangung des Grades des Doktors der
Ingenieurwissenschaften der Naturwissenschaftlich-Technischen
Fakultät der Universität des Saarlandes

von
Niklas König

Saarbrücken
2023

Tag des Kolloquiums: 7.Februar 2024
Dekan: Prof. Dr. Ludger Santen
Berichterstatter: Prof. Dr.-Ing. Matthias Nienhaus
Jun.-Prof. Dr. Gianluca Rizello
Prof. Dr.-Ing. Armin Dietz
Vorsitz: Prof. Dr.-Ing. Michael Vielhaber
Akad. Mitarbeiter: Dr. Michael Roland

Acknowledgement

This doctoral thesis has been written during my time as scientific researcher at the Laboratory of Actuation Technology (LAT) led by Prof. Dr.-Ing. Matthias Nienhaus at Saarland University. I would like to give all my gratitude to him for giving me the possibility to grow on a personal and professional level. Most of the work would have not been possible without his continuous supervision and support.

I would also like to thank Dr.-Ing. habil. Emanuele Grasso for not only being my mentor and colleague but also a friend during those years. Beside Prof. Nienhaus, he is co-author of most of my publications, and has helped me by providing fruitful advice and discussions. Special thanks also to Riccardo Mandriota for his interest in this work and detailed discussions about it.

I would also like to give gratitude to all my colleagues at the LAT for providing a creative and comfortable working environment, in particular Martin Becker, Daniel Merl, Robert Schwartz, Chris May, Klaus Schuhmacher, Stephan Kleen, Stefano Fabbri, Saeed Farzami and Jonah Vennemann for interesting discussions and enjoyable working time. Special thanks to my office mate, Carsten Klein, with whom I had a beautiful trip to South Korea and to Elke Zarbock for her ongoing patience and empathy.

Many thanks to the students that helped in this work by several student works and theses: Carsten, Charlotte, Dario, Giorgia, Iklim, Johannes K., Johannes M., Jonah, Joshua, Mira, Niccolò, Rudolf, Romain, Saeed, Stefano, Victor, and Yannik. Special thanks also to Patrick and Maximilian for their interesting discussions and news about the world of embedded systems.

Finally, I would like to thank my parents Peter and Karin for their constant love and encouragement during tough times. Without their support, all of this would not have been possible.

Abstract

Self-sensing techniques allow position estimation on electromagnetic actuators by means of electrical quantities, which can be used in sensorless applications or use-cases requiring redundancy. In standstill and low speed conditions, an estimation through the inductance is required, which is challenging due to electrical noise issues and an ambiguity that is present inside this parameter. In this work, a position self-sensing strategy for electromagnetic actuators is proposed that is based on current ripples that are inherently caused inside PWM-operated switching electronics. First, the work models these current ripples under the consideration of iron losses. Then, a position self-sensing strategy is proposed, which involves an analog integration approach. This decreases computational effort while increasing the signal-to-noise-ratio. Further considerations are made for compensating the hysteretic behavior that is visible in electromagnetic actuators. To overcome the ambiguity, a parameter that represents iron losses is estimated and allows for a unique solution of the position estimation problem. Experimental results prove the robustness and accuracy of the approach on industrial electromagnetic actuators for the usage of end-position and linear position detection. Finally, an experiment involving sensorless position control proves the bandwidth and robustness of the technique in case the estimation is used as position feedback.

Kurzzusammenfassung

Sogenannte *Self-Sensing*-Techniken erlauben das Bestimmen der Ankerlage von elektromagnetischen Aktoren über das Messen rein elektrischer Größen. Dies macht sie besonders attraktiv für den sensorlosen Betrieb oder Anwendungen mit Redundanzanforderungen. Bei Stillstand und niedrigen Geschwindigkeiten ist eine Ermittlung über die Induktivität zwingend erforderlich. Jedoch weist diese Größe Mehrdeutigkeiten auf und ist sensibel gegenüber Messrauschen. In dieser Arbeit wird eine Self-Sensing-Technik vorgeschlagen, die auf Stromwelligkeiten basiert, welche inhärent durch die PWM-Ansteuerung vorhanden sind. Hierzu wird zunächst ein mathematisches Modell von Stromwelligkeiten unter der Berücksichtigung von Eisenverlusten formuliert. Der Ansatz zur Positionsermittlung basiert auf einer analogen Integration, wodurch Rechenaufwand eingespart werden kann, während das Signal-Rausch-Verhältnis verbessert wird. Weitere Erweiterungen dienen der Kompensation hysteretischen Verhaltens. Das Problem der Mehrdeutigkeiten wird adressiert, indem ein weiterer Parameter, welcher die Eisenverluste im Aktor zusammenfasst, herangezogen wird. Experimentelle Ergebnisse an industriellen elektromagnetischen Aktoren zeigen die Robustheit und Genauigkeit des Ansatzes mit Hinblick auf eine Endlagenerkennung und einer linearen Positionsschätzung. Abschließend wird experimentell im Rahmen einer sensorlosen Regelung die Dynamik und die Robustheit der Technik gezeigt.

List of acronyms

ADC	Analog-Digital Converter
ANN	Artificial Neural Network
ASIC	Application Specific Integrated Circuit
DC	Direct Current
EMA	Electromagnetic Actuator
EMF	Electro-Motive Force
EML	Electromagnetic Levitation
FAR	Full Active Rectifier
FPAA	Field-Programmable Analog Array
FPGA	Field-Programmable Gate Array
FPU	Floating Point Unit
HF	High Frequency
HP	High-Pass Filter
IDIM	Integrator-Based Direct Inductance Measurement
LF	Low Frequency
LMS	Least-Mean Squares
LP	Low-Pass Filter
LUT	Look-Up Table
MLP	Multi-Layer Perceptron
MMF	Magneto-Motive Force
MOS	Metaloxide Semiconductor
MOSFET	Metaloxide Semiconductor Field Effect Transistor
MPI	Modified Prandtl-Ishlinskii
OR	Offset Removal
OS	Oversampling
PCB	Printed Circuit Board
PWM	Pulse Width Modulation
RLS	Recursive Least Squares
SC	Switched Capacitor
SH	Sample-and-Hold
SIDIM	Simplified Integrator-based Direct Inductance Measurement
SMC	Sliding Mode Controller
SNR	Signal-to-Noise Ratio
STSMC	Super-Twisting Sliding Mode Controller
USB	Universal Serial Bus

Contents

1 Introduction

1.1 Motivation

Electromagnetic actuation has been of interest since the discovery of electromagnetism in the early 1800s. A first prototype of an actuating electromagnet has been invented and developed by the british physician William Sturgeon in the year 1825 [1]. His first device was capable of lifting a mass of 9 pound by generating a force of 40 N. From that time on, the development of electromagnets mainly focused on increasing size and force such as the concept developed by the US-american physicist Henry in 1831 with 3400 N [2, pp. 3ff.]. With the modeling of electromagnetism conducted by Maxwell in its well-known equations, it was possible to calculate magnetic fields and resulting forces, leading to a more detailed design procedure. In particular, the german physicist Julius Dub investigated the influence of geometry properties on the force-displacement-behavior. Nevertheless, it was the german physicist Wilhelm Binder, in 1940, who was able to manipulate the force-displacement-characteristic for industrial applications. A good overview of the historical events involving in the development of electromagnets is covered in [2].

From that time on, electromagnets have been widely applied in the industrial, automotive and domestic sector. Due to their simple design, they are considered a robust and cheap actuation principle that can be produced in high volumes [2]. They can be used for generating rotational or linear motion. Since the underlying physical principle is based on the reluctance force, these electromagnetic actuators can produce only attractive forces, thus requiring a counteracting force in terms of a spring or a second electromagnet. Consequently, one or two stable positions can be achieved. A major advantage of electromagnets lies in their capability of generating forces without further mechanical transformations, thus they are considered a direct thrust actuator. This has evolved to a wide field of so-called special magnets that are only designed for their application case, thus offering unique force-displacement-characteristics with high geometrical integration into the system. [2]. Compared to other actuation principles, electromagnets generate large strokes with high forces [3, p. 47]. Due to the discussed properties and advantages of electromagnets, wide range of applications are opened. In particular, such actuators are included in hydraulic and pneumatic valves for stationary as well as mobile applications, switching relays, electromagnetic clutches and brakes. Other application scenarios include linear position actuators as well as active magnetic bearings [2, 3].

From the 1950s on, development of semiconductor devices enabled a further improvement of the overall actuator characteristics. With the help of discrete electronic circuits, it was possible to reduce actuation times, optimize current consumption in rest position and provide current as well as position control. Further inventions involved compensation of nonlinear characteristic and hysteresis effects [2]. Nevertheless, most actuators are still driven in an open loop manner with fixed supply voltage due to the actuator robustness and the cost sensitivity. Nominal voltage, number of coil windings and generated force are usually dimensioned in such a way that a suitable current, and consequently force, is generated at any position even under self-heating. In such a way, actuation is possible even under external loads and disturbances. The reduced system costs, especially due to lack of electronics and sensors, often overcome the ineffectiveness of this driving approach.

In the last years, the ongoing success of microprocessors allowed to integrate the above-mentioned functionalities in software algorithms rather than discrete electronics, thus reducing the system costs and allowing the implementation of such approaches on low-cost actuators. Despite their almost 200 years of development, linear actuation systems based on electromagnets experience of a further increase in functionality such as sophisticated control and monitoring applications [4–8], as well as soft-landing and further redundant information generation, which increases significantly functional safety [9, 10]. These important trends are further driven by digitalization strategies such as Industry 4.0, that requires Predictive Maintenance and Condition Monitoring concepts, and by further energy-saving demands, either forced by governmental restrictions or required by applications that are battery-driven.

Since it cannot be guaranteed that the position of the actuator is hold under external disturbance forces when reducing driving currents, the information on the actual actuator position is required for the implementation of those strategies. Classically, this position information is retrieved by mechanical sensors such as encoders, LVDTs (linear variable differential transformers) or, in the case of switching actuators, with mechanical end-position switches. Nevertheless, applying such sensory increases system cost, complexity and size significantly. Moreover, the coupling of an additional sensor with its wiring is cumbersome in use cases where the actuator is exposed to harsh environments such as hydraulic valves. Hence, most sensor-based solutions are placed in high-quality-applications due to cost reasons. Sensor costs are crucial in the cost-sensitive sector of electromagnets, thus representing a major challenge for implementing more sophisticated monitoring and control approaches, that result into further functional safety and reduced energy consumption. The issue of mechanical sensors has been addressed by exploiting the so-called self-sensing techniques.

1.2 State-of-the-art

In literature, both terms *sensorless* and *self-sensing* are used for actuators with the capability of position estimation. Technically, the term self-sensing seems appropriate since the actuator mechanical quantities are estimated through the knowledge of the actuator electrical quantities such as voltage and current. Thus, position and forces can be self-sensed by the actuator with its electrical subsystem. The term *sensorless* leads to confusion since anyways electrical sensors are required [11]. Since most works refer to *sensorless*, this term is also used in the following state-of-the-art.

Originally, the field of sensorless techniques was developed for rotating machinery such as synchronous and asynchronous machines [12–14]. While first approaches are based on the observation of the back-induced voltage during movement, more sophisticated approaches are based on the estimation of the actuator inductance that allows for an operation at standstill and low-speed. A particular groundbreaking research was conducted by Schroedl with his INFORM (INdirect Flux detection by On-line Reactance Measurement) technique in the late 1980s [15–17], where test pulses are injected into the machine. Further research works applied rotating [18] and alternating injection [19] as well as arbitrary injection injection schemas [20, 21].

From that time on, also sensorless techniques for electromagnetic actuators were subject for research investigations, starting from the middle 1990s. Similarly for electrical machines, these techniques can be classified based on the exploited physical effects, as illustrated by Figure 1.1. Generally, they can be separated into techniques using the estimation of the back-induced electromotive force (back-EMF), the identification of the inductance and the determination of eddy current losses inside actuators.

Estimation based on the back-EMF A large amount of works exploits the back-EMF induced during motion of the actuator rod. In such a dynamic case, the flux inside the actuator is changing. In the measured current, the derivative of the flux is visible and can be processed. A simple current peak detection was used in [22]. Other approaches integrate numerically this information in an open-loop manner in order to estimate the actual flux inside the actuator [4–6]. In order to overcome integrator drifting, also closed-loop integration [23] or a compensation of the drift [24] can be considered. More sophisticated works make usage of state observation, such as Luenberger observers [25], Kalman observers [26] and sliding mode observers [27–32]. The estimation based on the back-EMF cannot work at standstill and low speeds due to the lack of a voltage that can be measured with a good signal-to-noise ratio. While this is still sufficient for fast-switching actuators, actuators that are used for positioning require an estimation procedure that is capable of identifying the actuator position at the entire speed range.

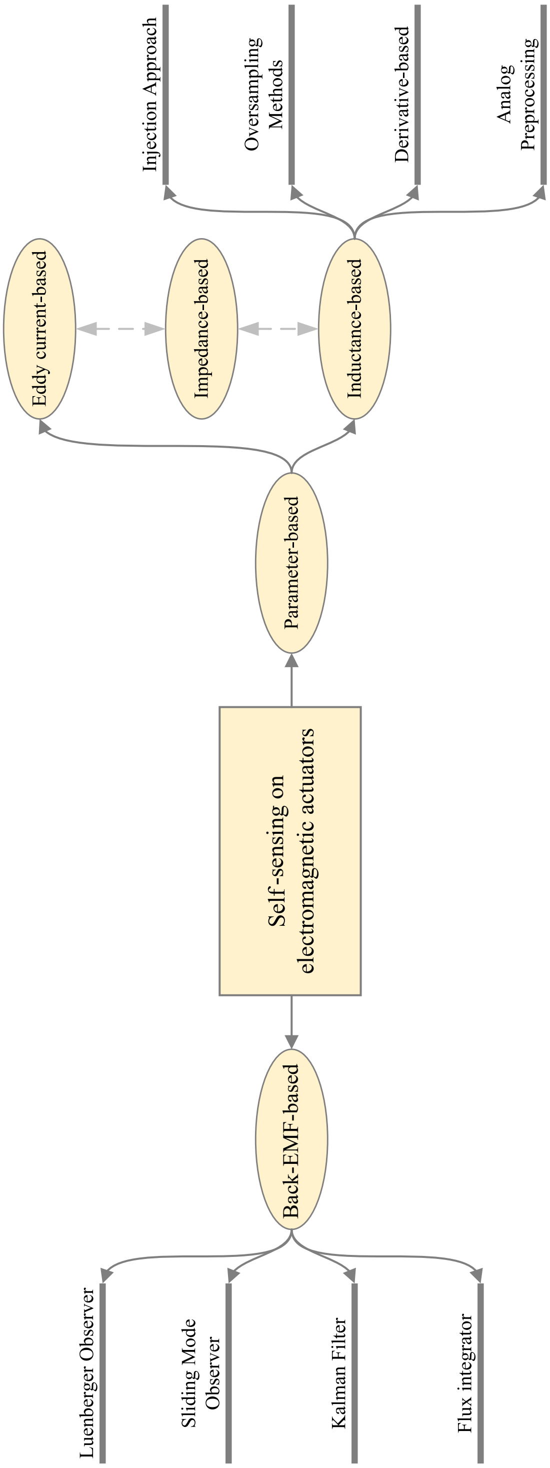

Figure 1.1: State of the art of self-sensing techniques for electromagnetic actuators.

Thus, techniques relying on observers that are based on the back-EMF are not further discussed in this work.

Estimation based on the inductance A physical quantity that can be estimated even in standstill condition is the inductance of the actuator. In particular, a persistent excitation [33] must be applied on the actuator to cause a measurable current change that allows for the estimation of the inductance. Similarly to rotating machines, injection-based approaches were developed in the works [8, 9, 32, 34–39] for solenoid actuators and in [40] for magnetic bearings. Demodulating the measured current response leads to a precise identification of the so-called incremental inductance, that is apparent under oscillating excitation. Nevertheless, injecting an additional signal into the actuator leads to several disadvantages. The choice of frequency of the injected harmonic signal leads to acoustic noise, force ripples and vibration as well as additional power losses. Furthermore, the maximum applicable driving voltage is reduced and the estimation bandwidth is considerably lower than the bandwidth of the injected harmonic signal.

Due to the mentioned disadvantages, this approach will not be followed here. Instead, techniques are discussed that rely on current ripples in those actuators. Classically, controlled electromagnetic actuators are driven by switching power electronics that are operated with a pulse-width-modulated (PWM) voltage. Such a PWM voltage represents an injection that is inherently present inside the actuator system. This voltage causes a continuous charging and decharging of the inductance which results into current ripples. The slope of the current ripple depends on the inductance, thus it can be exploited for the estimation of the incremental inductance. Such a step voltage also has the advantage of exciting the coil with several harmonics compared to a classical sinusoidal injection approach. Moreover, the PWM frequency is considerably higher than the speed of the plunger, thus an estimation with high bandwidth can be achieved. In the field of current ripple-based techniques, there exist different approaches for processing the current ripple:

1. The derivative-based approach
2. The oversampling-based approach
3. The preprocessing-based approach

Derivative-based works process the slope of the current ripple by applying two consecutive measurements and performing a numerical derivative [41–47]. By performing a derivative of the second order, also resistive voltage drops and the back-EMF during movement can be compensated. Due to the numerical derivative, the estimate usually exhibits a poor signal-to-noise ratio since current measurements are characterized by a low signal quality, especially in the case small currents are sensed with shunt amplifiers. Moreover, the switching of the power transistors distorts the measurement. Thus, strong filtering needs to be applied which leads to bandwidth reduction. In particular, the works [42, 45] amplify the current slope by applying sample-and-hold units and operational amplifiers for increasing the signal-to-noise ratio. Nevertheless, by applying a derivative, a linear shape of the current ripple is assumed that does not account for resistive effects and eddy-currents, which decreases identification performance.

Overcoming the demerits of the derivative-based approaches, oversampling approaches were invented that perform an oversampled analog-digital (AD) conversion of the current ripple within a PWM period [37, 48–53]. In such works, the sampling frequency of the AD converter is considerably higher than the PWM frequency, for instance the work [51] acquires 10000 samples per each PWM period. Based on the obtained data vector, such approaches perform a curve fitting method or a regression algorithm such as LMS algorithms in order to estimate the incremental inductance. By doing so, the exponential shape of the current ripple can be considered during the estimation process. Nonetheless, all of the above-mentioned works neglect the influence of the eddy currents. Performing an oversampled current measurement leads to significant increase in signal-to-noise ratio, thus no further processing of the inductance and position estimate is required. Nevertheless, this advantage comes with a considerable demerit of an increased sampling and computational effort, mostly leading to the usage of high-bandwidth ADCs, high performance microcontrollers with digital signal processors (DSP) or even Field-Programmable Gate Arrays (FPGAs). Such electronic components increase the cost significantly which is undesired in the cost-sensitive field of electromagnetic actuation.

The last category of techniques tries to minimize the computational effort by outsourcing the necessary preprocessing operations in analog electronics rather than software methods. Thus, a good trade-off between computational resources and obtained signal-to-noise ratio (SNR) can be obtained. Indeed, when considering PWM frequencies that are relatively high, this approach can decrease the computational burden of microprocessors. An analog preprocessing stage was presented in [54, 55], that consists of a high-pass, a rectifier and a low-pass filter. Despite its performance in estimation, this approach limits the dynamics of the estimation and of the control algorithm due to the restrictions applied by the filters. An hysteresis amplifier presented in [45] allows for a robust identification of the inductance during driving. Nevertheless, it requires the usage of a linear power electronics instead of a switching power electronics, with remarkable decrease in energy efficiency, which is undesirable in the present days. The preprocessing-based techniques have proven to provide a good SNR with decreased computational resources. Because of the ongoing performance rise in microprocessors and FPGAs, they particularly lost interest in research. Thus, oversampling approaches seemed more adequate to implement on such platforms. Nevertheless, especially in low-cost segments the usage of high-power microcontrollers and AD converters is still unwanted nowadays, leaving this research field empty for several years.

From the state-of-the-art it is visible that, for applications with standstill and low speed actuation, such as positioning applications, the incremental inductance seems the best candidate for displacement identification. Nevertheless, the incremental inductance shows a non-monotonous characteristic over the position [2], especially when the actuator operates in magnetic saturation. Thus, position estimation strategies relying on this information suffer from ambiguities [32, 39, 45, 56, 57]. This issue is addressed by using look-up tables with a prior knowledge of the moving direction of the actuator [45]. While this resembles a simple solution, it can lose its tracking during high speed operation and always needs an initialization procedure.

Estimation based on eddy currents Another physical effect that allows position identification are eddy current losses inside the plunger. The works [45, 56, 57] exhibit this physical quantity through a lumped parameter model of the magnetic circuit. In particular, iron losses are modeled as a resistor connected in parallel to the main inductance, which represents leakage. All works show that this parameter has a monotonous behavior over the entire position range and shows a remarkable sensitivity on the position. Nevertheless, all works concede that this parameter suffers from large measurement variance and poor signal-to-noise ratio, thus the work [45] avoids the evaluation of this parameter. On the other side, the works [56, 57] estimate the parallel resistance by applying a model reference adaptive system (MRAS) and verify the applicability of this physical parameter. In order to increase the SNR, information from the incremental inductance is merged with the information obtained by the parallel resistance by applying binary decision making between the operation points.

Beside the above-mentioned estimation approaches based on incremental inductance and eddy currents, there exist also techniques that fall into both categories. In particular, frequency-dependent impedance spectrums are analyzed in the works [35, 36, 45]. Thus, such approaches identify the inductance and eddy current behavior at the same time. The amplitude of the impedance changes according to the actuator position and can be therefore exploited for position estimation. Because of the demand of having different scan frequencies, those techniques resemble the injection-based approaches.

Further research works have concentrated on the modeling and compensation of the hysteretic behavior of the obtained signals. The work [58] applies a generalized Preisach model of hysteresis to the self-sensing technique. Moreover, the work [59] applies the approach by Preisach for observing the magnetic flux in the air gap and the core. Self-sensing based on the eddy current resistor is discussed in [60], where a Pseudo-inverse

Preisach model is successfully applied to compensate for hysteresis phenomena. In [9], a modified Prandtl-Ishlinskii model is used for hysteresis compensation of self-sensed proportional solenoids. Despite research goals that concentrate on modeling of magnetic materials in order to compensate undesired behavior, new works [61, 62] focus on the design of actuators for self-sensing. By applying different design methodologies and by using laminated materials, hysteresis phenomena can be dampened while the sensitivity of the inductance can be increased.

By summarizing the state-of-the-art, techniques and algorithms can be separated into five consecutive steps: underlying physical effect, measurement quantity, measurement elaboration, identification algorithm and the used model. Those five steps are common for all techniques, such as shown in Figure 1.2. In particular, the underlying physical effect depends on the flux respectively its derivative (equals back-EMF), the incremental inductance or the eddy currents. For position self-sensing, only electrical quantities such as voltage and current are measured. In case an injection approach is used or the PWM-caused current ripple is processed, the high frequency components of the current needs to be measured additionally. Those electrical quantities can be either directly measured or analogically processed (e.g. differentiation or integration) before being sampled by an ADC either by using dedicated measurement times within one PWM period or by using oversampling. Digital processing, e.g. filtering, differentiation or integration, can be applied as well. The dedicated physical parameters can be either directly calculated, observed or obtained using regression algorithms and MRAS approaches. In a further step, they can be either modeled physically by means of magnetic equivalent circuits or phenomenologically by means of Look-up-Tables (LUT) or interpolators based on polynomials and artificial neural networks (ANN). The resulting model can either be directly an (pseudo-)inverse model or can be inverted for position estimation. The modeling accuracy can be increased by considering hysteresis compensation or by applying a supervising observer, that takes the mechanical system into consideration.

1.3 Focus and scientific scope of this thesis

The state-of the-art has shown that a large amount of works focuses on techniques based on back-induced voltages for high-speed actuators with limited capability for low speeds. Instead, this thesis focuses on actuators for low-speed applications including standstill, which is typical for positioning applications. The state-of-the-art reveals that the identification through the incremental inductance promises the best results. Since the demerits of injection approaches are unwanted, techniques are preferred from the field of PWM-caused current ripples. Thus, this research work focuses on such kind of position self sensing. Its contributions are:

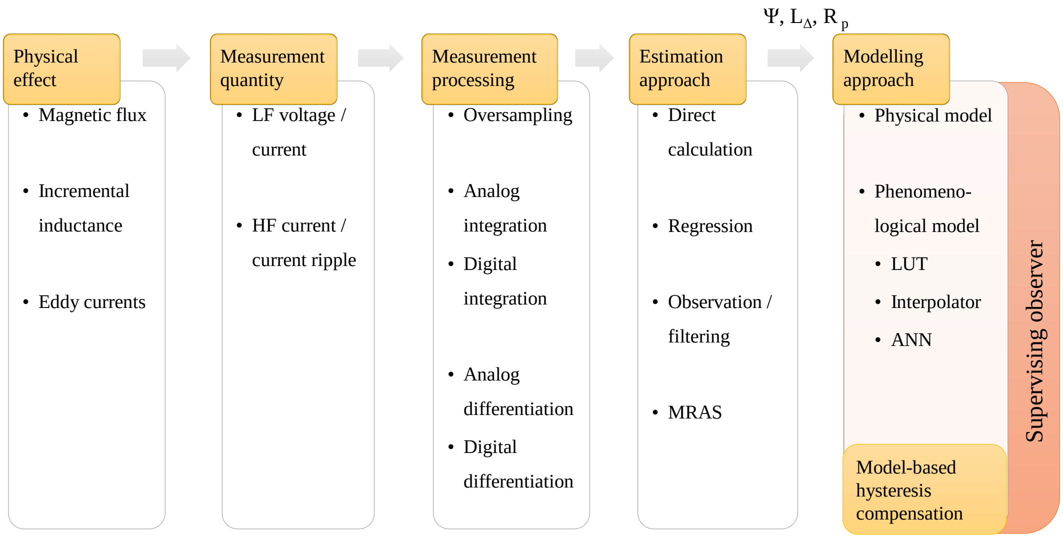

Figure 1.2: Overview on the consecutive steps necessary for implementing self-sensing strategies.

1. *Modeling and analysis of current ripples:* The successful modeling of current ripples influences the performance of the following self-sensing algorithms significantly. Basic models for current ripples without the influence of eddy currents can be derived easily by solving the first order differential equation of a RL circuit. The work [45] models also the eddy currents by means of a parallel resistor and provides a closed equation of the current ripple under PWM operation. Nevertheless, it neglects the transients that occur at PWM switching instants. Such transients lead to cusps visible in the current ripple, as reported by [40] and modeled by means of equivalent circuits and numerical simulation in [63, 64]. When not being considered, theses cusps alter the position estimation [40] and usually are avoided completely during measurement instants [51]. Nevertheless, they contain important information about the eddy currents and can be exploited for self-sensing. In literature, there is no analytical model of these cusps. This work models the current ripples under consideration of iron losses such as hysteresis and eddy current losses and provides a closed analytical equation considering the current cusps. This is done by providing a thorough analysis of the magnetic equivalent circuit of the actuator, that leads to the well known topology of series resistance, main inductance and parallel resistance. During the derivation, particular focus is laid on the complexity of the model in order to model all important effects while maintaining a computational

lightweight model. Furthermore, cases are shown where the negligence and linear approximation of the current ripple is appropriate. Results of this analysis are published in the works [65, 66].

2. *Computational lightweight self-sensing:* State-of-the-art works in the field of current ripple-based identification are mainly based on numerical derivatives or on oversampling. While in the first case the SNR is low, in the second case the SNR can be significantly improved with increased sampling and measurement effort, that is undesired in low-cost actuation. Methods based on analog preprocessing are underrepresented and were of low scientific research interest because most works assume performant microcontroller units that are not available in the low cost sector. In this work, the Integrator-Based Direct Inductance Measurement (IDIM) technique is presented that is based on analog preprocessing by means of a resettable analog integrator. First works covering the position estimation and sensorless position control on an electromagnetic actuator were published in [67, 68] and patented in [69]. Further improvements concerning the estimation bandwidth and accuracy followed in the publication [70], where a sensorless controlled levitator verified the performance of the approach. Further works considered the effects of parasitic capacitances [65] as well as eddy currents on the estimation [66]. This work presents different ways of identifying the inductance by means of the IDIM technique for different use cases such as highly dynamic operation of switching as well as linear actuators or static operation for end-position detection. The obtained methods are compared in terms of measurement and computational effort as well as bandwidth and SNR. A sensitivity analysis for measurement errors in the sensors and the analog circuit such as gain and offset errors is conducted additionally. Finally, an experimental study is shown where common oversampling approaches with different number of samples are compared experimentally to the IDIM technique in terms of computational effort and SNR.

3. *Solution to ambiguities:* As shown above, the incremental inductance shows a non-monotonic behavior over the position range that leads to ambiguities in the position estimate. Works exploit information from the eddy current resistor as further input parameter to solve this ambiguity by applying look-up-tables and binary decision making. Such binary decision has reduced accuracy and can fail when noise triggers the rule. Compared to state-of-the-art works that use observers or MRAS approaches, this work introduces an estimator based on the eddy-current resistor that is computationally lightweight and only needs 3 measurements per PWM period. The estimator is derived thoroughly and a sensitivity analysis for measurement errors is conducted. Instead of a binary rule data fusion, an artificial neural network

with a lightweight structure is used for information merging. Results show the accuracy of the proposed approach. The approach for solving the ambiguities in the position estimation is published in the work [66].

4. *Hysteresis compensation:* For accurate modeling and self-sensing of electromagnetic actuators, the hysteretic nature of the ferromagnetic material has to be taken into consideration. Despite its importance, the state-of-the-art shows few works addressing this topic. In this work, a Modified Prandtl-Ishlinskii model is used for the identification and compensation of the hysteretic behavior of the incremental inductance. Since the incremental inductance shows a butterfly hysteretic characteristic, that cannot be modeled by classical hysteresis models, a transformation is shown that provides a link to the classical B-H-curve. During derivation of the approach, special attention is paid on the computational lightness of the approach in order to support the main aspect of the IDIM technique. Experimental results on an electromagnetic actuator are shown with and without hysteresis compensation and are discussed in terms of computational effort as well as accuracy. The presented approach is published in [71].

The work is structured as follows. First, a small introduction into ferromagnetism and loss principles in ferromagnetic materials is given in Chapter 2. Then, a thorough mathematical analysis is conducted with the help of magnetic and electrical equivalent circuits. Chapter 2 ends with the analysis and discussion of the response of such a system to a PWM voltage. Chapter 3 introduces and analyzes the self-sensing approaches such as the IDIM technique and the eddy current based estimation and presents different ways of modeling the position-dependency of the obtained physical parameters. Chapter 4 explains in detail the analog circuit that is necessary for the implementation of the IDIM technique and describes the test-bench used for the experiments. Experiments for three use cases are shown, including: the end position detection for a switching actuator with monotonous characteristic, the linear position detection on a switching actuator with hysteresis compensation and the end-position detection on a switching actuator with non-monotonous behavior. Additionally, a comparison is conducted with a common oversampling strategy in terms of SNR and computational effort under variation of the number of samples. Chapter 5 provides a further outlook for sensorless control applications. In particular, a sensorless controlled levitator is shown and experimentally verified. Finally, conclusions are drawn and an outlook for future work is given in Chapter 6.

2 Modeling of electromagnetic actuators under PWM-excitation

This chapter provides a mathematical model of electromagnetic actuators that is needed for the common understanding of this thesis. Beside a basic model, a short introduction into the nonlinear hysteretic behavior of ferromagnetic materials is given as well as the main losses inside such actuators during dynamic operation such as iron losses. The understanding of these physicals effects allows for a modeling of the electrical and magnetic behavior of the actuator under PWM operation. The model uses equivalent circuits in the magnetic and electrical domain that allow analyzing the actuator with the well-known circuit theory [72]. Based on this analysis, a general model of PWM-caused current ripples inside electromagnetic actuators is derived that is able to serve as a physical and mathematical background for the self-sensing techniques explained in Chapter 3.

2.1 Mathematical model of electromagnetic actuators

A generic electromagnetic actuator is composed of a current-driven coil, a plunger made of ferromagnetic material and a ferromagnetic back-iron serving as magnetic flux guide, as shown in Figure 2.1. Between the movable plunger and its end-stop, an air gap with variable length x is present. For sake of simplicity, in this section, losses will be neglected and the permeability of the ferromagnetic materials is treated linearly with a relative permeability $\mu_r \to \infty$.

In general, electromagnetic actuators serve as energy converter between electrical and mechanical energy. The energy conversion takes place by exploiting magnetic energy as supporting energy type [2]. Magnetic energy can be easily stored in inductors with ferromagnetic cores. Nevertheless, the conversion between these energies undergoes losses that results into energy that is dissipated as heat. Due to its large time constant, the heat as well as its transfer through the thermal subsystem will not be considered in this analysis. Figure 2.2 summarizes the electrical and mechanical subsystem in a schematic. Only the simplified model will be considered here, where the magnetic domain behaves linearly and without any losses. Therefore, its influences can be neglected for calculating

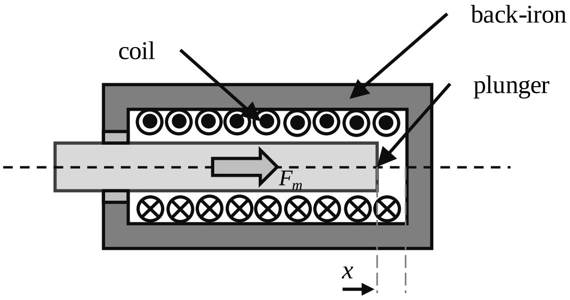

Figure 2.1: Cross-section of a general-purpose solenoid actuator, adopted from [71].

the mechanical response to an electrical excitation. This simplification allows for a simple analytical calculation of the actuator force. Nevertheless, for the analysis of the actuator response under PWM operation, the nonlinearity as well as the occurring losses of the electromagnetic materials need to be considered, as later will be done in Section 2.2.

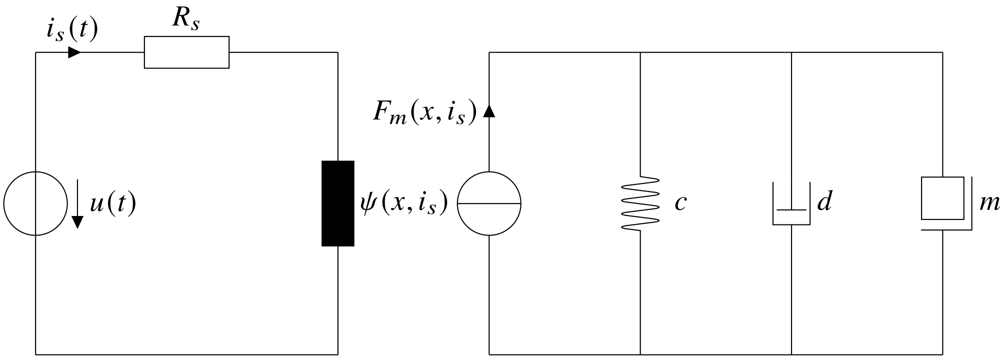

Figure 2.2: Electrical and mechanical subsystem of an electromagnetic actuator, adopted from [2].

By analyzing Figure 2.2, the mathematical model of the electrical and mechanical subsystems can be obtained [2] as:

$$u(t) = R_s \cdot i_s(t) + \frac{\partial \psi(x, i_s)}{\partial t}, \tag{2.1}$$

$$m \cdot \frac{\partial^2 x(t)}{\partial t^2} = F_m(x, i_s) - c \cdot x(t) - d \cdot \frac{\partial x(t)}{\partial t}, \tag{2.2}$$

with R_s being the series resistance of the coil, Ψ being the flux linkage as well as u and i_s being the applied voltage and current, respectively. The parameters of the mechanical system are the mass m, the spring stiffness c as well as the viscous damping coefficient d. The magnetic energy stored in the actuator can be calculated as:

$$W_{mag} = \int_0^{i_s} \psi(x, i_s) di_s. \tag{2.3}$$

Assuming no conversion losses, the force $F_m(x, i_s)$ of the electromagnetic actuator can be calculated from the magnetic energy by means of the principle of virtual work as [2]:

$$F_m(x, i_s) = -\frac{\partial W_{mag}}{\partial x} = -\frac{\partial}{\partial x} \int_0^{i_s} \psi(x, i_s) di_s. \tag{2.4}$$

The force is always directed in such a way that the air gap and therefore the magnetic energy present in the air gap is minimized. This phenomenon is known as Maxwell stress along surfaces between different permeabilities and under the name of reluctance force [73, p. 58]. In particular, neglecting losses and assuming a linear magnetic material, the force yields to:

$$F_m(x, i_s) = -\frac{\partial}{\partial x} \left(\frac{1}{2} L_s(x) \cdot i_s^2 \right) = -\frac{1}{2} \frac{\partial L_s(x)}{\partial x} \cdot i_s^2, \tag{2.5}$$

where L denotes the static inductance, which will be explained in detail in Section 2.2. This well-known quadratic current law reflects the fact that the reluctance force that is generated is independent on the current sign and, consequently, the force is always attracting. That is the reason why an external force is needed for pulling the plunger back to its original position. The opposed forces can be provided by gravity, springs or by an additional actuator in the protagonist-antagonist-principle. The term $\frac{\partial L_s(x)}{\partial x}$ can be adopted based on the design choices and, thus, several force-displacement-characteristics can be achieved. In literature, hyperbolic curves are considered for switching actuators with or without a decreased force before the end stop as well as flattened or partially linear curves for proportional actuators [2]. A deeper insight into the force generation mechanism as well as constructive adaptations can be found in the literature [2, 73, 74].

2.2 Properties of magnetic materials

In the previous section, the magnetic characteristic of the ferromagnetic materials has been considered purely linear and with infinite magnetic permeability for the sake of simple analytical calculations. Nevertheless, for an accurate modeling of electromagnetic actuators, the nonlinear and hysteretic behavior of these materials has to be considered. For a basic understanding, a short review about the basics of magnetism will be provided here before specifying the quantities that are used for modeling. For a more detailed introduction into the topic, reference is made to [2, 75–77].

In general, the electrons of an atom have an orbital moment and a spin moment. Due to their electrical charge and their movement, they generate magnetic moments, in particular an orbital magnetic moment and a spin magnetic moment [75]. In some materials, both moments compensate each other, leading to a total moment being null. Such materials are considered as diamagnetic [2]. In other materials, these moments superimpose, leading to an increased magnetic moment. If an external field is applied, this field rotates the atomic moment in the direction of the external field. Such materials are considered as paramagnetic [2]. In elements such as iron, nickel and cobalt as well as some alloys, there is a direct interference between the atomic moments of different atoms due to the existing crystal lattice. In such materials, there is a spontaneous magnetization without any external field. The material itself is separated into domains which are completely magnetized until saturation. These domains are called Weiss domains [75]. In case of a complete superposition, the material is considered as ferromagnetic, while in case of a partially superposition they are considered as ferrimagnetic [2]. Materials with completely opposing atomic moments are called antiferromagnetic [2]. Based on the material law with a magnetic permeability μ, which links the magnetic field strength H and the magnetic flux density B

$$B = \mu H = \mu_0 \mu_r H, \tag{2.6}$$

a relative magnetic permeability μ_r can be defined. The permeability in air is denoted as μ_0 and amounts to $4\pi \cdot 10^{-7} \frac{Vs}{Am}$. Different materials are characterized by their value of μ_r [75]:

- diamagnetic $\mu_r < 1$
- para- and antiferromagnetic $\mu_r > 1$
- ferro- and ferrimagnetic $\mu_r \gg 1$.

In engineering, only ferri- and ferromagnetic materials are relevant [2]. In particular, for solenoid actuators and electrical machines, only ferromagnetic materials are usually considered due to their high saturation densities, and consequently, high forces [75].

In ferromagnetic materials, the magnetization process is highly nonlinear and hysteretic. It follows different magnetization stages, that are shown in Figure 2.3. First, the material consists of countless Weiss domains, whose magnetic moments are statistically distributed. The sum of all moments amounts to zero (Initial state). Between the domains there exists the so-called Bloch walls, where the magnetization reverses. Such a Bloch wall is only 100-1000 atoms thick [2]. Beside the walls, there exists also crystallographic defects in the material [75], which mainly depend on the material quality and the manufacturing process [75]. When an external field is applied, the Weiss domains are expanding in the field direction, thus the Bloch walls are moving (state 1). This process is still reversible [75].

When a Bloch wall hits a defect, the Bloch wall is blocked because it needs more energy to jump over the defect. When the field is further increased, the Bloch wall has enough energy to jump over the defects (Barkhausen jump), which leads to a further increase of the Weiss domains (state 2) [75]. The wall movement at this state is irreversible and leads to the existence of magnetic hysteresis. At a final state, the atomic dipoles are rotating into the field direction until the material is fully in saturation (state 3) [75]. This rotation is reversible. The magnetization effects are temperature-dependent and usually disappear when a certain Curie-temperature T_C is exceeded [75].

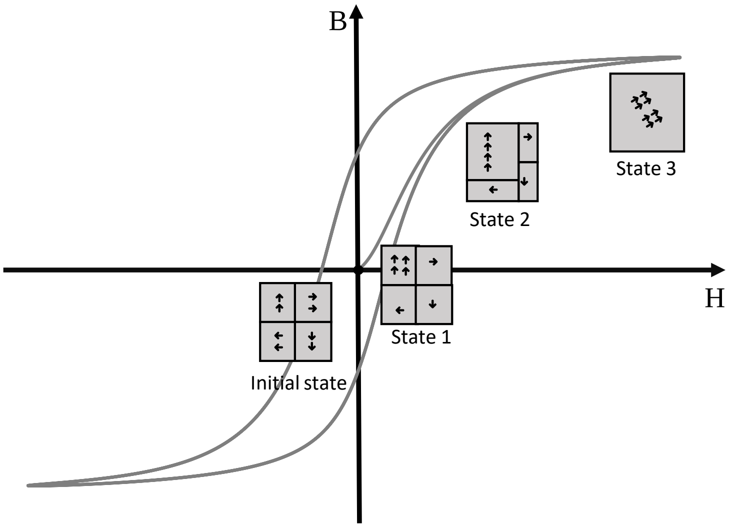

Figure 2.3: Magnetization process in ferromagnetic materials, adopted from [2, p. 41].

The so-called B-H-curve visualizes the hysteretic nonlinear dependence of the magnetic flux density B over the magnetic field strength H and is shown in Figure 2.4 for common ferromagnetic materials. Due to the nonlinear hysteretic behavior, the magnetic permeability is dependent on the actual working point (H_0, B_0) on the B-H-curve and is subject to several definitions. For instance, the static permeability used for DC calculations, can be formulated by the slope of the secant line between the origin and the actual working point [2, p. 26]:

$$\mu_s = \frac{B_0}{H_0}. \tag{2.7}$$

Electromagnetic actuators are normally driven by switching voltages such as PWM voltages, leading to the induction of current ripples. Those currents ripples partially charge and discharge the inductor. This driving scheme excites the magnetic material at the small signal range. Therefore, the behavior of the B-H-curve and its characteristic needs to be regarded in this small signal range. Operating in the small signal range,

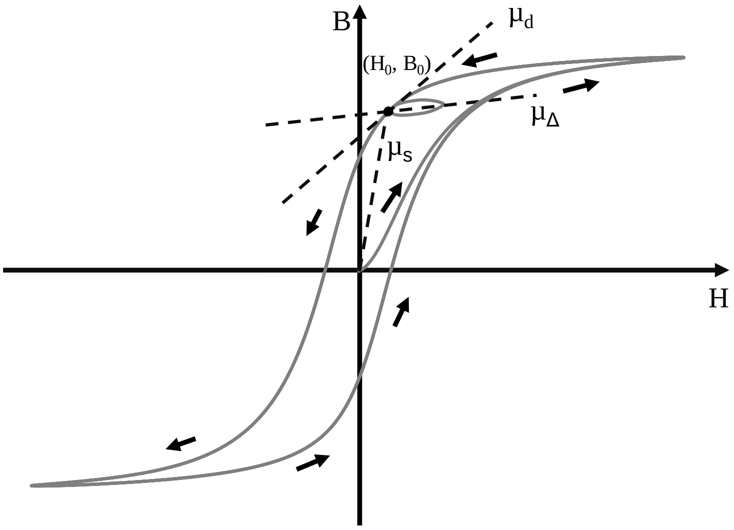

Figure 2.4: B-H characteristic of a softmagnetic material with minor loops and definition of different permeabilites, adopted from [77, p. 4].

under an applied bias field, leads to the creation of minor loops, whose mean permeability during one minor loop is described by the incremental permeability [77]

$$\mu_\Delta = \frac{B_\Delta}{H_\Delta}|_{(H_0,B_0)}. \tag{2.8}$$

For a infinitesimal small excitation, the reversible inductance can be obtained:

$$\mu_{rev} = \frac{B_\Delta}{H_\Delta}|_{(H_0,B_0)} \qquad \text{for } B_\Delta \to 0 \text{ and } H_\Delta \to 0. \tag{2.9}$$

On the other hand, there exists the so-called differential permeability, which results in the definition of the differential reluctance and inductance. The differential permeability can be defined by the tangent of the B-H-curve in the actual working point on the major loop [2, p. 26]:

$$\mu_d = \frac{\partial B}{\partial H}|_{(H_0,B_0)}. \tag{2.10}$$

Note that in an anhysteretic material, where no loops occur, the incremental, reversible and differential inductance resemble each other. Since in this chapter the current ripples generated by a PWM voltage are considered in hysteretic materials, the incremental inductance will be considered in the following sections.

Magnetic flux paths with sources and materials of different permeability can be easily visualized and analyzed by means of the circuit theory. This is possible due to the analogy between the electrical domain and the magnetic domain [72]. In particular, the magnetic flux ϕ is driven by the magneto-motive force (MMF), which is calculated in the scalar case as $\theta = \oint H dl$. In a current-driven coil with a certain number of windings N, the so-called flux linkage can be obtained as [2, p. 18]:

$$\psi = N\phi, \tag{2.11}$$

and the MMF can be simplified to

$$\theta = N \cdot i_s. \tag{2.12}$$

As described by the Hopkinson law, a magnetic flux flowing through a piece of magnetic material leads to a magnetic voltage drop $v = \int_{l_1}^{l_2} H dl$ between two coordinates l_1 and l_2:

$$v = \mathcal{R} \cdot \phi. \tag{2.13}$$

The so-called magnetic reluctance resembles a resistive component in the flux path and can be modeled as [2, p. 23]:

$$\mathcal{R} = \frac{l_{eff}}{\mu A_{eff}}, \tag{2.14}$$

with l_{eff} and A_{eff} describing the effective geometry of the piece of magnetic material with a certain relative magnetic permeability μ_r. Thus, the static reluctance in the working point (H_0, B_0) yields to:

$$\mathcal{R}_s = \frac{l_{eff}}{\mu_s A_{eff}}, \tag{2.15}$$

and the static inductance that is used for energy and force calculations as:

$$L_s = \frac{\psi}{i_s} = \frac{N^2}{\mathcal{R}_s}. \tag{2.16}$$

For the small signal excitation resulting into minor loops, the so-called incremental reluctance can be obtained as:

$$\mathcal{R}_\Delta = \frac{l_{eff}}{\mu_\Delta A_{eff}}, \tag{2.17}$$

and consequently the incremental inductance as:

$$L_\Delta = \frac{\Delta\psi_\Delta}{\Delta i_s} = \frac{N^2}{\mathcal{R}_\Delta}, \tag{2.18}$$

where ψ_Δ denotes the magnetic flux amplitude inside the minor loop. Thus it is possible to obtain the characteristic of the incremental inductance over the current, as depicted in Figure 2.5. In contrast to the classical hysteretic phenomena of the B-H-curve, the incremental inductance shows a so-called butterfly hysteresis [77, p. 541].

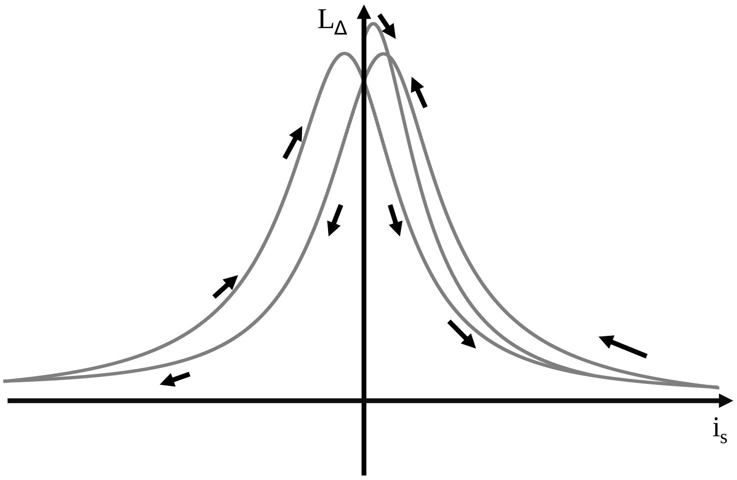

Figure 2.5: Behaviour of the incremental inductance, adopted from [77].

The mathematical representation of the incremental reluctance resembles the linearized behavior of the reluctance around its actual working point (H_0, B_0), therefore it can be considered as a small signal reluctance. This approach of linearizing non-linear components is commonly known from electrical circuit theory and, therefore, reluctance networks can be treated by applying linear network analysis tools [72].

The Maxwell equations link the B-H characteristic of the ferromagnetic material with the $\psi - i$ characteristic of the electromagnetic actuator by geometrical quantities. Thus, in the scalar case, it can be obtained:

$$\psi = N \cdot \phi = N \cdot \int_A BdA, \tag{2.19}$$

$$i_s = \frac{1}{N} Hl_{eff}. \tag{2.20}$$

Another common approach is the usage of the magnetic voltage v and the magnetic flux ϕ in analogy to the electrical quantities voltage and current. This allows for an intuitive modeling of magnetic circuit by means of classical electrical circuit theory. Consequently, the B-H-curve can also be presented in the form of an $\phi - v$ characteristic:

$$\phi = \frac{1}{N} \cdot \psi = \int_A B dA, \tag{2.21}$$

$$v = N \cdot i_s. \tag{2.22}$$

2.3 Losses inside magnetic materials

As explained in Section 2.1, not only the nonlinear hysteretic behavior of the ferromagnetic material increases the complexity of the actuator model, but also the presence of energy losses during operation. Moreover, beside decreasing the efficiency during operation, such losses also influence the self-sensing capability of the actuator since the loss phenomena overlap with the desired signals. As discussed later, it can be seen that losses inherently influence the shape of the current ripple under PWM operation, thus altering the information that is required for a position estimate with high accuracy, sensitivity and repeatability. Since this chapter deals with the electromagnetical subsystem of the actuator, only losses occurring in this part of the system will be discussed, while, for instance, mechanical losses due to friction are not considered here.

Losses in the electromagnetic part can be divided into static and dynamic losses. In the case of static losses, the thermal loss in the coil due to Joule effect [78, p. 33] is the most significant contribution. During modeling, this resistive loss is represented by the serial resistance R_s of the coils. Moreover, leakage fluxes due to parasitic air gaps are also present and reduce the available magnetic flux that link with the plunger and the air gap. Dynamic losses inside magnetic materials are summarized under the name iron losses and generally consist of [78, p. 461]:

- Eddy current losses
- Hysteresis losses
- Residual losses

Eddy current losses occur when a varying magnetic field passes an electrically conducting material. Due to electromagnetic induction, a voltage is induced in the material that generates electrical currents. Those currents generate a magnetic field that overlap with the original field. Due to energy considerations, that are formulated in the Lenz rule, the generated field is opposed to the original field, leading to losses during dynamic operation [78, p. 462]. Instead, hysteresis losses are caused by the hysteretic nature of magnetic materials. Due to its presence, there exists a difference in the amount of energy that is needed to polarize and depolarize magnetic materials. This difference in energy is dissipated as heat during dynamic operation [78, p. 462]. While hysteresis and eddy current losses predominate the dynamic losses in ferromagnetic materials, a small amount of losses can be considered as residual losses that are caused by microscopic physical effects [78, p. 462]. Its amount will be neglected here, since they only occur at lower flux densities and in materials with low electrical conductivity, where eddy currents can be neglected [79].

Due to the loss separation principle, those losses that usually are strictly physically linked to each other, can be modeled and analyzed separately [80, p. 12]. In literature, many works focus on different modeling approaches for different applications. While the discussion would clearly expand the scope of the thesis, only two common approaches are mentioned: the frequency-based power calculation approach and the differential equation approach. The interested reader is directed to the fundamental book on ferromagnetism [77] and magnetic hysteresis [80] for further details. The first widely-applied approach analyzes the amount of losses under a purely sinusoidal excitation and therefore yields to the calculation of power losses in dependence of the used frequency [78, p. 461]. One of the most adopted models is the Steinmetz law: $P = \eta \cdot B^{1.6} \cdot f + e \cdot B^2 \cdot f^2$ [77, p. 782], that empirically models the power losses P as a function of the frequency f by means of the coefficients η and e. While this approach is sufficient for power loss analysis in applications with fixed frequencies (e.g. net applications with 50 Hz), it is inappropriate in the discussed case of dynamic modeling where transients occur due to the usage of PWM voltages. Thus, approaches based on differential equations are used that are able to analyze dynamic behavior. The differential equations stem directly from the Maxwell equations. In fact, all dynamic losses have in common that they can be considered proportional to the change of the magnetic flux density $\frac{dB}{dt}$ [81]. Being transformed to the Laplace domain, those equations allow a linear analysis of the involved losses. In particular, the loss elements can be interpreted as components in magnetic equivalent circuits [82] that can be analyzed by tools known from circuit theory [72].

Eddy current losses

Eddy currents occur when the magnetic flux flowing through electrically conducting material is varying over time. Most magnetic materials usually exhibit a certain electrical conductivity σ_{el} beside their magnetic properties. This is especially the case in electromagnetic actuators when steel alloys are used and, due to cost reasons, a lamination of the steel is avoided. In the case of the discussed actuators, the back-iron and especially the plunger realized as solid metal core, is affected. In general, the induced voltage u_{ind} yields to:

$$u_{ind}(t) = -\frac{\partial \psi(t)}{\partial t}, \tag{2.23}$$

while the resulting eddy current i_{ed} amounts to:

$$i_e(t) = \frac{u_{ind}}{R_e} = -\frac{\sigma_{el} A_{eff}}{l_{eff}} \frac{\partial \psi(t)}{\partial t}, \tag{2.24}$$

with A_{eff} and l_{eff} being the effective area and length of the body where the eddy currents occur. The eddy current itself generates a magnetic field that is opposed to the original field, thus reducing the total magnetic voltage v_{tot}:

$$v_{ed}(t) = N \cdot i_{ed}(t), \tag{2.25}$$

$$\begin{aligned} v_{tot}(t) &= v_{orig}(t) + v_{ed}(t) \\ &= \mathcal{R}\phi(t) - \frac{\sigma_{el} N^2 A_{eff}}{l_{eff}} \frac{\partial \phi(t)}{\partial t}. \end{aligned} \tag{2.26}$$

Since we analyze the fluxes within the material, only one winding exists [2, p. 168], and consequently we can set $N = 1$. As shown by [2, p. 169], the term in front of $\frac{\partial \phi(t)}{\partial t}$ can be seen as magnetic inductance in the magnetic path:

$$\mathcal{L}_e = \frac{\sigma_{el} A_{eff}}{l_{eff}}, \tag{2.27}$$

The definition of magnetic inductance resembles the definition of the electrical conductance of the piece of magnetic material. There is an analogy between electrical and magnetic inductances: while the electrical inductance delays the rise of current in response to an electrical voltage step, the magnetic inductance delays the rise of flux when a magnetic voltage step is applied. This resembles the physical effect of eddy currents, as Equation 2.26 indicates a first-order system in the magnetic domain.

For a voluminous piece of material exhibiting eddy currents, such as the plunger, the skin effect needs to be taken into account. In particular, this effect causes a delay in the generation of eddy currents between the inner layer and the outer layer of the piece of magnetic material. Since the inner parts are affected by the sum of the original field and the fields that are generated by the eddy currents in the outer layers, the magnetic flux slowly propagates itself into the inner part of the body. According to the work of [72], the propagation of eddy currents in a voluminous body can be modeled by a cascade of magnetic low-pass filters consisting of magnetic reluctances and magnetic inductances, as shown in Figure 2.6. By increasing the number of low-pass filters n_c in the cascade, the model accuracy can be increased.

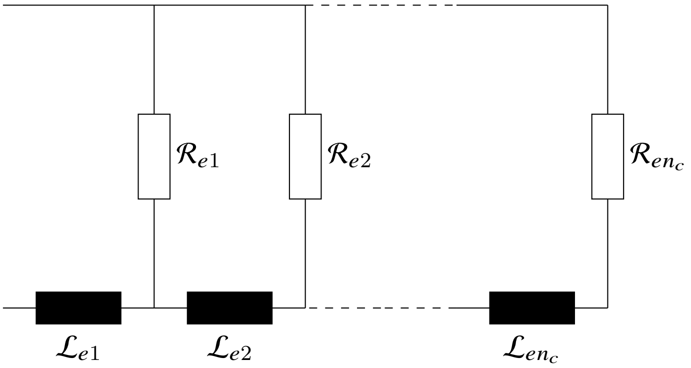

Figure 2.6: Magnetic equivalent circuit of a voluminous piece of magnetic material, where eddy currents are induced, adopted from [2, p. 169].

Hysteresis losses

As mentioned in Section 2.2, magnetic materials exhibit a hysteretic behavior, that not only introduces a nonlinearity with memory in static operation, but also leads to losses during dynamic operation. In particular, the magnetic energy that is needed for polarizing the material, and therefore charging the inductance, is different than the energy that is needed for decharging [78, pp. 457ff.]. This difference in energy is dissipated as heat and is referred to as hysteretic loss [78, p. 461]. While such losses occur mainly during travel on the major B-H-curve, the driving of the actuator by a PWM voltage excites minor loops of the B-H-curve at every PWM instant, leading to continuous hysteretic losses. For a correct analysis of the current ripple under PWM operation, the effect of such hysteretic losses inside a minor loop is studied. Similarly to the eddy current losses, most approaches for analyzing hysteretic losses are based on a frequency-based energy model [78, p. 461], which does not sufficiently represent the case of transients caused by PWM voltages and their resulting current ripples [82]. Therefore, for elaborating the eddy current losses in such cases, the dynamic hysteresis model from Chua [83] based on differential equations is considered. In general, the Chua model describes a hysteretic system as

$$\frac{dy(t)}{dt} = g[x(t) - f(y(t))], \tag{2.28}$$

with a generic hysteresis between the system input $x(t)$ and the system output $y(t)$. The function $g()$ is called dissipation function while the function $f()$ is referred to as restoring function [83], which already indicates the energy considerations behind this model. Both functions are monotonic and differentiable functions, which need to be identified based on the given hysteresis [83]. In the case of the discussed magnetic hysteresis, the input can be considered as flux density $\boldsymbol{B}$ while the output can be considered as magnetic field strength H. As seen in Equation 2.22, B and H can be replaced by the magnetic voltage v and the magnetic flux ϕ respectively, yielding to:

$$\frac{d\phi(t)}{dt} = g[v(t) - f(\phi(t))]. \tag{2.29}$$

In particular, the studied hysteresis losses occur in a minor loop with a relatively small amplitude that is caused by the current ripple. It therefore can be considered to take place in the small signal range. Thus, Equation 2.29 with its functions $g()$ and $f()$ can be linearized around the working point with the quantities ϕ_0, $\frac{d\phi}{dt}|_{\phi_0}, v_0$ [84, p. 111] on the hysteresis curve under the assumption of differentiability of the functions $g()$ and $f()$. An implicit function h can be defined for the given system:

$$h\left(\phi(t), \frac{d\phi(t)}{dt}, v(t)\right) = \frac{d\phi(t)}{dt} - g(v(t) - f(\phi(t))) = 0. \tag{2.30}$$

A small deviation can be defined around the working point as:

$$\Delta\phi(t) = \phi(t) - \phi_0, \tag{2.31}$$

$$\Delta\frac{d\phi(t)}{dt} = \frac{d\phi(t)}{dt} - \frac{d\phi}{dt}|_{\phi_0}, \tag{2.32}$$

$$\Delta v(t) = v(t) - v_0. \tag{2.33}$$

This function can be linearized around the working point by applying the Taylor series and truncated at the second order:

$$\begin{aligned} h(\left(\phi(t), \frac{d\phi(t)}{dt}, v(t)\right) &= h\left(\phi_0 + \Delta\phi(t), \frac{d\phi}{dt}|_{\phi_0} + \Delta\frac{d\phi(t)}{dt}, v_0 + \Delta v(t)\right) \\ &\approx h\left(\phi_0, \frac{d\phi}{dt}|_{\phi_0}, v_0\right) + \frac{\delta h}{\delta\phi}(\phi_0)\Delta\phi + \frac{\delta h}{\delta\frac{d\phi(t)}{dt}}\left(\frac{d\phi}{dt}|_{\phi_0}\right)\Delta\frac{d\phi(t)}{dt} + \frac{\delta h}{\delta v}(v_0)\Delta v. \end{aligned} \tag{2.34}$$

By inserting the state variables and by calculating the partial derivatives, it can be obtained:

$$h\left(\phi(t), \frac{d\phi(t)}{dt}, v(t)\right) \approx h\left(\phi_0, \frac{d\phi}{dt}|_{\phi_0}, v_0\right) + \Delta\left(\frac{d\phi}{dt}\right) - \frac{\delta g}{\delta v}(v_0 - f(\phi_0))\Delta v + \frac{\delta g}{\delta f}\frac{\delta f}{\delta\phi}(\phi_0)\Delta\phi. \tag{2.35}$$

Because the function $h()$ is implicit, all terms containing $h()$ can be set to zero and the linearized system can be obtained:

$$\frac{d\tilde{\phi}(t)}{dt} = \underbrace{\frac{\partial g}{\partial v}(v_0 - f(\phi_0))}_{\tilde{\beta}_0} \tilde{v}(t) - \underbrace{\frac{\partial g}{\partial f}\frac{\partial f}{\partial \phi}(\phi_0)}_{\tilde{\beta}_1} \tilde{\phi}(t). \tag{2.36}$$

The linearized state variables are denoted with a tilde. This linearized system with the working-point-dependent parameters $\tilde{\beta}_0$ and $\tilde{\beta}_1$ can be described as:

$$\tilde{\beta}_0 v(t) = \frac{\partial \phi}{\partial t} + \tilde{\beta}_1 \phi(t). \tag{2.37}$$

and the resulting magnetic voltage drop can be divided into:

$$v(t) = \underbrace{\frac{1}{\tilde{\beta}_0}}_{=\mathcal{L}_h} \frac{\partial \phi}{\partial t} + \underbrace{\frac{\tilde{\beta}_1}{\tilde{\beta}_0}}_{=\mathcal{R}_h} \phi(t), \tag{2.38}$$

consisting of an inductive part and a resistive part. Thus, similarly to eddy current losses, hysteretic losses can be represented by a series connection of a reluctance with a magnetic inductance, such as shown in Figure 2.7. They also cause a delay behavior on the magnetic flux.

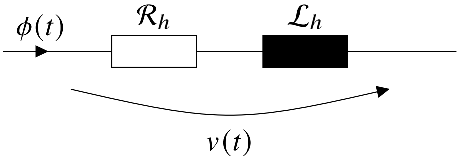

Figure 2.7: Magnetic equivalent circuit of a piece of magnetic material exhibiting hysteretic losses.

2.4 Magnetic equivalent circuit for electromagnetic actuators

With the discussed material characteristics as well as losses in the previous sections, it is possible to expand the simple electromechanical model from Section 2.1. In this section, the magnetic subsystem of the electromagnetic actuator will be derived by means of a magnetic equivalent circuit. A basis for this equivalent circuit is Figure 2.1 that shows the basic construction that is common to all reluctance-based electromagnetic actuators. The magnetic flux path inside a solenoid actuator can be modeled as depicted in Fig. 2.8 [51]. Back-iron and plunger are made of a soft-magnetic material with a specific B-H-characteristic and also exhibit eddy currents and hysteresis losses. It is convenient here to summarize reluctances and magnetic inductances into magnetic impedances that are denoted with $\mathcal{Z}$. Thus, there exists a magnetic impedance $\mathcal{Z}_b$ for the back-iron and an impedance $\mathcal{Z}_p$ for the plunger. Since not all the flux lines close over the air gap, a reluctance $\mathcal{R}_l$ considers all the leakage fluxes inside the actuator which do not lead to a generated force. The air gap is represented by a position-dependent reluctance which can be calculated as [2, p. 77]:

$$\mathcal{R}_x(x) = \frac{x}{\mu_0 A_{eff}}. \tag{2.39}$$

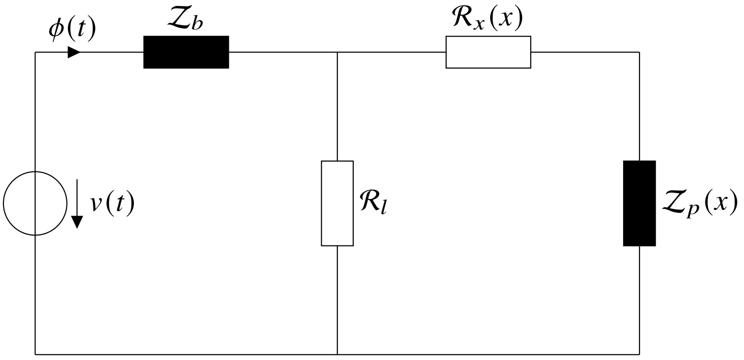

Figure 2.8: Magnetic equivalent circuit of a solenoid actuator, adopted from [51].

With the help of Section 2.2, the generic magnetic impedances $\mathcal{Z}_b$ and $\mathcal{Z}_p$ are modeled by considering the approximated loss models. The nonlinear characteristic of the back-iron material is presented by the incremental reluctance $\mathcal{R}_{\Delta b}$ in the actual working point of the actuator. Usually, the back-iron itself has a small thickness or is made up of laminated iron sheets. Thus, eddy currents occur, but are not so significant that the skin effect needs to be taken into account [72, pp. 72ff.]. Therefore, the effect can be considered by a single magnetic inductance called $\mathcal{L}_{eb}$. Similarly, the hysteresis loss can be modeled by a magnetic reluctance $\mathcal{R}_{hb}$ and magnetic inductance $\mathcal{L}_{hb}$. This leads to the total impedance of:

$$\mathcal{Z}_b = \mathcal{R}_{\Delta b} + s\mathcal{L}_{eb} + \mathcal{R}_{hb} + s\mathcal{L}_{hb}. \tag{2.40}$$

Similarly, the plunger exhibits the characteristic of the incremental permeability, which is here summarized into the magnetic reluctance $\mathcal{R}_{\Delta p}$. The plunger represents a voluminous piece of soft-magnetic material, where eddy currents are affected by the skin effect. In order to model the impedance $\mathcal{Z}_p$, the magnetic cascade model shown in Fig. 2.6 is used and represented as a total impedance $\mathcal{Z}_{ep}$:

$$\mathcal{Z}_p = \mathcal{R}_{\Delta p} + \mathcal{Z}_{ep} + \mathcal{R}_{hp} + s\mathcal{L}_{hp}. \tag{2.41}$$

In particular, the air gap reluctance as well as the magnetic components of the plunger exhibit a position-dependency. Usually, back-iron and plunger are made of soft-magnetic materials with a high permeability ($\mu_r >> 1$) and, therefore, only a negligible amount of flux lines short-circuits the air gap. Thus, the leakage reluctance can be neglected during the following calculations:

$$\mathcal{R}_l \rightarrow \infty. \tag{2.42}$$

Because of the negligence of the leakage flux, all circuit components appear in a serial connection and can be summarized. As visible in Fig. 2.9, magnetic reluctances and magnetic inductances are summarized and named generically for sake of simplicity. Since the reluctance $\mathcal{R}_0$ includes the position dependent air gap reluctance, it is also dependent on the position. Thus, all components are position-dependent and can be used for self-sensing.

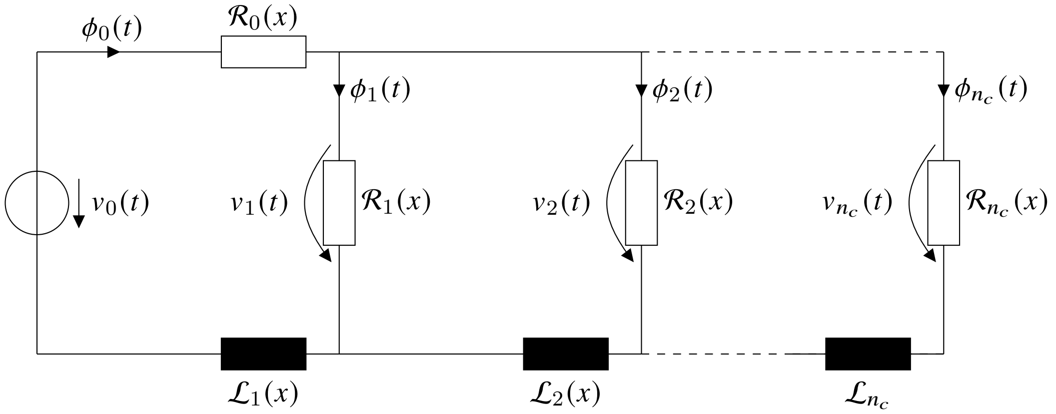

Figure 2.9: Simplified magnetic equivalent circuit of a solenoid actuator.

In order to facilitate the mathematical analysis of the obtained circuit, the Laplace transformation is applied with the Laplace value called s. This method is used in classical circuit theory and analysis. In the following calculations, all initial conditions are set to zero. All transformed quantities are denoted with capital letters and in dependence of s. For sake of brevity, the position dependence is not shown in these equations. In particular, the total flux $\Phi_0(s)$ can be calculated by the Kirchhoff law as:

$$\Phi_0(s) = \sum_{j=1}^{n_c} \Phi_j(s), \tag{2.43}$$

where the index j stands for the actual flux branch in Figure 2.9. By applying the Hopkinson law, the magnetic voltage can be expressed as:

$$V_0(s) = \mathcal{R}_0\Phi_0(s) + s\mathcal{L}_1\Phi_0(s) + \mathcal{R}_1\Phi_1(s). \tag{2.44}$$

For sake of simplicity, the externally given magnetic voltage is denoted as $V_0(s)$. The voltage over each i-th low-pass element can be expressed as:

$$V_i(s) = \Phi_i(s)\mathcal{R}_i = V_{i-1}(s) - s\mathcal{L}_i \sum_{j=i}^{n_c} \Phi_j(s). \tag{2.45}$$

This yields to the calculation of the magnetic flux per each branch as:

$$\Phi_i(s) = \frac{V_{i-1}(s) - s\mathcal{L}_i \sum_{j=i}^{n_c} \Phi_j(s)}{\mathcal{R}_i}. \tag{2.46}$$

Thus, the flux per each branch can be calculated in a recursive way as:

$$\Phi_i(s) = \begin{cases} \dfrac{V_0(s) - \mathcal{R}_1\Phi_1(s)}{\mathcal{R}_0 + s\mathcal{L}_1} & for \qquad i = 0 \\ \dfrac{V_{i-1}(s) - s\mathcal{L}_i \sum_{j=i}^{n_c} \Phi_j(s)}{\mathcal{R}_i} & for \qquad 1 \leq i \leq n_c \end{cases}. \tag{2.47}$$

The obtained model allows analyzing the response of the magnetic subsystem in all of its flux branches when an input in form of a magnetic voltage is applied. In particular, transients can be modeled, that allows to study the influence of PWM on the magnetic subsystem and, consequently, on the electrical current.

2.5 Electrical equivalent circuit for electromagnetic actuators

In the previous section, the magnetic equivalent circuit was modeled with the magnetic voltage as input and the magnetic flux as output. Nevertheless, the magnetic field strength respectively the magnetic voltage is created by means of a coil with a certain number of windings N. The coil serves as an electromagnetic transducer that links the magnetic quantities to the electrical ones. In particular, the interconnection happens through the electromotive force (EMF) $\frac{d\phi(t)}{dt}$ on the electrical side and the magnetomotive force (MMF) $v(t) = Ni_s$ on the magnetic side. By considering the number of windings N, the flux linkage can be derived:

$$\Psi_0(s) = N \cdot \Phi_0(s), \tag{2.48}$$

while the relation between coil current and magnetic voltage can be written as:

$$V_0(s) = N \cdot I_s(s). \tag{2.49}$$

Thus, a transfer function can be defined that describes the dynamic behavior between coil current and flux linkage:

$$\frac{\Psi_0(s)}{I_s(s)} = \frac{\Gamma(s)}{\Upsilon(s)}, \tag{2.50}$$

consisting of a generic polynomial in s named $\Gamma(s)$ for the nominator and $\Upsilon(s)$ for the denominator. With this transfer function it is possible to transform electrical quantities into magnetical ones and vice verse.

The electrical circuit is depicted in Figure 2.10 and consists of the series resistance R_s, that accounts for copper resistance, a parasitic capacitance C_p, that models capacitive coupling between the windings, and the EMF source. The influence of the series resistance is considerable due to a high number of windings that are usually used in such electromagnetic actuators. By increasing the number of windings, the generated field strength, and consequently flux and force, can be maximized while the current is maintained low. Moreover, connection resistances as well as resistances in the used switches of the power electronics can be summed into this series resistance. Thus, its amount cannot be neglected during the analysis of current ripples. On the other hand, the parasitic capacitance that represents capacitance coupling between winding, housing and ground has smaller influence since its amount is relatively small compared to the inductive and resistive behavior, which predominate. Works concede that the influence is significant only at frequencies and switching rates in the MHz-range [85]. Thus, most works neglect the effect of parasitic capacitances [45, 74, 85] in the case of the discussed electromagnetic actuators at low frequencies for sake of model simplicity. Nonetheless, in case strong capacitive behavior is present, its behavior needs to be considered since it introduces oscillations in the current ripples. The interested reader is therefore guided to the work [65], that analyses the influence of the capacitance in case of an underdamped, critically damped and overdamped response of the current ripple.

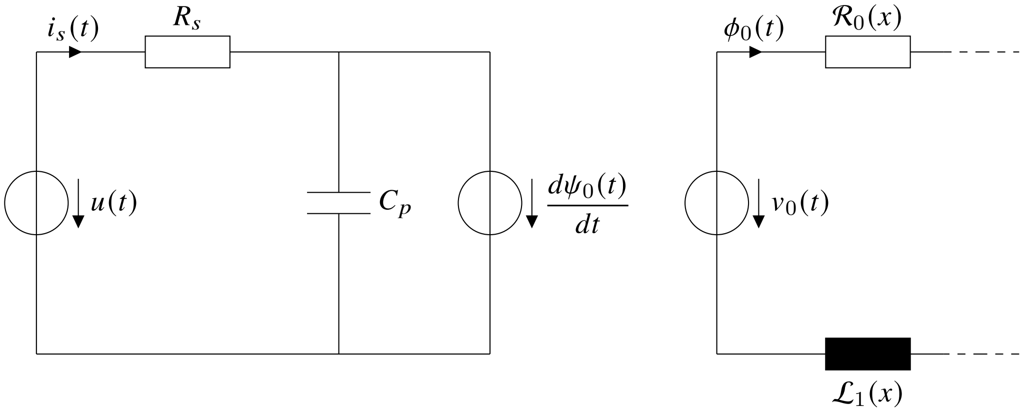

Figure 2.10: Electromagnetic equivalent circuit of a solenoid actuator. The magnetic components connected in series are summarized together.

With the capacitance being neglected ($C_p \rightarrow 0$), the electrical system with an input voltage $u(t)$ can be expressed using the Kirchhoff rules as:

$$u(t) = R_s \cdot i_s(t) + \frac{d\Psi_0(t)}{dt}, \tag{2.51}$$

and can be transformed into the Laplace domain under the negligence of the initial condition as follows:

$$U(s) = R_s I_s(s) + s\Psi_0(s) = R_s I_s(s) + s\frac{\Gamma(s)}{\Upsilon(s)} I_s(s), \tag{2.52}$$

thus yielding the electrical transfer function:

$$\frac{I_s(s)}{U(s)} = \frac{\Upsilon(s)}{R_s\Upsilon(s) + s\Gamma(s)} = \frac{\Xi(s)}{\Lambda(s)}, \tag{2.53}$$

with generic polynomials in s denoted by $\Xi(s)$ for the nominator and $\Lambda(s)$ for the denominator. By using Equation 2.47, the flux distribution inside a solenoid actuator can be calculated considering a certain complexity n_c of the model representing the amount and nature of iron losses inside the actuator. In case solid ferromagnetic materials with high electrical conductivity are used, the more the skin effect needs to be considered, the higher n_c must be chosen for modeling the behavior with high accuracy. From the equation it can be observed that the calculation of the flux inside a particular branch requires the knowledge of the flux inside the other branches. According to Equation 2.47, the flux in the i-th branch relies on the sum of all fluxes in the branches before. Thus, per each branch that gets added to the model, a zero is added into the transfer function. By evaluating Equation 2.47 in a recursive manner, the transfer functions per each branch can be formulated. Starting from the initial branch $i = 0$, it can be obtained:

$$\frac{\Psi_0(s)}{V_0(s)} = \frac{1}{\mathcal{R}_0 + s\mathcal{L}_1} - \frac{\mathcal{R}_1}{\mathcal{R}_0 + s\mathcal{L}_1}\frac{\Psi_1(s)}{V_0(s)}, \tag{2.54}$$

and for a generic branch $i\epsilon[1, n_c]$, the calculation yields to:

$$\frac{\Psi_i(s)}{V_{i-1}(s)} = \frac{1}{\mathcal{R}_i} - \frac{s\mathcal{L}_i}{\mathcal{R}_i}\frac{\sum_{j=i}^{n_c}\Psi_j(s)}{V_{i-1}(s)}. \tag{2.55}$$

Consequently for $i = n_c$, it is observed that

$$\frac{\Psi_{n_c}(s)}{V_{n_c-1}(s)} = \frac{1}{\mathcal{R}_{n_c} + s\mathcal{L}_{n_c}}. \tag{2.56}$$

While analytical and numerical evaluation of the obtained model can be cumbersome, it can be used for analyzing the model order based on the chosen model complexity n_c. It can be seen that due to Equation 2.55, a zero gets added to the transfer function per each model complexity n_c starting from 2. Because of the part $\frac{\mathcal{R}_1}{\mathcal{R}_0+s\mathcal{L}_1}\frac{\Psi_1(s)}{V_0(s)}$, a pole is added to the transfer function per each model complexity n_c. An initial pole is inherently available due to the term $\frac{1}{\mathcal{R}_0+s\mathcal{L}_1}$. This leads to the following statement concerning the polynomials when the order n_c is increased:

$$\frac{\Psi_0(s)}{I_s(s)} = \frac{\Gamma(s)}{\Upsilon(s)} \quad \texttt{with} \quad deg(\Gamma(s)) = n_c - 1 \quad \texttt{and} \quad deg(\Upsilon(s)) = n_c, \tag{2.57}$$

resulting into a strictly proper transfer function, where the degree of the nominator is smaller than the denominator. While this statement only concerns the magnetic circuit, the electrical transfer function can be similarly analyzed by merging the transfer functions from Equation 2.55 and Equation 2.53. In this case, the degrees of the nominator and denominator of the the electrical transfer function adjust as follows:

$$\frac{I_s(s)}{U(s)} = \frac{\Xi(s)}{\Lambda(s)} = \frac{\Upsilon(s)}{R_s(s)\Upsilon(s) + s\Gamma(s)} \quad \texttt{with} \quad deg(\Xi(s)) = n_c \quad \texttt{and} \quad deg(\Lambda(s)) = n_c. \tag{2.58}$$

Therefore, transferring the magnetic transfer function into the electrical domain results into the addition of one further zero, making the electrical transfer function proper, since nominator and denominator equal in their degrees. This behavior of an additional zero inherently leads to a conclusion on the dynamic behavior of the electromagnetic system: from the eddy current model presented in Figure 2.6, it can be seen that a cascade of magnetic RL-circuits models the skin effects that leads to a delayed flux rise in case the magnetic field strength is changed. In this case, the RL-circuits serve as low-pass filters for the magnetic flux. When transformed to the electrical domain by using Equation 2.58, those magnetic low-pass elements are transformed into electrical high-pass filters. This can be also verified by the physical nature of the eddy currents: since they delay the rise of the magnetic flux in response to an instant rise of the exciting magnetic field, they also delay the rise of the inductance that is apparent in the electrical circuit. Thus, the electrical currents rises faster in the circuit due to the absence of an high inductance value. When the eddy currents fade out, the flux is able to rise to its static value, thus increasing the inductance and limiting the current rise in the electrical circuit. The effect is shown for a simulation case by Figure 2.11. In the simulation, a voltage step of 24V is applied to a coil with series resistance of 100 Ω and the following parameters: $\mathcal{R}_0 = 50H^{-1}, \mathcal{R}_1 = 1H^{-1}, \mathcal{R}_2 = 10H^{-1}, \mathcal{L}_1 = 0.001\Omega^{-1}$ and $\mathcal{L}_2 = 0.01\Omega^{-1}$. Similar phenomena were reported in [86].

As mentioned before, the analytical and numerical evaluation of this equation can be cumbersome and expensive in terms of calculation effort when the model complexity n_c is increased dramatically. While this can still be feasible for simulation of the flux

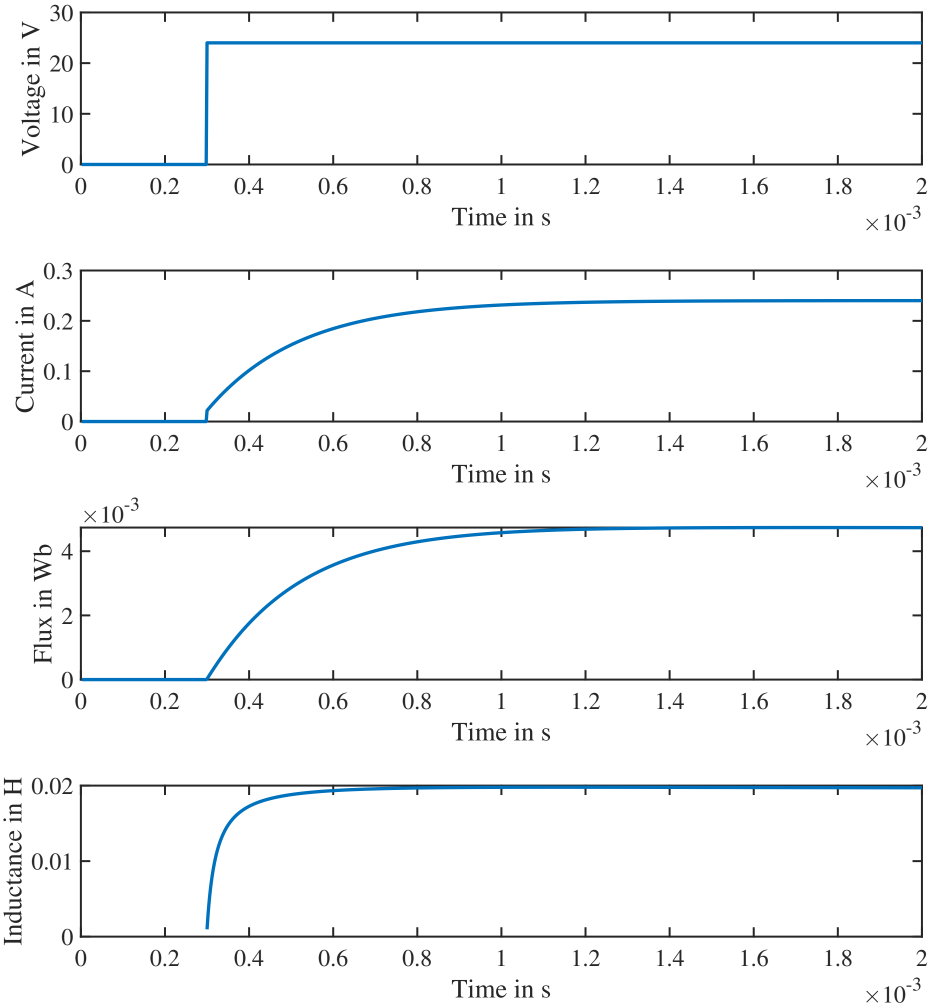

Figure 2.11: Effect of the eddy currents on the current and magnetic flux when a voltage step is applied. Simulation shown for a model order of $n_c = 2$. Last plot shows the static inductance that is apparent on the electrical circuit.

distribution as well as simulation of the obtained current ripple, an online evaluation becomes impractical. Since the obtained model should also be the basis for the real-time self-sensing strategies that are presented in Section 3, a computationally lightweight implementation of the model on computational units with limited power is desired. Thus, it is highly preferred to approximate the model by decreasing n_c. In the following, the model is evaluated for the cases of $n_c = 0...2$, along with the physical meaning behind this simplifications and comparison of accuracy.

Model order of 0 In case the model order accounts to zero, all magnetic inductances disappear. In such a case, no iron losses like eddy currents and hysteretic losses are considered. Setting n_c to zero, therefore, yields to the direct relationship between current and flux linkage:

$$V_0(s) = \mathcal{R}_0 \Phi_0(s), \tag{2.59}$$

being inserted into the electrical transfer function:

$$\frac{I_s(s)}{U(s)} = \frac{N^2}{R_s + s\mathcal{R}_0}, \tag{2.60}$$

a classical first-order low-pass behavior is obtained. It resembles a series connection of the resistance R_s and the incremental inductance $L_\Delta = \frac{N^2}{\mathcal{R}_0}$.

Model order of 1 In the case of a model order equal to one ($n_c = 1$), the magnetic transfer function can be formulated as:

$$V(s) = \mathcal{R}_0 \Phi_0(s) + \mathcal{R}_1 \Phi_0(s) + s\mathcal{L}_1 \Phi_0(s). \tag{2.61}$$

In such a model, the iron losses involving eddy currents and hysteretic losses are modeled, but not to such an extent that the skin effect is considered. This model order can be sufficient e.g. when laminated stator and plunger parts are used and the electrical conductivity of the used materials is small. By considering the number of windings N, the transfer function in the magnetic domain can be achieved:

$$\frac{\Psi_0(s)}{I_s(s)} = \frac{N^2}{\mathcal{R}_0 + \mathcal{R}_1 + s\mathcal{L}_1} = \frac{\Gamma(s)}{\Upsilon(s)}, \tag{2.62}$$

with $\deg(\Gamma(s)) = 0$ and $\deg(\Upsilon(s)) = 1$. The resulting transfer function contains one pole and no zeros. Consequently, the model contains one pole and one zero when transferred to the electrical domain.

Model order of 2 When considering a model order of $n_c = 2$, also a skin effect with 2 layers is taken into consideration. Again, Equation 2.47 can be evaluated and algebraically manipulated to the transfer function:

$$\frac{\Psi_0(s)}{I_s(s)} = \frac{N^2(\mathcal{R}_1 + \mathcal{R}_2 + s\mathcal{L}_2)}{\mathcal{R}_1\mathcal{R}_2 + s\mathcal{R}_1\mathcal{L}_2 + (\mathcal{R}_0 + s\mathcal{L}_1)(\mathcal{R}_1 + \mathcal{R}_2 + s\mathcal{L}_2)} = \frac{\Gamma(s)}{\Upsilon(s)}, \tag{2.63}$$

with $\deg(\Gamma(s)) = 1$ and $\deg(\Upsilon(s)) = 2$. By inserting this magnetic transfer function with Equation 2.53 in the electrical system, again a zero is added to the transfer function.

Choice of an appropriate model order Based on the previous paragraphs, it can be seen that the model order strictly defines to which amount iron losses are considered. From the state-of-the-art it is well-known that iron losses, in particular eddy currents, have a significant impact on self-sensing through back-EMF and inductance. Furthermore, they can even be exploited for self-sensing in case the other quantities do not allow unique estimation results. Thus, in favor of the approaches mentioned in Chapter 3, the model order 0 will be avoided due its negligence of the loss effects. Higher model orders starting from 3, do not seem adequate in terms of computational effort and ease of implementation. Finally, the model orders 1 and 2 seem preferable for the purpose of real-time estimation, depending on whether the skin effect can be considered or neglected.

Figure 2.12 shows the measurement of the current ripple in an electromagnetic actuator with significant eddy current behavior. The plunger is made of solid steel and is especially designed for high eddy currents in order to dampen the field generation and consequently the force generation when a voltage is applied. This allows softer starting and softer landing of the plunger. The actuator as well as the measurement set-up will be described thoroughly in Section 4.3, while only the results are shown here. Models of the order 0, 1 and 2 are fitted on the measured current ripple. It can be seen that the model of order 0 achieves the worst performance with 83 % of fit performance. Moreover, this model is not able to follow the immediate cusps at the switching instants due to the lack of a zero. The models with higher orders archive with 87 % and 90% better fit performances and are able to model the cusp of the current. Nevertheless, the model of the second order shows undesirable overshoots. Because of its acceptable accuracy, reduced computation effort and modeling of the cusps, the model with order one will be used in the following. In fact, the work [63] uses a reduced eddy current model without skin effect and achieved similar estimation of the cusps at the switching instants. It has to be denoted that the model with an order of one achieves good approximation of the cusps due to the presence of a zero, but it is a strong simplification compared to its physical nature. In this model, the cusp is modeled as an immediate jump in the current. This is physically not feasible, since the current can only rise with a finite slope. In practice, there still exists a slight skin effect, that adds delay to the flux and current rise, smoothing the jump. Thus, increasing the number of n_c will adopt the model to its physical background. For the purpose of identifying the eddy current losses, that can be exploited for self-sensing, the model is sufficient.

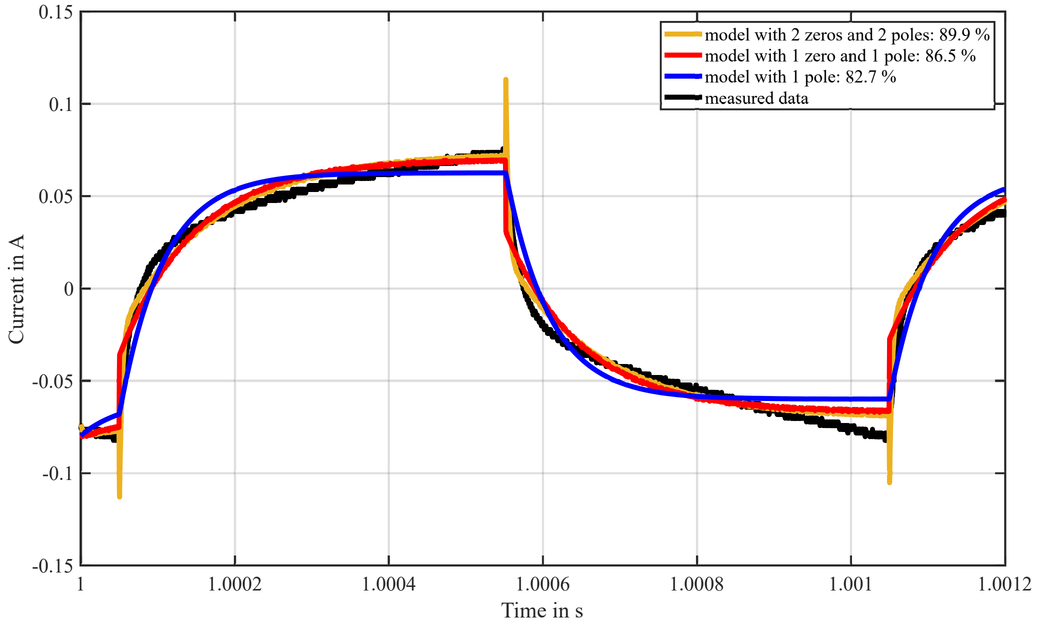

Figure 2.12: Current ripple inside an electromagnetic actuator and model of the current ripple when different model orders are applied, adopted from [66].

With a model order of 1, it is possible to continue with the modeling of the electrical equivalent circuit of the actuator. In particular, all reluctances in the model can be summarized into one reluctance denoted as $\mathcal{R}_\Sigma$:

$$\mathcal{R}_\Sigma = \mathcal{R}_0 + \mathcal{R}_1. \tag{2.64}$$

The corresponding simplified electromagnetic circuit is shown in Figure 2.13.

Considering the assumptions made, the electrical transfer function can be simplified to

$$\frac{I_s(s)}{U(s)} = \frac{\mathcal{R}_\Sigma + s\mathcal{L}_1}{R_s(\mathcal{R}_\Sigma + s\mathcal{L}_1) + sN^2}. \tag{2.65}$$

The calculations conducted above were made in the Laplace domain in order to apply classical circuit theory. Nonetheless, the parameters of the magnetic reluctance $\mathcal{R}_\Sigma$ and the magnetic inductance $\mathcal{L}_1$ are position dependent and change over time in the application. Thus, the partial derivatives of these quantities need to be considered

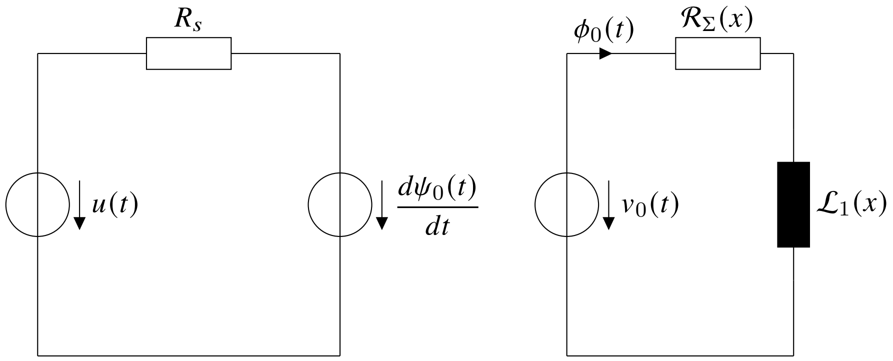

Figure 2.13: Simplified electromagnetic equivalent circuit of a solenoid actuator.

since they induce voltages inside the actuator during movement. Thus, the following calculations will take place in the time domain. The electromagnetic circuit can be described as follows in the time domain:

$$u(t) = R_s i_s(t) + \frac{\partial \psi_0(t)}{\partial t}, \tag{2.66}$$

$$i_s(t) = \frac{1}{N^2}\left(\mathcal{R}_\Sigma(x)\psi_0(t) + \mathcal{L}_1(x)\frac{\partial \psi_0(t)}{\partial t}\right). \tag{2.67}$$

In particular, Equation 2.66 can be rearranged to:

$$\psi_0(t) = \int \left(u(t) - R_s i_s(t)\right) dt. \tag{2.68}$$

By algebraic manipulation of Equations 2.67 and 2.68, the following equation can be achieved:

$$i_s(t) = \frac{\mathcal{R}_\Sigma(x)}{N^2}\left(\int \left(u(t) - R_s i_s(t)\right) dt\right) + \frac{\mathcal{L}_1(x)}{N^2}\left(u(t) - R_s i_s(t)\right). \tag{2.69}$$

In particular, it can be seen that the term $\frac{N^2}{\mathcal{R}_\Sigma(x)}$ resembles the definition of the incremental inductance $L_\Delta(x)$ made in Equation 2.17. Similarly, the term $\frac{N^2}{\mathcal{L}_1(x)}$ has the unit Ω and therefore represents an electrical resistance, which from now on will be called parallel resistance $R_p(x)$. This resistor represents the sum of the losses of eddy currents and hysteretic losses. Hence, modeling losses by means of parallel resistors is a well-known approach in actuator modeling [45, 57, 72], in which the resistor is mostly identified empirically. With the model provided in Sections 2.3 and 2.4 it is possible to derive the resistance based on its physical effects and geometry, and adapt it accordingly to the used loss effects.

Thus, the terms of L_Δ and R_p can be inserted and the equation can be rearranged to:

$$L_\Delta(x) i_s(t) = \int (u(t) - R_s i_s(t))\, dt + \frac{L_\Delta(x)}{R_p(x)} (u(t) - R_s i_s(t)) . \tag{2.70}$$

Performing a differentiation on both sides under the consideration of the time-dependency of the parameters yields to:

$$\begin{aligned} \frac{\partial L_\Delta(x)}{\partial x}\frac{\partial x}{\partial t} i_s(t) + L_\Delta(x)\frac{\partial i_s(t)}{\partial t} &= u(t) - R_s i_s(t) + \frac{\partial}{\partial x}\left(\frac{L_\Delta(x)}{R_p(x)}\right)\frac{\partial x}{\partial t}(u(t) - R_s i_s(t)) \\ &+ \frac{L_\Delta(x)}{R_p(x)}\left(\frac{\partial u(t)}{\partial t} - R_s\frac{\partial i_s(t)}{\partial t}\right) . \end{aligned} \tag{2.71}$$

Rearranging this equation into the form of a differential equation with input $u(t)$ and output $i_s(t)$ leads to:

$$\begin{aligned} \left(1 + \frac{\partial}{\partial x}\left(\frac{L_\Delta(x)}{R_p(x)}\right)\frac{\partial x}{\partial t}\right) u(t) + \frac{L_\Delta(x)}{R_p(x)}\frac{\partial u(t)}{\partial t} &= \left(R_s + \frac{\partial L_\Delta(x)}{\partial x}\frac{\partial x}{\partial t} + R_s\frac{\partial}{\partial x}\left(\frac{L_\Delta(x)}{R_p(x)}\right)\frac{\partial x}{\partial t}\right) i_s(t) \\ &+ L_\Delta(x)\left(1 + \frac{R_s}{R_p(x)}\right)\frac{\partial i_s(t)}{\partial t} , \end{aligned} \tag{2.72}$$

that is an inhomogeneous differential equation of the first order. Furthermore, a direct feed-through of the first derivative of the input is present. In order to simplify mathematical treatment, the following assumption is made:

$$1 >> \frac{\partial}{\partial x}\left(\frac{L_\Delta(x)}{R_p(x)}\right)\frac{\partial x}{\partial t} , \tag{2.73}$$

which allows to set the leading coefficient on the input to one. The assumption usually holds due to the fact that in the discussed electromagnetic actuators L_Δ is usually in the range of $1e^{-3}H$ to $1H$ while R_p is characterized by values higher than 100 Ω. Even in the case of fast switching actuators where $\frac{\partial x}{\partial t}$ is high, the incremental inductance L_Δ is usually designed small for a fast current dynamic. Nevertheless, in case of actuators with high inductance and low parallel resistance (equals high iron losses) are used, it has to be verified individually if this assumption still holds. This can be verified by applying the self-sensing technique that later are being discussed in Chapter 3, under quasi-static conditions, where $\frac{\partial x}{\partial t}$ is null.

Applying the discussed simplification yields:

$$u(t) + \frac{L_\Delta(x)}{R_p(x)}\frac{\partial u(t)}{\partial t} = R_\Sigma i_s(t) + L_\Delta(x)\left(1 + \frac{R_s}{R_p(x)}\right)\frac{\partial i_s(t)}{\partial t} , \tag{2.74}$$

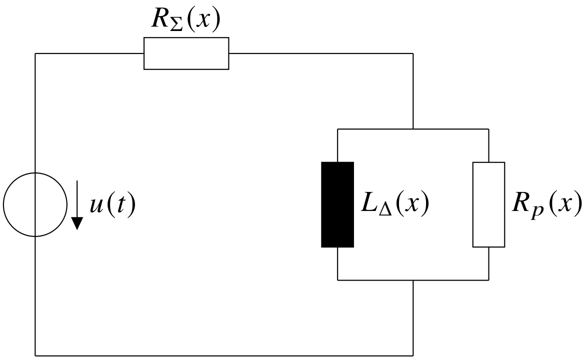

Figure 2.14: Electrical equivalent circuit of a solenoid actuator considering iron losses.

with the total resistance denoted as R_Σ being:

$$R_\Sigma(x) = R_s + \frac{\partial L_\Delta(x)}{\partial x}\frac{\partial x}{\partial t} + R_s \frac{\partial}{\partial x}\left(\frac{L_\Delta(x)}{R_p(x)}\right)\frac{\partial x}{\partial t}. \tag{2.75}$$

This resistor involves not only the copper resistance but also the back-induced voltage due to geometry change by a moving plunger and the back-induced voltage caused by the change of the flux that is generated by the eddy current during movement of the plunger. Since all induced voltages depend on the actual current $i_s(t)$ in the coil, as it is the case for all reluctance-based electromagnetic actuators, a representation as resistive component is possible. The obtained differential Equation 2.74 resembles the model of the electrical equivalent circuit depicted in 2.14 involving a series connection of the resistor R_Σ with the parallel connection of the inductance L_Δ and the parallel resistor R_p. The shown circuit resembles the differential equation for the case $R_\Sigma = R_s$.

2.6 Model of PWM-induced current ripples

Finally, the current ripple inside electromagnetic actuators under PWM voltage operation can be analyzed using the electromagnetic model obtained in the previous section. Before solving the differential Equation 2.74, the switching electronics used for PWM operation as well as the PWM voltage needs to be specified. This work focuses on the driving of an actuator with the so-called bipolar PWM, where positive as well as negative voltages can be applied to the phase terminals. Compared to other approaches, such as the unipolar driving with half-bridge or with a low-side-switch with freewheeling diode, the bipolar approach allows the inversion of the applied voltage and, thus, higher current dynamics during control scenarios. The following derivation will only focus on the bipolar approach due to its universality. Nonetheless, equations for other driving strategies can be easily obtained in a similar manner.

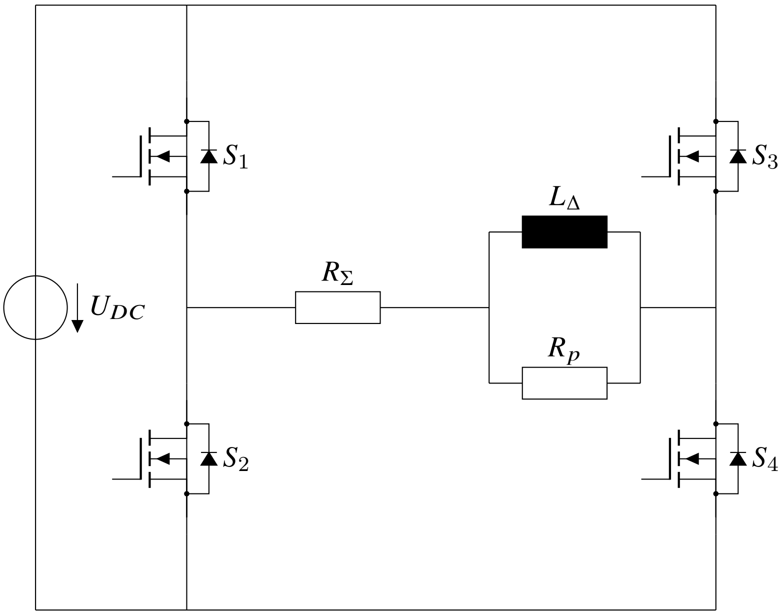

Figure 2.15: Schematic of a H-Bridge driving an electromagnetic actuator.

A common power stage that is able to operate electromagnetic actuators in a bipolar manner is the H-bridge shown in Figure 2.15. It consists of four switches that are connected to the load, in this case the derived electrical equivalent circuit depicted in Figure 2.14. The switches S1 and S4 as well as the switches S2 and S3 operate in a complementary manner in order to avoid a short circuit between the bus voltage U_{DC} and ground. Those switches can be realized as Bipolar Junction Transistors, Insulated Gate Bipolar Transistors or, as usually preferred in applications with high switching frequencies and low power, as Metaloxide Semiconductor Field Effect Transistors (MOSFET) [87].

By operating the H-bridge with a PWM input, the voltage at the phase terminals can be defined as:

$$u_{pwm}(t) = \begin{cases} U_{DC} & \text{for} \quad 0 \leq t \leq \alpha \cdot t_{pwm} \\ -U_{DC} & \text{for} \quad \alpha \cdot t_{pwm} \leq t \leq t_{pwm} \end{cases} , \tag{2.76}$$

with U_{DC} being the bus voltage of the H-bridge, α being the duty cycle in the interval $[0, 1]$ of the PWM and t_{pwm} being the chosen PWM period, as depicted in Figure 2.16. The driving of an inductive load directly leads to the presence of a current ripple. Usually it is desired to reduce the ripple in order to reduce the force ripple generated in the actuator, the acoustic noise as well as the power losses. A common approach is to dimension the PWM frequency significantly higher then the mechanical time constant in order to reduce force ripple and vibrations and higher than 20 kHz in order to shift the generated acoustic noise outside the audible spectrum. Nevertheless, increasing the switching frequency also increases the switching losses in the transistors.

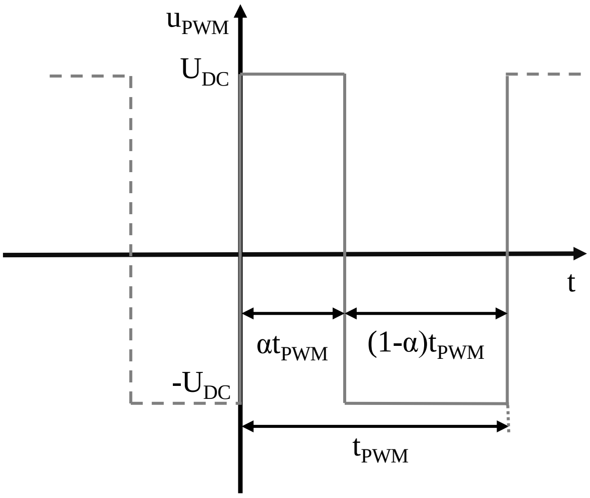

Figure 2.16: Exemplary PWM voltage showing the PWM period and the duty cycle, adopted from [68].

For a successful implementation of the self-sensing strategies in Chapter 3, an accurate analytical solution of the differential Equation 2.74 with respect to the PWM input voltage given in Equation 2.76 needs to be calculated. First, the homogeneous solution of the differential equation is calculated, leading to

$$i_s(t) = i_0 \cdot e^{-\frac{t}{\tau_{el}}}, \tag{2.77}$$

with τ_{el} being the time constant of the electrical system and i_0 being the initial current in the coil. For sake of simplicity, the inhomogeneous solution is calculated first for a simple model that does not involve iron losses. This is achieved by putting $R_p \to \infty$. Afterwards, the inhomogeneous solution for the case with iron losses is discussed with particular focus on the cusps that occur during the switching instants of the voltage.

Solution with iron losses neglected ($R_p \to \infty$) When the iron losses are neglected, a simple RL circuit is obtained that exhibits a low-pass behavior for the current. In this case, the electrical time constant τ_{el} yields to:

$$\tau_{el} = \frac{L_\Delta}{R_\Sigma}, \tag{2.78}$$

and the inhomogeneous solution can be calculated by using the concept of variation of constants. For sake of simplicity, only the solution is provided as:

$$i_s(t) = \begin{cases} \frac{1}{R_\Sigma}\left(U_{DC} + (R_\Sigma \cdot i_0 - U_{DC}) \cdot e^{-\frac{R_\Sigma}{L_\Delta}t}\right) & \text{for} \quad 0 \leq t \leq \alpha t_{pwm} \\ \frac{1}{R_\Sigma}\left(-U_{DC} + \left(R_\Sigma \cdot i_s(\alpha t_{pwm}) + U_{DC}\right) \cdot e^{-\frac{R_\Sigma}{L_\Delta}(t-\alpha t_{pwm})}\right) & \text{for} \quad \alpha t_{pwm} \leq t \leq t_{pwm} \end{cases}, \tag{2.79}$$

with

$$i_s(\alpha t_{pwm}) = \frac{1}{R_\Sigma}\left(U_{DC} + (R_\Sigma \cdot i_0 - U_{DC}) \cdot e^{-\frac{R_\Sigma}{L_\Delta}\alpha t_{pwm}}\right). \tag{2.80}$$

It is visible that the equation has different cases depending on whether the positive or negative voltage is applied. In case of the positive part ($0 \leq t \leq \alpha t_{pwm}$), the current rises until its saturation limit or until the end of the duty cycle when the negative voltage pulse is applied ($\alpha t_{pwm} \leq t \leq t_{pwm}$). Under its excitation, the current decreases until its saturation limit or until the next PWM period begins. For better distinction between the fundamental current i_0 and the components of the current ripple, it can be algebraically manipulated to:

$$i_s(t) = \begin{cases} i_0 + \left(\frac{U_{DC}}{R_\Sigma} - i_0\right)\left(1 - e^{-\frac{R_\Sigma \cdot t}{L_\Delta}}\right) & \text{for} \quad 0 \leq t \leq \alpha t_{pwm} \\ i_s\left(\alpha t_{pwm}\right) + \left(\frac{-U_{DC}}{R_\Sigma} - i_s(\alpha \cdot t_{pwm})\right)\left(1 - e^{-\frac{R_\Sigma(t-\alpha t_{pwm})}{L_\Delta}}\right) & \text{for} \quad \alpha t_{pwm} \leq t \leq t_{pwm} \end{cases}. \tag{2.81}$$

In particular, the maximum amplitude of the ripple and its shape can be analyzed:

$$i_s(t) = \underbrace{i_0}_{\text{fundamental}} + \underbrace{\underbrace{\left(\frac{U_{DC}}{R_\Sigma} - i_0\right)}_{\text{amplitude}}\underbrace{\left(1 - e^{-\frac{R_\Sigma \cdot t}{L_\Delta}}\right)}_{\text{shape}}}_{\text{ripple}}, \tag{2.82}$$

where the parts are highlighted for the rising part of the current ripple. In the same manner, the parts can be separated for the falling part of the current ripple:

$$i_s(t) = \underbrace{i_s(\alpha t_{pwm})}_{\text{fundamental}} + \underbrace{\underbrace{\left(\frac{-U_{DC}}{R_\Sigma} - i_s(\alpha t_{pwm})\right)}_{\text{amplitude}}\underbrace{\left(1 - e^{-\frac{R_\Sigma \cdot t}{L_\Delta}}\right)}_{\text{shape}}}_{\text{ripple}}. \tag{2.83}$$

The amplitude of the current ripple is limited by its physical saturation limit defined by the maximum applicable voltage that is either U_{DC} or $-U_{DC}$, the total resistance R_Σ and the actual fundamental current. The shape of the current ripple is exponential. In cases where the inductance behavior is more significant than the resistive behavior ($L_\Delta \gg R_\Sigma$), the current ripple can be considered almost linear. Figure 2.17 shows the current ripple in case of a RL load when a PWM voltage is applied.

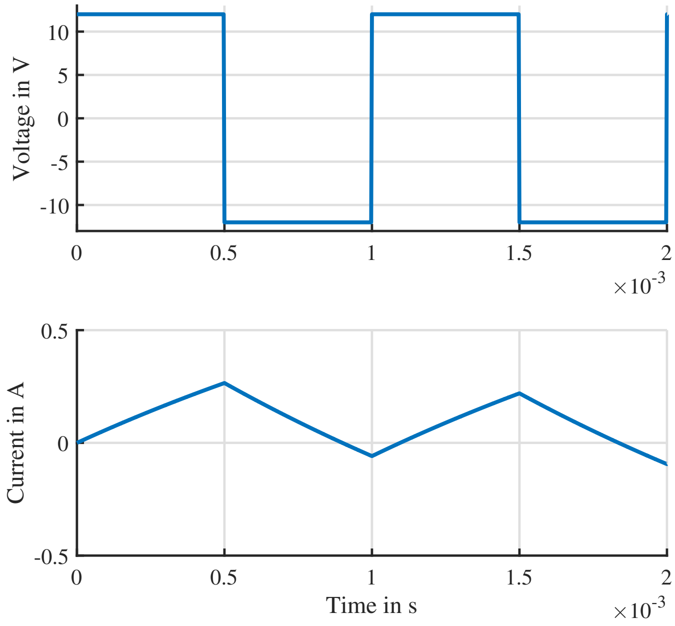

Figure 2.17: Simulated current ripple for an inductive load ($L_\Delta = 20\ mH$) with series resistance ($R_\Sigma = 10\ \Omega$). The applied PWM voltage has an amplitude of $U_{DC} = 12\ V$ and a frequency of $f_{PWM} = 1\ kHz$.

Solution with iron losses considered When iron losses are considered, the parallel resistance exhibits a finite value, therefore the full Equation 2.74 must be considered, along with the derivative of the input voltage. The PWM input given by Equation 2.76 is a non-continuous function, which is indeed not differentiable. Consequently, another representation of the PWM input voltage needs to be considered. While smoothed jumps or ramps with a certain rise time can be easily considered for numerical solution of the differential equation, another approach is required for the analytical solution that is preferred in this work. Thus, the Heaviside step function $\Theta(t)$ is considered [84, p. 175]:

$$\Theta(t) = \begin{cases} 0 & \text{for} \quad t < 0 \\ 1 & \text{for} \quad t \geq 1 \end{cases} . \tag{2.84}$$

Its derivative yields to the Dirac impulse $\delta(t)$:

$$\delta(t) = \frac{d\Theta(t)}{dt} = \begin{cases} \infty & \text{for} \quad t = 0 \\ 0 & \text{else} \end{cases}, \tag{2.85}$$

that allows an analytical solution of the differential equation with respects to its input voltage. Contrary to Equation 2.76, the PWM voltage can now be defined as:

$$u(t) = -U_{DC} + 2U_{DC}\Theta(t), \tag{2.86}$$

for the rising edge and in an analog way to

$$u(t) = U_{DC} - 2U_{DC}\Theta(t - \alpha \cdot t_{pwm}), \tag{2.87}$$

for the falling edge. Finally, the PWM voltage for both positive and negative voltage pulses can be obtained as

$$u_{pwm}(t) = -U_{DC} + 2U_{DC}\Theta(t) - 2U_{DC}\Theta(t - \alpha \cdot t_{pwm}). \tag{2.88}$$

Finally, the homogeneous solution of Equation 2.74 with respect to the input voltage Equation 2.88 can be calculated to:

$$i_s(t) = \begin{cases} e^{-\frac{t}{\tau_{el}}} \left(i_0 + \frac{U_{DC}}{R_\Sigma} - h_i\right) - \frac{U_{DC}}{R_\Sigma} & \text{for } t \rightarrow 0^- \\ e^{-\frac{t}{\tau_{el}}} \left(i_0 + \frac{U_{DC}}{R_\Sigma} - h_i\right) - \frac{U_{DC}}{R_\Sigma} + \frac{2U_{DC}}{R_\Sigma}\left(1 - e^{-\frac{t}{\tau_{el}}}\right) + h_i e^{-\frac{t}{\tau_{el}}} & \text{for } 0^+ \leq t \leq t_*^- \\ e^{-\frac{t-t_*}{\tau_{el}}} \left(i_s(t_*^-) - \frac{U_{DC}}{R_\Sigma}\right) + \frac{U_{DC}}{R_\Sigma} - \frac{2U_{DC}}{R_\Sigma}\left(1 - e^{-\frac{t-t_*}{\tau_{el}}}\right) - h_i e^{-\frac{t-t_*}{\tau_{el}}} & \text{for } t_*^+ \leq t \leq t_{pwm}^- \end{cases}, \tag{2.89}$$

with t_* and h_i being

$$t_* = \alpha \cdot t_{pwm}, \tag{2.90}$$

$$h_i = \frac{2U_{DC}}{R_\Sigma + R_p}. \tag{2.91}$$

In the considered case, the electrical time constant changed to

$$\tau_{el} = \frac{L_\Delta \left(R_p + R_\Sigma\right)}{R_p R_\Sigma}, \tag{2.92}$$

where also the iron losses are taken into account. Due to the term $\frac{\partial u(t)}{\partial t}$, instantaneous cusps occur at the voltage switching instants. Because of this, the solution now considers three cases: the time before the first switching instant ($t < 0^-$), the time between positive and negative switching instants ($0^+ \leq t \leq t_*^-$) and the time between the negative switching instant and the switching instant of the following PWM period ($t_*^+ \leq t \leq t_{pwm}^-$). The indices + and − indicate if the particular switching instant is approached from the left (−) or the right side (+). It has to be denoted that the first case is only a theoretical case since it resembles zero from the left but not before. Similarly to the case without iron losses, the equation can be rearranged for better comprehension:

$$i_s(t) = \begin{cases} i_0 + \left(\frac{-U_{DC}}{R_\Sigma} - i_0\right)\left(1 - e^{-\frac{t}{\tau_{el}}}\right) - h_i e^{-\frac{t}{\tau_{el}}} & \text{for } t \longrightarrow 0^- \\ i_0 + \left(\frac{U_{DC}}{R_\Sigma} - i_0\right)\left(1 - e^{-\frac{t}{\tau_{el}}}\right) & \text{for } 0^+ \leq t \leq t_*^- \\ i_s(t_*^-) + \left(\frac{-U_{DC}}{R_\Sigma} - i_s(t_*^-)\right)\left(1 - e^{-\frac{t-t_*}{\tau_{el}}}\right) - h_i e^{-\frac{t-t_*}{\tau_{el}}} & \text{for } t_*^+ \leq t \leq t_{pwm}^- \end{cases} . \tag{2.93}$$

In this case, the current ripple is splitted into three parts:

$$i_s(t) = \underbrace{i_s(t_*^-)}_{\text{fundamental}} + \underbrace{\underbrace{\left(\frac{-U_{DC}}{R_\Sigma} - i_s(t_*)\right)}_{\text{amplitude}} \underbrace{\left(1 - e^{-\frac{t}{\tau_{el}}}\right)}_{\text{shape}}}_{\text{ripple}} - \underbrace{\underbrace{\frac{2U_{DC}}{R_\Sigma + R_p}}_{\text{height}} \underbrace{e^{-\frac{t}{\tau_{el}}}}_{\text{decay}}}_{\text{cusp}}, \tag{2.94}$$

shown for the time instant $t_*^+ \leq t \leq t_{pwm}^-$. For sake of brevity, the separated terms for the other cases are not shown here. Generally, it can be seen that the current ripple resembles the current ripple without iron losses. The fundamental part stays the same since it is related to the static current that is not affected by dynamic iron losses. The ripple itself exhibits the same amplitude with and without iron losses, but a different electrical time constant that is now smaller than the one without iron losses. In particular, for very small iron losses, which results into a high parallel resistance, the same time constant is achieved as in the case without iron losses. Finally, a third term is added to the current ripple expressions. In particular, the term reflects the cusps that occur during the switching instants. The cusps exhibit a height that is dependent on the parallel resistance R_p and the maximum applicable voltage. There is still an exponential term that models the decay of the cusps over time. With this term, the decay of iron losses is considered when the transients ran out. It has to be highlighted that this model applies simplifications for the analytical solution and for reduced calculation effort. In reality, the current cannot rise with an infinite rise time. The skin effect as well as the parasitic inductances prevent this, as it was presented in Chapter 2.5 for higher model complexities n_c. Nevertheless, as it can be seen during the experimental results, that current ripples on physical electromagnetic actuators can be successfully approximated by this model, since their cusps rise with a finite, but significantly large, slew rate. Figure 2.18 shows simulation results of the current ripple for an inductor in several configurations. The behavior is exponentially-shaped and resembles a charging and discharging behavior. With iron losses, remarkable cusps occur and the electrical time constant changes.

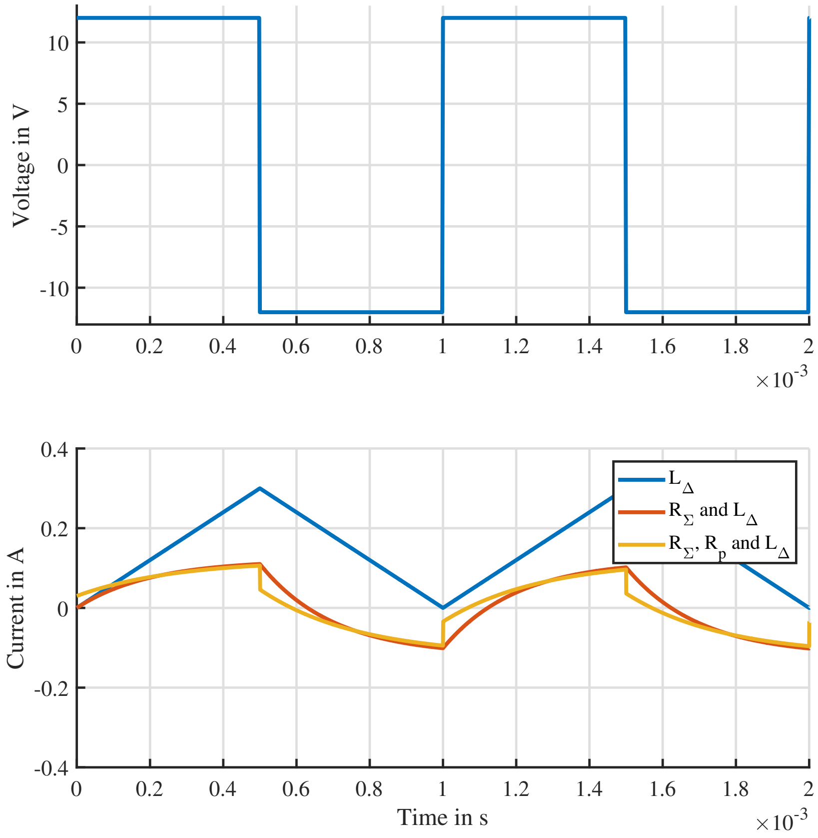

Figure 2.18: Simulated current ripple for an inductive load ($L_\Delta = 10$ mH) with and without series resistance ($R_\Sigma = 100\ \Omega$) and parallel resistance ($R_p = 300\ \Omega$). The applied PWM voltage has an amplitude of $U_{DC} = 12$ V and a frequency of $f_{PWM} = 1\ kHz$.

The height of the current ripple cusp can be calculated for the switch from negative to positive voltage ($t = 0$):

$$h_i^+ = i_s(0^+) - i_s(0^-) = \frac{2U_{DC}}{R_\Sigma + R_p}, \tag{2.95}$$

and for the switch from positive to negative voltage ($t = t_*$):

$$h_i^- = i_s(t_*^+) - i_s(t_*^-) = -\frac{2U_{DC}}{R_\Sigma + R_p}. \tag{2.96}$$

3 Position self-sensing techniques based on PWM-induced current ripples

A general model of current ripples inside electromagnetic actuators involving iron losses has been derived and analyzed in the previous chapter. As seen, the parameters of the incremental inductance L_Δ and the iron loss resistor R_p show a dependency on the actuator position x, which can be exploited for position self-sensing. From the analysis of the state-of-the-art, it is visible that different approaches for the identification of those parameters can be applied. In this thesis, the approach of analog preprocessing is followed that aims for high SNR while maintaining the computational effort on the microprocessor low.

The overall actuation system consists of the electromagnetic actuator (EMA), that is depicted in Figure 3.1, which is under operation and needs to be monitored or controlled. This actuator is driven by a power amplifier, which is a MOSFET-based H-bridge configuration as shown in Chapter 2.5. The electrical quantities are being sensed and brought to the analog preprocessing stage (denoted as IDIM circuit), which is going to be described later in this chapter, and an analog-digital converter (ADC). The quantized and discretized values of the ADC are sent to the microcontroller unit, that performs the identification of the physical parameters that are necessary for self-sensing. The position estimation is obtained by a mathematical model with additional hysteresis compensation and can be used for monitoring, control or functional safety purposes. The microcontroller itself also generates the PWM signal for the power amplifier. In applications with increased need for redundancy, also a position sensor can be present. The different domains of the electrical signals, namely the digital domain (yellow), the analog domain (green) and the power domain (red) are highlighted in the figure to stress the fact that an analog circuitry can perform some signal processing steps that can unload the ADC and the microprocessor unit.

In the following subchapters, different self-sensing algorithms for different application scenarios are presented, derived and analyzed. First, the focus is laid on the incremental inductance since it promises the best results for position estimation on non-ambiguous actuators. Therefore, the analog circuitry of the IDIM technique is shown and discussed. In particular, Chapter 3.1 shows the general derivation and description of the IDIM

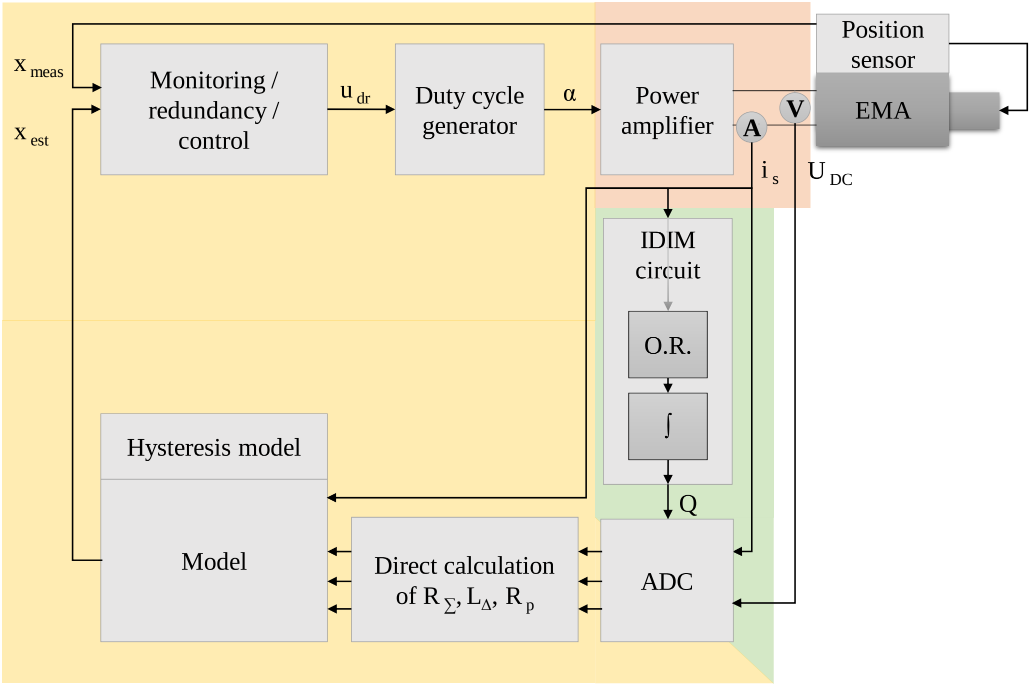

Figure 3.1: Schematic of the overall actuation system, consisting of the EMA, a power amplifier, the self-sensing circuit and a microcontroller unit. The digital domain (yellow) performs only the necessary calculations, while the analog domain (green) carries out most of the signal processing. The power domain is highlighted as red.

technique involving also a discussion of conditions for identifiability and a sensitivity analysis of measurement errors in the sensors and the analog circuity. Furthermore, an identification approach is shown for the series resistance R_Σ that allows compensating of unwanted resistive behaviors and allows identifying the actuator temperature that can compensate for temperature-dependent parameters and temperature drifting. While Chapter 3.1 shows the IDIM technique in its full extent, simplification can be applied for applications involving actuators with reduced dynamics or negligible iron losses. Such simplification accounts for switching actuators in a quasi-static manner, whose end-position needs to be detected. In such cases, the measurement and modeling effort can be significantly reduced compared to the full IDIM formulation. This reduces the costs of the electronics in such application scenarios, which are especially cost-sensitive. Similar to Chapter 3.1, the simplified IDIM technique is shown and derived and a sensitivity analysis concerning measurement errors is conducted. Chapter 3.3 discusses the estimation based on the eddy current through the parallel resistance R_p, which is especially important in applications where the incremental inductance is not monotonous. Then, Chapter 3.4 compares the different self-sensing techniques in terms of the number of necessary measurements, the number of calculations, the simplifications that were made during the derivation, the sensitivity towards errors, the SNR and possible applications scenarios. All shown self-sensing approaches are based on the identification of the incremental inductance L_Δ and the parallel resistor R_p. An appropriate model, either of physical or phenomenological nature, needs to be derived that assumes a position dependency and a current dependency of both parameters due to saturation and hysteretic effects: $L_\Delta = f(i,x)$, $R_p = f(x)$. By inverting the model, the estimated position can be achieved: $x_{est} = f^{-1}(L_\Delta, R_p, i)$. Chapter 3.5 presents such classes of models and selects the ones with the best accuracy and the lowest computational effort. Finally, Chapter 3.6 shows an approach for compensating unwanted hysteretic behavior in the position estimate for further increase of the accuracy.

The basic circuitry for analog prepossessing, which is necessary for the IDIM technology is illustrated in Figure 3.2. It consist of two stages: an offset elimination stage (O.E.), that is necessary for the removal of the fundamental driving current and an analog integrator circuit with external reset that integrates the current ripple within one PWM period. Removing the fundamental driving current is necessary in order to separate the current ripple from the fundamental current, that is usually several orders higher then the current ripple. As visible from Equation 2.93, only the current ripple contains the information that is necessary in the self-sensing algorithms. Removing the offset ensures that only the relevant information is integrated and the integrator does not suffer from drifting. In the following, the offset removed current is referred to as $\bar{i_s}(t)$, the reset signal as $r(t)$ and the integral output as $Q(t)$, since the integral of a current quantity refers physically to a charge. The offset elimination stage as well as the reset signal can change according to the used IDIM technique and are further explained in the subchapters.

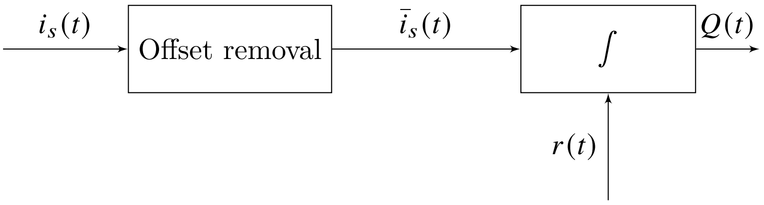

Figure 3.2: General IDIM measurement chain consisting of an offset-removing stage and a resettable integrator.

Before deriving the techniques, basic measurement quantities are defined. In this thesis, only shunt-based current sensors in series with the phase are considered. Results for shunt-based sensors, where the shunt is placed at the low-side FET or the DC link, as well as other sensor principles, such as Hall-based or magnetic resistance-based sensors can be derived similarly from the presented results. Shunt-based sensors provide a voltage that is linearly dependent on the voltage over the shunt resistor:

$$u_{meas} = G \cdot u_{shunt} + u_{off}, \tag{3.1}$$

with u_{off} being an offset voltage that allows for bidirectional sensing and G being the gain. The voltage drop over the shunt resistor is proportional to the current:

$$u_{shunt} = R_{shunt} \cdot i_s, \tag{3.2}$$

where R_{shunt} denotes the shunt resistance. The measured output voltage of the sensor is then the input of the IDIM circuit shown in Figure 3.2. For sake of simplicity and easier mathematical handling, all components of the measurement chain are neglected so that: $G = 1$, $R_{shunt} = 1\ \Omega$, $u_{off} = 0\ V$, which yields to $u_{meas} = i_s$. The DC link voltage U_{DC} is usually measured by means of voltage dividers. For sake of brevity, a divider ratio equal to one is chosen so that the DC link voltage is directly available.

An analog integrator can be configured as indicated in Figure 3.3. By means of the integration resistor R_{int} and the integrator capacitance C_{int}, the input voltage can be amplified. When the noise on the signal is Gaussian white noise with zero mean value, the integrator is able to amplify the signal while rejecting noise. In order to avoid a saturation of the integrator, a reset is necessary to bring the integrator state to zero at defined instants. This can be achieved by using a reset switch. In particular, such a reset switch is able to completely decharge the capacitor when it is closed, thus the integrator value can be reset to zero.

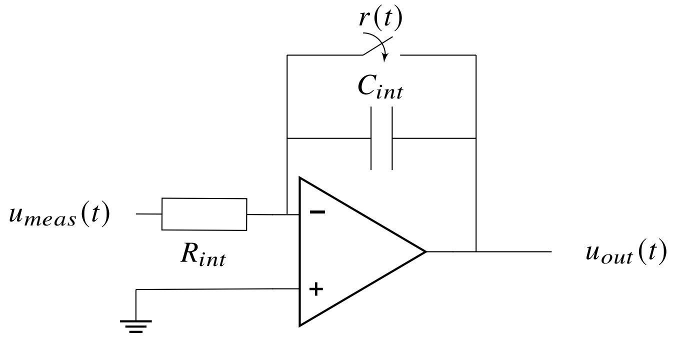

Figure 3.3: Single-ended analog inverting integrator with reset capability, adopted from [88, p. A-31].

The integrator circuit can be mathematically described as:

$$u_{out}(t) = -\frac{1}{R_{int}C_{int}} \int_{r(t)\neq 1} u_{meas}(t)dt - u_C(0). \tag{3.3}$$

In case the reset signal amounts to 1, the integrator is resetted and its current value is forced to zero. In case the reset signal equals zero, the integration starts. By forcing $r(t) = 1$ at the beginning of each integration window, the initial condition on the capacitor voltage u_C is always kept to zero. For sake of brevity and better mathematical handling, also here the gain is set to one by setting $R_{int} = 1\Omega$ and $C_{int} = 1F$ so that the integral can be defined as:

$$Q(t) = \int_{r(t)\neq 1} \bar{i}_s(t)dt. \tag{3.4}$$

3.1 Self-Sensing based on the incremental inductance for dynamic cases

In the previous section, the circuitry for the IDIM technique was briefly presented. In this section, the IDIM technique in its complete formulation is derived and discussed. Such formulation allows applying the technique onto actuators with high current dynamic and iron losses. Moreover, the identification of the series resistance is possible, that can be used for compensation of resistive behavior as well as an estimation of the actuator temperature. In this general formulation of the IDIM technique, the offset-eliminating stage is realized by means of a sample-and-hold (SH) circuitry followed by a subtraction stage, that removes the sampled value from the actual value. By applying such a subtraction, the fundamental current in the measurement is eliminated, thus only the current ripple can be processed. Figure 3.4 shows the schematic of the circuitry. The SH stage is also triggered by the reset signal that is given to the integrator. In this derivation, a perfect SH stage is assumed for better mathematical treatment. Nevertheless, the technical realization of an appropriate SH stage is a challenging task since the droop of the stage due to parasitic conductance must be minimized, especially when large hold times are considered. The technical realization of such a stage is explained briefly in Chapter 4.1.

The reset signal is chosen in such a way that the PWM switching instants are not being integrated:

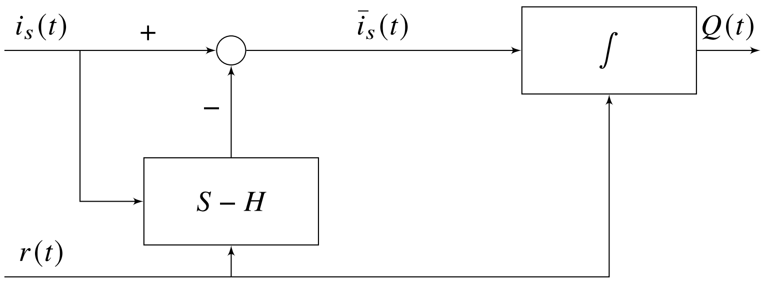

Figure 3.4: IDIM measurement chain with sample-and-hold unit based offset removal, adopted from [71].

$$r(t) = \begin{cases} 0 & \text{for} \quad t_s^+ \le t \le t_e^+ \\ 0 & \text{for} \quad t_s^- \le t \le t_e^- \\ 1 & \text{else} \end{cases}, \tag{3.5}$$

The time instants t_s^+ and t_e^+ refer to the start (s) and end (e) of the integration window when a positive PWM voltage pulse is applied and the time instants t_s^- and t_e^- to the integration window borders when a negative PWM voltage pulse is applied. They can be defined as:

$$t_s^+ = t_r, \tag{3.6}$$

$$t_e^+ = \alpha t_{pwm} - t_r, \tag{3.7}$$

$$t_s^- = \alpha t_{pwm} + t_r, \tag{3.8}$$

$$t_e^- = t_{pwm} - t_r, \tag{3.9}$$

with a suitable waiting time t_r. When $r(t)$ is equal to zero, the SH stage hold its last value and the integration is performed until $r(t)$ equals one. In this time instant, the integrator is reset and the input signal is not considered. Figure 3.5 illustrates the chosen time intervals of the reset signal within one PWM period. In particular, the waiting time t_r is a design choice and must be large enough in order to ensure a proper decharging of the integration capacitance and small enough that a large integration interval is covered. Furthermore, the time t_r should cover possible glitches in the current due to inverter switching effects, e.g. dead-time insertion as well as ringing, and effects of the limited slew rate of current shunt amplifiers in these regions. In addition, the time t_r should cover the current ripple cusps and their exponential decay due to eddy currents. By setting $r(t)$ to 1 in these time instants, the integrator is in reset and the current information, involving the glitches and eddy current effects, are not taken into consideration during evaluation of the integral. Similar avoidance of possible glitches is also conducted in the oversampling approaches [51, 53].

The current differences

$$\Delta i^{+} = i_s(t_e^{+}) - i_s(t_s^{+}), \tag{3.10}$$

$$\Delta i^{-} = i_s(t_e^{-}) - i_s(t_s^{-}), \tag{3.11}$$

and the time differences

$$\Delta t^{+} = t_e^{+} - t_s^{+}, \tag{3.12}$$

$$\Delta t^{-} = t_e^{-} - t_s^{-}, \tag{3.13}$$

are defined.

3.1.1 Derivation of the estimation equations

By applying the reset signal provided by Equation 3.5, the integral equation can be defined as:

$$Q(t) = \int_{r(t)\neq 1} \bar{i}_s(t)dt = \int_{r(t)\neq 1} \left(i_s(t) - i_s(t_x)\right) dt, \tag{3.14}$$

where t_x equals the time when the sampling has happened at the start of the integration window. Thus, t_x equals t_s^{+} in case the equation is evaluated for the positive voltage pulse and t_x equals t_s^{-} in case of the negative voltage pulse. The offset-removed current $\bar{i}_s(t)$ is now replaced by the output of the subtraction stage. Inserting the differential Equation 2.74 of the electrical equivalent circuit into the integral form yields to:

$$Q(t) = \int_{r(t)\neq 1} \frac{1}{R_\Sigma}\left[u(t) + \frac{L_\Delta}{R_p}\frac{\partial u(t)}{\partial t} - L_\Delta\left(1 + \frac{R_\Sigma}{R_p}\right)\frac{\partial i_s(t)}{\partial t}\right] - i_s(t_x)dt. \tag{3.15}$$

It has to be remarked that L_Δ and R_p are parameters that are position-, current- and temperature-dependent. In the following derivation, these parameters are assumed to be constant over one PWM period in order to simplify the mathematical treatment. This assumption holds for high PWM frequencies, where the PWM time period is considerably smaller than the time constant of the mechanical and thermal subsystem: $t_{pwm} \ll \tau_m, \tau_{th}$. Thus, the dependency of the parameters on the position, temperature and current is not shown in the following calculations. Evaluating the integral equation for a positive voltage pulse yields to:

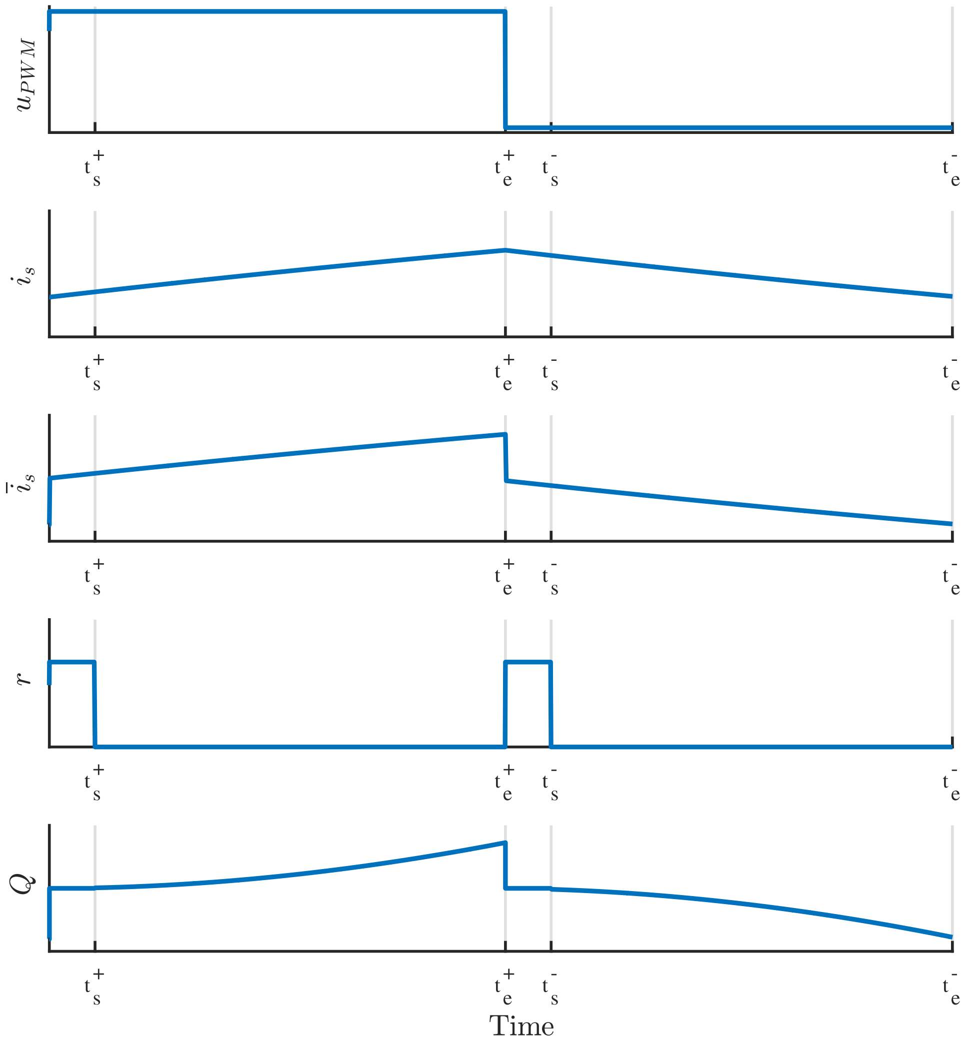

Figure 3.5: Integral signal $Q(t)$ and reset signal $r(t)$ when being applied to an offset-removed current ripple $\bar{i}_s$ of an electromagnetic actuator along with the critical time instants.

$$
\begin{aligned}
Q(t_e^+) - Q(t_s^+) = & \frac{U_{DC}}{R_\Sigma}\left(t_e^+ - t_s^+\right) + \frac{L_\Delta}{R_\Sigma R_p}\left(u(t_e^+) - u(t_s^+)\right) - \frac{L_\Delta}{R_\Sigma}\left(1 + \frac{R_\Sigma}{R_p}\right)\left(\left(i_s(t_e^+) - i_s(t_s^+)\right)\right) \\
& - i_s(t_s^+)\left(t_e^+ - t_s^+\right).
\end{aligned}
\tag{3.16}
$$

The expression from the integral can be simplified by considering that the integrator is reset at the begin of every PWM period: $Q(t_s^+) = 0$ and by using a fixed DC voltage during one pulse $u(t_e^+) = u(t_s^+) = U_{DC}$. Furthermore, the assumption $R_\Sigma \ll R_p$ can be applied since electromagnetic actuators are designed for minimal copper losses, which yields to a small value of R_Σ and small iron losses, which results into a high value of R_p. Considering these assumptions, the integral can be solved:

$$
Q(t_e^+) \approx \frac{U_{DC}}{R_\Sigma}\Delta t^+ - \frac{L_\Delta}{R_\Sigma}\Delta i^+ - i_s(t_s^+)\Delta t^+. \tag{3.17}
$$

Analogously, the integral can be evaluated for the negative voltage pulse:

$$
\begin{aligned}
Q(t_e^-) - Q(t_s^-) = & \frac{-U_{DC}}{R_\Sigma}\left(t_e^- - t_s^-\right) + \frac{L_\Delta}{R_\Sigma R_p}\left(u(t_e^-) - u(t_s^-)\right) - \frac{L_\Delta}{R_\Sigma}\left(1 + \frac{R_\Sigma}{R_p}\right)\left(i_s(t_e^-) - i_s(t_s^-)\right) \\
& - i_s(t_s^-)\left(t_e^- - t_s^-\right),
\end{aligned}
\tag{3.18}
$$

and with the considerations $Q(t_s^-) = 0$ and $u(t_e^-) = u(t_s^-) = -U_{DC}$, it can be solved to:

$$
Q(t_e^-) \approx \frac{-U_{DC}}{R_\Sigma}\Delta t^- - \frac{L_\Delta}{R_\Sigma}\Delta i^- - i_s(t_s^-)\Delta t^-. \tag{3.19}
$$

The equations of the integral for the positive and negative voltage pulses can be brought into a matricial form

$$
\begin{bmatrix} U_{DC}\Delta t^+ \\ -U_{DC}\Delta t^- \end{bmatrix} \approx \underbrace{\begin{bmatrix} Q(t_e^+) + i_s(t_s^+)\Delta t^+ & \Delta i^+ \\ Q(t_e^-) + i_s(t_s^-)\Delta t^- & \Delta i^- \end{bmatrix}}_{\mathbf{A}} \begin{bmatrix} R_\Sigma \\ L_\Delta \end{bmatrix}, \tag{3.20}
$$

where the parameter vector containing R_Σ and L_Δ can be obtained by inverting the matrix A that contains the measurements:

$$
\begin{bmatrix} R_\Sigma \\ L_\Delta \end{bmatrix} \approx \mathbf{A}^{-1} \begin{bmatrix} U_{DC}\Delta t^+ \\ -U_{DC}\Delta t^- \end{bmatrix}. \tag{3.21}
$$

If $\mathbf{A}$ is invertible, then its inverse can be calculated as

$$\mathbf{A}^{-1} = \frac{1}{|\mathbf{A}|} \begin{bmatrix} \Delta i^- & -\Delta i^+ \\ -Q(t_e^-) - i_s(t_s^-)\Delta t^- & Q(t_e^+) + i_s(t_s^+)\Delta t^+ \end{bmatrix}, \tag{3.22}$$

with

$$|\mathbf{A}| = \det(\mathbf{A}) = \left(Q(t_e^+) + i_s(t_s^+)\Delta t^+\right)\Delta i^- - \left(Q(t_e^-) + i_s(t_s^-)\Delta t^-\right)\Delta i^+, \tag{3.23}$$

being its non-zero determinant. Thus, the parameters can be estimated by the estimation equations:

$$R_\Sigma \approx \frac{U_{DC}}{|\mathbf{A}|}\left(\Delta i^- \Delta t^+ + \Delta i^+ \Delta t^-\right), \tag{3.24}$$

and

$$L_\Delta \approx -\frac{U_{DC}}{|\mathbf{A}|}\left(\left(Q(t_e^-) + i_s(t_s^-)\Delta t^-\right)\Delta t^+ + \left(Q(t_e^+) + i_s(t_s^+)\Delta t^+\right)\Delta t^-\right). \tag{3.25}$$

Due to the combined identification, the series resistance can be actively compensated in the estimation of the incremental inductance. This not only compensates for the resistive behavior that results into an exponential-shaped current ripple, but also for back-induced voltages during the movement of the actuator and a possible change of the resistance due to self-heating. From the estimation equations, it can be also seen that the IDIM technique requires in total seven measurements per PWM period: one measurement of the DC link voltage, four measurements of the current at the time instants t_s^+, t_e^+, t_s^- and t_e^- as well as two measurements of the integral at the time instants t_e^+ and t_e^-. The estimation itself can be computed relatively fast, since it is the solution of a 2x2 linear system. Nevertheless, there is still noise present inside the estimate due to the usage of current differences, which resemble current derivatives.

In case the determinant amounts to zero, or only the positive or negative voltage pulse can be evaluated, the incremental inductance can be still estimated under knowledge of the series resistance R_Σ using Equations 3.17 and 3.19 as

$$L_\Delta \approx \frac{U_{DC}\Delta t^+ - R_\Sigma\left(Q(t_e^+) + i_s(t_s^+)\Delta t^+\right)}{\Delta i^+}, \tag{3.26}$$

for the positive voltage pulse and

$$L_\Delta \approx \frac{-U_{DC}\Delta t^- - R_\Sigma\left(Q(t_e^-) + i_s(t_s^-)\Delta t^-\right)}{\Delta i^-}, \tag{3.27}$$

for the negative voltage pulse. More about the conditions for identifiablity and the resulting need for a pre-knowledge of the series resistance R_Σ is given in the following section.

3.1.2 Conditions for the estimation based on the incremental inductance

In the following section, conditions will be derived for the determinant $|A|$, in which an identification of one or both parameters is not possible. Such operating points, in which the conditions are fulfilled, should be avoided, or further knowledge is required for determination in those working points. For sake of brevity, the currents $i_s^+ = i_s(t_s^+)$ and $i_s^- = i_s(t_s^-)$ are defined so that the determinant can be rewritten as

$$|\mathbf{A}| = \left(Q(t_e^+) + i_s^+ \Delta t^+\right) \Delta i^- - \left(Q(t_e^-) + i_s^- \Delta t^-\right) \Delta i^+. \tag{3.28}$$

A condition for invertibility is that the determinant is nonzero so that the matrix has full rank:

$$|\mathbf{A}| \neq 0. \tag{3.29}$$

By inserting the equation of the determinant, it can be rewritten

$$|\mathbf{A}| = \left(Q(t_e^+) + i_s^+ \Delta t^+\right) \Delta i^- - \left(Q(t_e^-) + i_s^- \Delta t^-\right) \Delta i^+ \neq 0, \tag{3.30}$$

and

$$\frac{\left(Q(t_e^+) + i_s^+ \Delta t^+\right)}{\Delta t^+} \Delta t^+ \Delta i^- - \frac{\left(Q(t_e^-) + i_s^- \Delta t^-\right)}{\Delta t^-} \Delta t^- \Delta i^+ \neq 0. \tag{3.31}$$

The mean value of the current during the positive voltage pulse is defined as

$$i_{mean}^+ = \frac{1}{\Delta t^+} \int_{t_s^+}^{t_e^+} i_s(t) dt = \frac{Q(t_e^+) + i_s^+ \Delta t^+}{\Delta t^+}, \tag{3.32}$$

and analogously the mean value of the current during the negative voltage pulse as

$$i_{mean}^- = \frac{1}{\Delta t^-} \int_{t_s^-}^{t_e^-} i_s(t) dt = \frac{Q(t_e^-) + i_s^- \Delta t^-}{\Delta t^-}. \tag{3.33}$$

Thus, the inequivalence 3.31 can be rewritten as:

$$i_{mean}^+ \Delta t^+ \Delta i^- - i_{mean}^- \Delta t^- \Delta i^+ \neq 0. \tag{3.34}$$

The evaluation of the Equation 3.31 can become cumbersome due to the consideration of all possible working points. Thus, it will be evaluated for different cases:

Static case In the static case, the mean current remains constant over time. Consequently, the mean current remains the same for both voltage pulses

$$i_{mean} = i^{+}_{mean} = i^{-}_{mean}, \tag{3.35}$$

and, hence, the current difference in the current ripple remains the same since the mean current stays constant :

$$\Delta i = \Delta i^{+} = \Delta i^{-}. \tag{3.36}$$

Consequently, the determinant can be simplified to

$$|\mathbf{A}| = i^{+}_{mean}\Delta t^{+}\Delta i^{-} - i^{-}_{mean}\Delta t^{-}\Delta i^{+} \neq 0, \tag{3.37}$$

which results into the condition for identifiability in the static case:

$$\Rightarrow i_{mean}\Delta i\left(\Delta t^{+} - \Delta t^{-}\right) \neq 0. \tag{3.38}$$

In practice, the left term can become zero in the following scenarios:

1. $i_{mean} = 0$: the fundamental mean current is zero in the actuator, which is true for $\alpha = 0.5$ in the static case. Since no mean current is flowing, there exists also no mean voltage drop over the series resistance R_Σ. Thus, R_Σ cannot be identified. In such a case, R_Σ has to be given manually in order to estimate L_Δ.

2. $\Delta i = 0$: there exists no current ripple at all, since the current does not change within one PWM pulse. This can either happen because of a purely resistive load without any inductive behavior or due to the absence of a PWM voltage. For instance, a PWM voltage does not exist for duty cycles of zero or one ($\alpha = 0$ and $\alpha = 1$). In such a case, no persistent excitation is present and the identification of both parameters is not feasible unless a duty cycle in the possible range is applied. In such circumstances the duty cycle needs to be forced.

3. $\Delta t^{+} = \Delta t^{-}$: this case resembles the case of $i_{mean} = 0$, since in static condition the case resembles a duty cycle of $\alpha = 0.5$, which leads to no mean current. Similarly to the case above, R_Σ needs to be given manually when the identification of L_Δ is desired.

Dynamic case While in the static case, the evaluation of the in-equivalence given in Equation 3.31 is simple, for the dynamic case only $\alpha = 0$ and $\alpha = 1$ and $\Delta i^{+} = \Delta i^{-} = 0$ are known conditions where the identification fails. In those cases, no current ripple is present since the PWM is absent. Due to a lack of excitation, the identification of both parameters is not possible.

Similarly to the static case, in the situation where $i^{+}_{mean} = i^{-}_{mean} = 0$, L_{Δ} can only be identified, when the value of R_{Σ} is known. In this case, the voltage drop over the series resistance amounts to zero, thus its determination fails. In contrast to the static case, this condition can be also triggered for a duty cycle $\alpha \neq 0.5$ since the current changes according to the dynamics of the system.

For all other cases, it has to be determined in an online way if the determinant equals to zero. Since the approach is implemented on microprocessors with limited numerical representation, it has to be checked if $|\mathbf{A}|$ is below a certain threshold, that depends on the size of the variables, the quantization performed by the AD converter and the desired accuracy.

With the help of the conditions derived above, it can be evaluated if a precise determination of both parameters is possible. In working points where no PWM is present, the duty cycle needs to be changed for a short time to a value that allows to have voltage pulses with sufficient lengths. This procedure resembles an injection-based method, since voltage pulses have to be inserted externally. Only with such a procedure, the determination of one or both parameters is possible in such working points. In other situations, the incremental inductance can still be identified by the pre-knowledge of R_{Σ}. The identification of this parameter is the main topic in the following section.

3.1.3 Determination of the series resistance

As seen before, in case the mean current $i_{mean} \to 0$ as well as in case of a duty cycle $\alpha = 0.5$ for static applications, the incremental inductance L_{Δ} can still be identified under the knowledge of R_{Σ}. Under such circumstances, the resistance R_{Σ} can be approximated as

$$R_{\Sigma} = R_s + \frac{\partial L_{\Delta}(x)}{\partial x}\frac{\partial x}{\partial t} + R_s \frac{\partial}{\partial x}\left(\frac{L_{\Delta}(x)}{R_p(x)}\right)\frac{\partial x}{\partial t} \approx R_s, \tag{3.39}$$

since, in the considered static cases, the velocity of the actuator can be assumed close to zero $\frac{\partial x}{\partial t} \approx 0$.

Thus, the copper resistance R_s can be used directly and a predetermined value can be stored in memory. In case a condition for non-identifiability is being triggered, the stored value can be used as value for R_{Σ} and the identification of L_{Δ} is still possible. Nevertheless, the value of R_s is strongly temperature-dependent and causes considerable temperature drifting in the position self-sensing, especially if temperature is neglected [53]. This is problematic since electromagnetic actuators are usually driven close to their thermal limits and experience considerable self-heating. Under such use cases, the series resistance R_{Σ} needs to be frequently calculated by using Equation 3.24, additionally by inserting forced test PWM pulses, and stored and updated continuously in memory. Since the estimate of R_Σ has poor SNR especially for small currents, the application of a low-pass filter is desired in order to decrease the noise. The time constant of such a filter τ_f has to be dimensioned bigger than the mechanical time constant τ_m, but smaller than the thermal time constant τ_{th} [51]. Doing so allows to reject components coming from back-induced voltages while remaining a fast tracking of temperature changes.

An alternative to the straight-forward identification is the determination of the series resistance by means of a dedicated least mean squares (LMS) algorithm or by its recursive version, the recursive least squares (RLS) algorithm, that is better suited for online estimation. By applying a forgetting factor, the RLS algorithm is able to track temperature changes while forgetting past values which are not updated anymore or are wrong due to unsuitable operation points. Resistance and, therefore, temperature estimation by means of LMS/RLS algorithms is a well known approach in literature and, thus, reference is made to those works [89, 90].

3.1.4 Sensitivity analysis of measurement errors

In practical applications, sensors and electronic circuits experience tolerances and non-idealities that have an influence on the estimated inductance and resistance, and consequently, to the estimated position. Compared to self-sensing techniques for rotating electrical machines, where the rotor angle gets estimated by evaluating the phase shift of inductance or back-EMF values rather than their absolute amplitude, which makes them inherently robust against measurement uncertainties, this is not applicable to electromagnetic actuators. Position estimation in electromagnetic actuators requires the precise knowledge of the flux, the incremental inductance or the parallel resistance in their absolute value. Thus, it is of interest to analyze the sensitivity of the derived algorithm towards measurement uncertainties. Four types of measurement errors will be analyzed and discussed:

1. Gain errors in the measurement of current and voltage
2. Offset errors in the measurement of current and voltage
3. Gain errors in the IDIM circuit
4. Offset errors in the IDIM circuit

Gain errors in the measurements

The measurement quantities of voltage and current are now influenced by a gain error:

$$\tilde{u}(t) = G_u u(t), \tag{3.40}$$

$$\tilde{i}_s(t) = G_i i_s(t), \tag{3.41}$$

where $\tilde{u}(t)$ and $\tilde{i}_s(t)$ denote the measurements with a gain error of G_u and G_i for voltage and current, respectively. In the estimation Equations 3.24 and 3.25, the measurements influenced by the error can be inserted instead of their original ideal values. Thus, the following linear system is obtained now:

$$\begin{bmatrix} \tilde{U}_{DC}\Delta t^+ \\ -\tilde{U}_{DC}\Delta t^- \end{bmatrix} \approx \underbrace{\begin{bmatrix} \tilde{Q}(t_e^+) + \tilde{i}_s(t_s^+)\Delta t^+ & \tilde{i}_s(t_e^+) - \tilde{i}_s(t_s^+) \\ \tilde{Q}(t_e^-) + \tilde{i}_s(t_s^-)\Delta t^- & \tilde{i}_s(t_e^-) - \tilde{i}_s(t_s^-) \end{bmatrix}}_{\tilde{\mathbf{A}}} \begin{bmatrix} \tilde{R}_\Sigma \\ \tilde{L}_\Delta \end{bmatrix}, \tag{3.42}$$

with the parameters $\tilde{R}_\Sigma$ and $\tilde{L}_\Delta$, that are now influenced by the measurement gain error. Due to the linearity of integrator, Q exhibits the same gain error:

$$\tilde{Q} = G_i Q. \tag{3.43}$$

The determinant of $\tilde{\mathbf{A}}$ exhibits the same gain error:

$$\begin{aligned} |\tilde{\mathbf{A}}| &= \left(\tilde{Q}(t_e^+) + \tilde{i}_s(t_s^+)\Delta t^+\right)\left(\tilde{i}_s(t_e^-) - \tilde{i}_s(t_s^-)\right) - \left(\tilde{Q}(t_e^-) + \tilde{i}_s(t_s^-)\Delta t^-\right)\left(\tilde{i}_s(t_e^+) - \tilde{i}_s(t_s^+)\right) \\ &= G_i^2 \cdot |\mathbf{A}|, \end{aligned} \tag{3.44}$$

and, thus, the determination equations change to

$$\begin{aligned} \tilde{R}_\Sigma &\approx \frac{\tilde{U}_{DC}}{|\tilde{\mathbf{A}}|}\left(\left(\tilde{i}_s(t_e^-) - \tilde{i}_s(t_s^-)\right)\Delta t^+ + \left(\tilde{i}_s(t_e^+) - \tilde{i}_s(t_s^+)\right)\Delta t^-\right) \\ &= \frac{G_u U_{DC}}{|\mathbf{A}|G_i^2} G_i \left(\Delta i^- \Delta t^+ + \Delta i^+ \Delta t^-\right) \\ &= \frac{G_u}{G_i} R_\Sigma, \end{aligned} \tag{3.45}$$

and

$$\begin{aligned}
\tilde{L}_\Delta &\approx -\frac{\tilde{U}_{DC}}{|\tilde{\mathbf{A}}|}\left(\left(\tilde{Q}(t_e^-) + \tilde{i}_s(t_s^-)\Delta t^-\right)\Delta t^+ + \left(\tilde{Q}(t_e^+) + \tilde{i}_s(t_s^+)\Delta t^+\right)\Delta t^-\right) \\
&= -\frac{G_u U_{DC}}{|\mathbf{A}|G_i^2} G_i \left(\left(Q(t_e^-) + i_s(t_s^-)\Delta t^-\right)\Delta t^+ + \left(Q(t_e^+) + i_s(t_s^+)\Delta t^+\right)\Delta t^-\right) \\
&= \frac{G_u}{G_i} L_\Delta. \qquad (3.46)
\end{aligned}$$

It can be seen that a gain error in the measurements of current and voltage lead to a gain error in the estimate of the incremental inductance and series resistance. The gain error in the estimate is proportional to the voltage measurement gain error and inverse proportional to the current measurement gain error. Thus, the accuracy of the estimate can be directly increased by increasing the precision of the measurement , e.g. by providing shunt resistors and voltage dividers with tight tolerances and providing a dedicated calibration routine.

Offset errors in the measurements

Now, an offset error is introduced into the measurements of current and voltages:

$$\tilde{u}_{(}t) = u(t) + u_o(t), \qquad (3.47)$$

$$\tilde{i}_s(t) = i_s(t) + i_o(t), \qquad (3.48)$$

with $u_o(t)$ and $i_o(t)$ being the offset error in the voltage and current measurement, respectively. Due to the offset removal in the analog electronics, the integral $Q(t)$ does not exhibit an offset error:

$$\tilde{Q}(t) = Q(t). \qquad (3.49)$$

By inserting the error-influenced quantities into the estimation Equations 3.24 and 3.25, one obtains:

$$\begin{bmatrix} \tilde{U}_{DC}\Delta t^+ \\ -\tilde{U}_{DC}\Delta t^- \end{bmatrix} \approx \underbrace{\begin{bmatrix} \tilde{Q}(t_e^+) + \tilde{i}_s(t_s^+)\Delta t^+ & \tilde{i}_s(t_e^+) - \tilde{i}_s(t_s^+) \\ \tilde{Q}(t_e^-) + \tilde{i}_s(t_s^-)\Delta t^- & \tilde{i}_s(t_e^-) - \tilde{i}_s(t_s^-) \end{bmatrix}}_{\tilde{\mathbf{A}}} \begin{bmatrix} \tilde{R}_\Sigma \\ \tilde{L}_\Delta \end{bmatrix}, \qquad (3.50)$$

and the determinant of the matrix leads to:

$$
\begin{aligned}
|\tilde{\mathbf{A}}| &= \left(\tilde{Q}(t_e^+) + \tilde{i}_s(t_s^+)\Delta t^+\right)\left(\tilde{i}_s(t_e^-) - \tilde{i}_s(t_s^-)\right) - \left(\tilde{Q}(t_e^-) + \tilde{i}_s(t_s^-)\Delta t^-\right)\left(\tilde{i}_s(t_e^+) - \tilde{i}_s(t_s^+)\right) \\
&= \left(Q(t_e^+) + \left(i_s(t_s^+) + i_o\right)\Delta t^+\right)\Delta i^- - \left(Q(t_e^-) + \left(i_s(t_s^-) + i_o\right)\Delta t^-\right)\Delta i^+ \\
&= |\mathbf{A}| + \underbrace{i_0\left(\Delta t^+\Delta i^- - \Delta t^-\Delta i^+\right)}_{A_o}.
\end{aligned}
\tag{3.51}
$$

The parameters can be determined by using:

$$
\begin{aligned}
\tilde{R}_\Sigma &\approx \frac{\tilde{U}_{DC}}{|\tilde{\mathbf{A}}|}\left(\left(\tilde{i}_s(t_e^-) - \tilde{i}_s(t_s^-)\right)\Delta t^+ + \left(\tilde{i}_s(t_e^+) - \tilde{i}_s(t_s^+)\right)\Delta t^-\right) \\
&= \frac{U_{DC} + u_o}{|\mathbf{A}| + A_o}\left(\Delta i^-\Delta t^+ + \Delta i^+\Delta t^-\right) \\
&= \frac{1 + \frac{u_o}{U_{DC}}}{1 + \frac{A_o}{|\mathbf{A}|}} R_\Sigma,
\end{aligned}
\tag{3.52}
$$

and

$$
\begin{aligned}
\tilde{L}_\Delta &\approx -\frac{\tilde{U}_{DC}}{|\tilde{\mathbf{A}}|}\left(\left(\tilde{Q}(t_e^-) + \tilde{i}_s(t_s^-)\Delta t^-\right)\Delta t^+ + \left(\tilde{Q}(t_e^+) + \tilde{i}_s(t_s^+)\Delta t^+\right)\Delta t^-\right) \\
&= -\frac{U_{DC} + u_o}{|\mathbf{A}| + A_o}\left(\left(Q(t_e^-) + i_s(t_s^-)\Delta t^-\right)\Delta t^+ + \left(Q(t_e^+) + i_s(t_s^+)\Delta t^+\right)\Delta t^- + 2 i_o \Delta t^- \Delta t^+\right) \\
&= \frac{1 + \frac{u_o}{U_{DC}}}{1 + \frac{A_o}{|\mathbf{A}|}}\left(L_\Delta - 2\frac{U_{DC}}{|\mathbf{A}|} i_o \Delta t^- \Delta t^+\right) \\
&= \frac{1 + \frac{u_o}{U_{DC}}}{1 + \frac{A_o}{|\mathbf{A}|}} L_\Delta - 2\frac{U_{DC} + u_0}{|\mathbf{A}| + A_o} i_o \Delta t^- \Delta t^+.
\end{aligned}
\tag{3.53}
$$

It is visible that the estimation of the series resistance exhibits only a gain error, that depends on the value of the offset errors. Nevertheless, the incremental inductance exhibits a gain error and a strong offset error. This makes the implementation of a calibration routine and the application of components with low offset necessary.

Gain error in the integrator circuit

In this section, a gain error in the integrator circuit is considered:

$$
\tilde{Q}(t) = G_{RC} Q(t) = \left(1 + \Delta G_{RC}\right) Q(t),
\tag{3.54}
$$

with G_{RC} being the gain error in the integrator stage. For easier mathematical treatment, the term ΔG_{RC} is placed there, that allows separating the error-influenced from the error-free quantities. In the estimation process, the linear system of equations changes to:

$$\begin{bmatrix} U_{DC}\Delta t^+ \\ -U_{DC}\Delta t^- \end{bmatrix} \approx \underbrace{\begin{bmatrix} \tilde{Q}(t_e^+) + i_s(t_s^+)\Delta t^+ & \Delta i^+ \\ \tilde{Q}(t_e^-) + i_s(t_s^-)\Delta t^- & \Delta i^- \end{bmatrix}}_{\tilde{\mathbf{A}}} \begin{bmatrix} \tilde{R}_\Sigma \\ \tilde{L}_\Delta \end{bmatrix}, \tag{3.55}$$

while the calculation of the determinant leads to:

$$\begin{aligned} |\tilde{\mathbf{A}}| &= \left(\tilde{Q}(t_e^+) + i_s(t_s^+)\Delta t^+\right)\left(\Delta i^-\right) - \left(\tilde{Q}(t_e^-) + i_s(t_s^-)\Delta t^-\right)\left(\Delta i^+\right) \\ &= |\mathbf{A}| + \Delta G_{RC}\left(Q(t_e^+)\Delta i^- - Q(t_e^-)\Delta i^+\right). \end{aligned} \tag{3.56}$$

The estimation of the parameter is now affected by the gain error:

$$\begin{aligned} \tilde{R}_\Sigma &\approx \frac{U_{DC}}{|\tilde{\mathbf{A}}|}\left(\left(\Delta i^-\right)\Delta t^+ + \left(\Delta i^+\right)\Delta t^-\right) \\ &= \frac{1}{1 + \frac{\Delta G_{RC}\left(Q(t_e^+)\Delta i^- - Q(t_e^-)\Delta i^+\right)}{|\mathbf{A}|}} R_\Sigma, \end{aligned} \tag{3.57}$$

$$\begin{aligned} \tilde{L}_\Delta &\approx -\frac{U_{DC}}{|\tilde{\mathbf{A}}|}\left(\left(\tilde{Q}(t_e^-) + i_s(t_s^-)\Delta t^-\right)\Delta t^+ + \left(\tilde{Q}(t_e^+) + i_s(t_s^+)\Delta t^+\right)\Delta t^-\right) \\ &= \frac{1}{1 + \frac{\Delta G_{RC}\left(Q(t_e^+)\Delta i^- - Q(t_e^-)\Delta i^+\right)}{|\mathbf{A}|}} L_\Delta \\ &\quad - \frac{U_{DC}}{|\mathbf{A}| + \Delta G_{RC}\left(Q(t_e^+)\Delta i^- - Q(t_e^-)\Delta i^+\right)} \Delta G_{RC}\left(Q(t_e^-)\Delta t^+ + Q(t_e^+)\Delta t^-\right). \end{aligned} \tag{3.58}$$

As calculated above, a gain error in the integrator circuit leads to a gain error of the series resistance. Nevertheless, this gain error is not constant, but depends on the actual value of the integrator and the current differences Δi^+ and Δi^-, making compensation complicated. The same applies to the estimation of the incremental inductance, that additionally exhibits an offset error, which is also not constant. Thus, a gain error in the integrator represents a major challenge in the design process and needs to be carefully considered. As described in Chapter 4, realizing the circuit in Switched Capacitor (SC) technology reduces drastically the tolerances of the integration gain.

Offset error in the integrator circuit

Finally, an offset error in the integration stage is being considered by:

$$\tilde{Q}(t) = Q(t) + Q_o, \tag{3.59}$$

where Q_o is a constant offset. In this case, the determinant yields:

$$\begin{aligned} |\tilde{\mathbf{A}}| &= \left(\tilde{Q}(t_e^+) + i_s(t_s^+)\Delta t^+\right)\Delta i^- - \left(\tilde{Q}(t_e^-) + i_s(t_s^-)\Delta t^-\right)\Delta i^+ \\ &= |\mathbf{A}| + Q_o\left(\Delta i^- - \Delta i^+\right). \end{aligned} \tag{3.60}$$

Inserting the determinant into the estimation equations, one can see the influence of the error:

$$\begin{aligned} \tilde{R}_\Sigma &\approx \frac{U_{DC}}{|\tilde{\mathbf{A}}|}\left(\Delta i^-\Delta t^+ + \Delta i^+\Delta t^-\right) \\ &= \frac{1}{1 + \frac{Q_o(\Delta i^- - \Delta i^+)}{|\mathbf{A}|}} R_\Sigma, \end{aligned} \tag{3.61}$$

$$\begin{aligned} \tilde{L}_\Delta &\approx -\frac{U_{DC}}{|\tilde{\mathbf{A}}|}\left(\left(\tilde{Q}(t_e^-) + i_s(t_s^-)\Delta t^-\right)\Delta t^+ + \left(\tilde{Q}(t_e^+) + i_s(t_s^+)\Delta t^+\right)\Delta t^-\right) \\ &= \frac{1}{1 + \frac{Q_o(\Delta i^- - \Delta i^+)}{|\mathbf{A}|}} L_\Delta - \frac{U_{DC}}{|\mathbf{A}| + Q_o\left(\Delta i^- - \Delta i^+\right)} Q_o\left(\Delta t^+ + \Delta t^-\right). \end{aligned} \tag{3.62}$$

In this case, also a gain error appears in the estimate of the series resistance, that depends on the value of the actual current differences. When the actuator is driven in static conditions, this gain error vanishes. The same applies to the gain error of the incremental inductance. An additional offset error is present inside the incremental inductance, that scales with the actual current differences and the time instant.

3.2 Simplified Self-sensing based on the incremental inductance for static cases

In Section 3.1, the IDIM technique in its full formulation has been derived, analyzed and discussed thoroughly. The technique can cover dynamic as well as static use cases. But not in every application an estimation of the actuator position is needed with high dynamics. Actuators used for positioning applications or actuators with switching behavior and dedicated end positions are not always driven with the full current dynamic. In fact, mostly the position information is required after the actuator has performed its movement, so that the current is almost quasi-static. These conditions allow to make further assumptions on the actuator dynamics and on the shape of the current ripple, so that an IDIM technique with less measurement and calculation effort can be formulated for such application scenarios.

In quasi-static conditions, the influence of the eddy currents can be neglected since the current inside the actuator does not change. Only the eddy currents that are generated by the PWM switching are present and occur at the beginning of each voltage pulse. For the following calculations, the eddy currents are therefore neglected by setting $R_p \to \infty$. Additionally, for quasi-static applications, the fundamental mean current does not change quickly. Consequently, the current differences are assumed to be equal: $\Delta i^+ = \Delta i^-$, which allows assumptions on the current ripple. In such a case, the rising and the falling slope of the current ripple are the same and, therefore, the integration can take place over the complete PWM period (resembling a dual slope integration). Thus, the reset signal can be modified in such a way that only one pulse at the beginning of the PWM period is required:

$$r(t) = \begin{cases} 1 & \text{for} \quad 0 \leq t \leq t_r \\ 0 & \text{else} \end{cases}, \tag{3.63}$$

where the waiting time can be chosen in such a way that it is small enough for the integration capacitance to be reset: $t_r \to 0$. For the simplified version of the IDIM technique, also the resistance effect is neglected, that is responsible for the current ripple being exponentially shaped. Thus, the exponential function of the current ripple of Equation 2.81 can be approximated by a Taylor series where terms above the first order are truncated:

$$e^{-\frac{R_\Sigma}{L_\Delta} t} \approx 1 - \frac{R_\Sigma}{L_\Delta} t. \tag{3.64}$$

Inserting this approximation into the expression of the current ripple from Equation 2.81, yields.

$$i_s(t) \approx \begin{cases} i_0 + \left(\frac{U_{DC}}{R_\Sigma} - i_0 \right) \dfrac{R_\Sigma}{L_\Delta} t & \text{for} \quad 0 \leq t \leq t_* \\ i_s(t_*) + \left(\frac{-U_{DC}}{R_\Sigma} - i_s(t_*) \right) \dfrac{R_\Sigma}{L_\Delta} (t - t_*) & \text{for} \quad t_* \leq t \leq t_{pwm} \end{cases}, \tag{3.65}$$

with

$$i_s(t_*) = i_0 + \left(\frac{U_{DC}}{R_\Sigma} - i_0 \right) \frac{R_\Sigma}{L_\Delta} t_*. \tag{3.66}$$

The impact of the approximation can be seen in Figure 3.6, where a simulation case is shown. The original current ripple according to Equation 2.81 is shown in comparison to the current ripple that is approximated by a Taylor series of the first and second order.

It is visible that the slope of the ripple, which mainly contains the information about the incremental inductance, is almost the same for the middle parts per each voltage pulse of the current ripple.

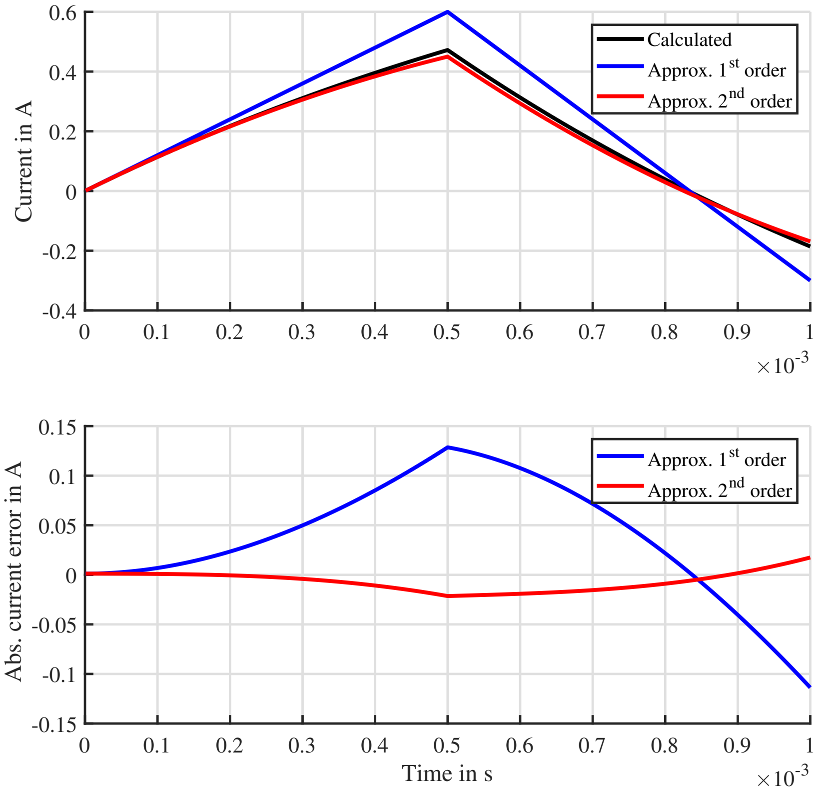

Figure 3.6: Current ripple approximation and resulting approximation errors. Simulated for $R_\Sigma = 10\ \Omega$, $L_\Delta = 10$ mH, $f_{PWM} = 1$ kHz and $U_{DC} = 12$ V.

The next section covers the derivation of the IDIM technique with these assumptions, that will be referred to as Simplified IDIM technique. Two possible realizations of this approach are shown, which depend on the use case: the first realization utilizes the same circuitry as described by Figure 3.4 consisting of an SH-stage, a subtraction stage and an integrator. Thus, this realization makes usage of the same electronics but uses simplified calculations. Nevertheless, the SH-stage is complicated to be implemented in practice and can exhibit aliasing effects when its sampling is triggered on a noisy current measurement. For this reason, another realization method is presented that avoids a SH-stage and uses a high-pass filter for the removal of the fundamental current. Both techniques are introduced, derived and discussed in detail.

3.2.1 Derivation of the estimation equations

Scenario 1: Sample-and-Hold based offset-elimination

In this scenario, the same IDIM circuitry as shown before in Figure 3.4 is used, consisting of a sample-and-hold stage, a subtraction stage and the resettable integrator circuit. Figure 3.7 shows the curves of the sensed current, the offset-free current, the reset trigger and the resulting integral along with its measurement time instants. In this scenario, only one reset pulse at the beginning of the PWM period is necessary and only one measurement at the end of the PWM period is required for the estimation of the incremental inductance.

In the following, the estimation equation for the incremental inductance is derived. Applying the offset-removing stage allows to eliminate the fundamental current from Equation 2.81:

$$\bar{i}_s(t) \approx \begin{cases} \left(\frac{U_{DC}}{R_\Sigma} - i_0\right)\frac{R_\Sigma}{L_\Delta} t & \text{for} \quad 0 \le t \le t_* \\ \left(i_s(t_*) - i_0\right) + \left(\frac{-U_{DC}}{R_\Sigma} - i_s(t_*)\right)\frac{R_\Sigma}{L_\Delta}\left(t - t_*\right) & \text{for} \quad t_* \le t \le t_{pwm} \end{cases}. \tag{3.67}$$

where $\bar{i}_s(t)$ denotes the current ripple without its fundamental component. Replacing the current $i_s(t_*)$ yields:

$$\bar{i}_s(t) \approx \begin{cases} \left(\frac{U_{DC}}{R_\Sigma} - i_0\right)\frac{R_\Sigma}{L_\Delta} t & \text{for} \quad 0 \le t \le t_* \\ \left(\frac{U_{DC}}{R_\Sigma} - i_0\right)\frac{R_\Sigma}{L_\Delta} t_* + \left(\frac{-U_{DC}}{R_\Sigma} - i_s(t_*)\right)\frac{R_\Sigma}{L_\Delta}\left(t - t_*\right) & \text{for} \quad t_* \le t \le t_{pwm} \end{cases}. \tag{3.68}$$

This equation can be simplified using conditions of quasi-static operation. The PWM is able to set a mean driving voltage u_{mean} by adjusting the duty cycle α. The effective driving voltage can be calculated by applying the mean value to the PWM voltage:

$$u_{mean} = \frac{1}{t_{pwm}} \int_0^{t_{pwm}} u(t)dt = 2U_{DC}\left(\alpha - 0.5\right), \tag{3.69}$$

such that a direct relationship between voltage and duty cycle α can be obtained. For quasi-static conditions, the mean current in the actuator follows the mean voltage and can be approximated as:

$$i_{mean} \approx \frac{u_{mean}}{R_\Sigma} = \frac{2U_{DC}\left(\alpha - 0.5\right)}{R_\Sigma}. \tag{3.70}$$

This approximation holds for static currents or for currents with dynamics that are considerably slower than the electrical time constant τ_{el} of the electromagnetic actuator.

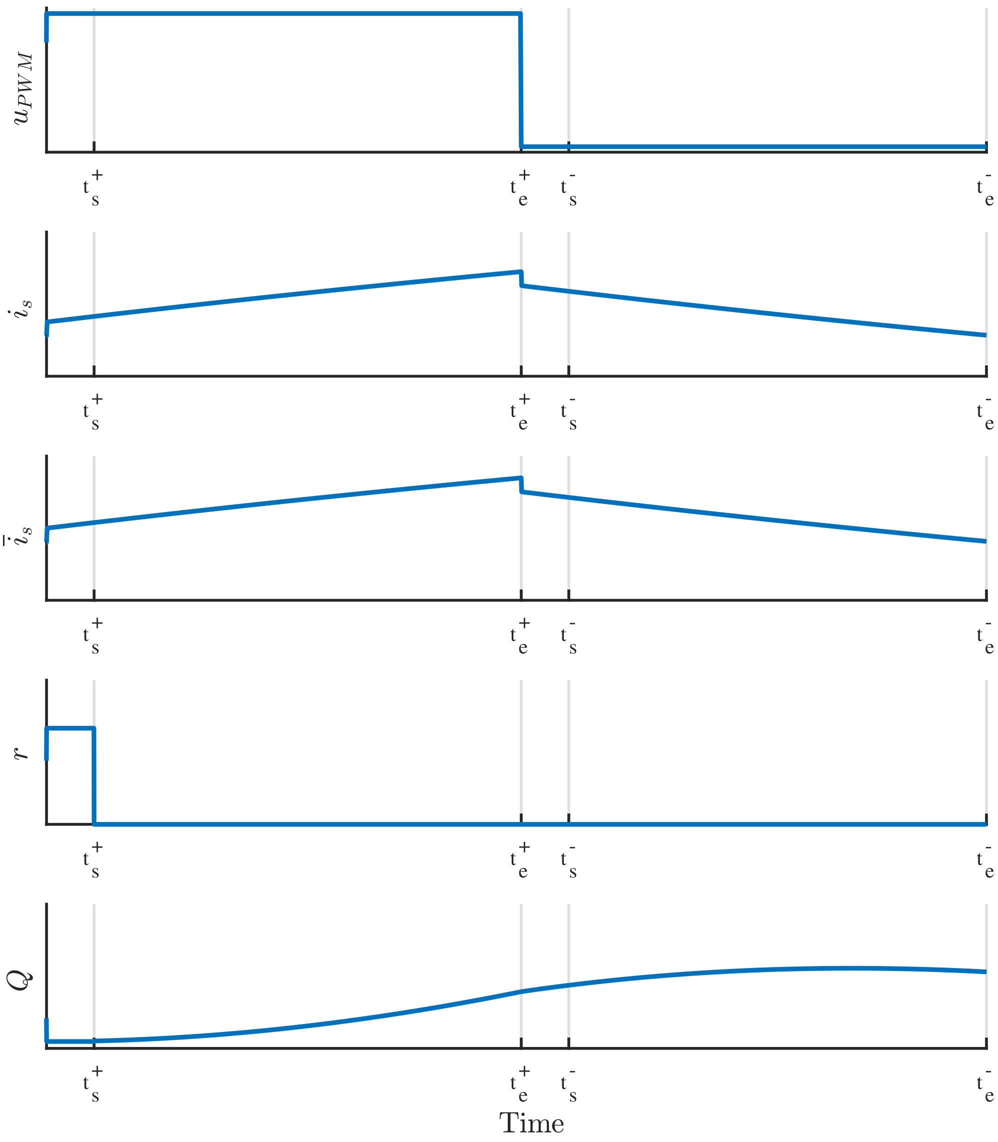

Figure 3.7: Integral signal $Q(t)$ and reset signal $r(t)$ applied on the offset removed current ripple $\bar{i}_s$ of an electromagnetic actuator for the simplified IDIM technique along with critical time instants.

In such a case, a proportional relationship between mean current and duty cycle is obtained. Furthermore, it can be assumed that the current ripple has a low amplitude compared to the mean current, so that the current at the beginning and at the middle of the PWM period can be approximated by the mean value of the current:

$$i_{mean} \approx i_0 \approx i_s(t_*). \tag{3.71}$$

Such approximation holds since the PWM frequency is chosen in such a way that the current ripple is minimized in order to decrease the generation of acoustic noise, force ripples and energy losses. By applying all the assumptions made, the expression of the offset-free current ripple can be simplified as:

$$\begin{aligned}
\bar{i}_s(t) &\approx \begin{cases} \left(\frac{U_{DC}}{R_\Sigma} - \frac{2U_{DC}(\alpha-0.5)}{R_\Sigma}\right)\frac{R_\Sigma}{L_\Delta}t & \text{for} \quad 0 \leq t \leq t_* \\ \left(\frac{U_{DC}}{R_\Sigma} - \frac{2U_{DC}(\alpha-0.5)}{R_\Sigma}\right)\frac{R_\Sigma}{L_\Delta}t_* + \left(\frac{-U_{DC}}{R_\Sigma} - \frac{2U_{DC}(\alpha-0.5)}{R_\Sigma}\right)\frac{R_\Sigma}{L_\Delta}(t-t_*) & \text{for} \quad t_* \leq t \leq t_{pwm} \end{cases} \\
&= \begin{cases} \frac{2U_{DC}}{L_\Delta}(1-\alpha)\,t & \text{for} \quad 0 \leq t \leq t_* \\ \frac{2U_{DC}}{L_\Delta}(1-\alpha)\,t_* - \frac{2U_{DC}}{L_\Delta}\alpha\,(t-t_*) & \text{for} \quad t_* \leq t \leq t_{pwm} \end{cases}.
\end{aligned} \tag{3.72}$$

By having a simplified expression of the current ripple, the integral and its dependency on the incremental inductance can now be calculated. The integral over the offset-free linearized current ripple can be splitted into two parts representing the positive and negative voltage pulses:

$$\begin{aligned}
Q(t_{pwm}) &= \int_0^{t_{pwm}} \bar{i}_s(t)dt \\
&= \int_0^{t_*} \bar{i}_s(t)dt + \int_{t_*}^{t_{pwm}} \bar{i}_s(t)dt,
\end{aligned} \tag{3.73}$$

which can be treated separately. The calculation for the rising part leads to:

$$\begin{aligned}
\int_0^{t_*} \bar{i}_s(t)dt &= \int_0^{t_*} \frac{2U_{DC}}{L_\Delta}(1-\alpha)\,tdt \\
&= \frac{2U_{DC}}{L_\Delta}(1-\alpha)\left[\frac{1}{2}t^2\right]_0^{t_*} \\
&= \frac{U_{DC}}{L_\Delta}(1-\alpha)\,t_*^2,
\end{aligned} \tag{3.74}$$

and for the falling part to:

$$\begin{aligned}
\int_{t_*}^{t_{pwm}} \bar{i}_s(t)dt &= \int_{t_*}^{t_{pwm}} \left(\frac{2U_{DC}}{L_\Delta}(1-\alpha)\,t_* - \frac{2U_{DC}}{L_\Delta}\alpha\,(t-t_*)\right)dt \\
&= \frac{2U_{DC}}{L_\Delta}(1-\alpha)\,t_*\,[t]_{t_*}^{t_{pwm}} - \frac{2U_{DC}}{L_\Delta}\alpha\left[\frac{1}{2}(t-t_*)^2\right]_{t_*}^{t_{pwm}} \\
&= \frac{2U_{DC}}{L_\Delta}(1-\alpha)\,t_*\left(t_{pwm}-t_*\right) - \frac{U_{DC}}{L_\Delta}\alpha\left(t_{pwm}-t_*\right)^2 \\
&= \frac{2U_{DC}}{L_\Delta}t_*^2(1-\alpha)^2 - \frac{U_{DC}}{L_\Delta}t_*^2(1-\alpha)^2 \\
&= \frac{U_{DC}}{L_\Delta}t_*^2(1-\alpha)^2\,. \qquad (3.75)
\end{aligned}$$

Finally, the complete integral can be expressed as

$$\begin{aligned}
Q(t_{pwm}) &= \int_0^{t_*}\bar{i}_s(t)dt + \int_{t_*}^{t_{pwm}}\bar{i}_s(t)dt \\
&= \frac{U_{DC}}{L_\Delta}(1-\alpha)\,t_*^2 + \frac{U_{DC}}{L_\Delta}t_*^2(1-\alpha)^2 \\
&= \frac{U_{DC}}{L_\Delta}t_{pwm}^2\alpha\,(1-\alpha)\,. \qquad (3.76)
\end{aligned}$$

Algebraic manipulation leads to the estimation equation for the incremental inductance:

$$L_\Delta \approx \frac{U_{DC}}{Q(t_e^-)}t_{pwm}^2\cdot\alpha\cdot(1-\alpha)\,. \qquad (3.77)$$

For the simplified IDIM methods, only one voltage measurement and one integral measurement per PWM period are necessary, which results into a decreased measurement effort. Moreover, the estimation process requires less mathematical operations than in the case of the complete IDIM technique and avoids the usage of current differences that decrease the SNR.

Scenario 2: High-pass filter based offset-elimination

The second realization form of the simplified IDIM technique relies on a different analog circuitry that is easier to implement. The circuit depicted in Figure 3.8 consists of a high-pass (HP) filter, a full bridge active rectifier (FAR) and the resettable integrator circuit. The high-pass filter allows to remove the fundamental current component without the usage of a dedicated sample-and-hold stage. Thus, it is easier to implement and shows no droop effects due to a leakage of the sampling capacitance. Nevertheless, the choice of a proper cut-off frequency is important since a good trade-off must be made between the elimination of the DC component and possible bandwidth reduction in the movement of the actuator. In the following, the time constant of the high-pass filter $\tau_{HP} = \frac{1}{f_{HP}}$ is placed far away from the mechanical time constant, but still below the PWM time period ($\tau_m \ll \tau_{HP} \ll t_{pwm}$). Since the high-pass filter completely removes the mean value from the current ripple, the integration would lead to a zero value. Consequently, the current ripple needs to be rectified so that a non-zero integration takes place. In the circuit, a full bridge active rectifier is used for this purpose, similarly to the work [54]. Then, the resettable integrator circuit can integrate the filtered and rectified signal. Compared to the application scenario above, this realization needs a modified analog circuit than the original IDIM technique, but this circuit is easier to implement due to the absence of a sampling stage. Furthermore, the avoidance of sampling significantly increases the SNR of this solution since noise cannot be sampled, and, consequently, no aliasing effects can occur.

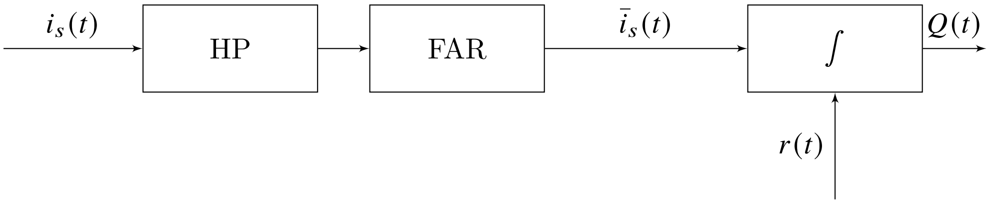

Figure 3.8: IDIM measurement chain consisting of a high-pass filter- and rectifier-based offset removal stage.

In the following, the estimation procedure for this approach is derived. First, the linearized current ripple from Equation 3.65 is considered. The mean value of the current ripple can be calculated as:

$$i_s^0 = \frac{Q(t_{pwm})}{t_{pwm}} = \frac{U_{DC}}{L_\Delta}\alpha\,(1-\alpha)\,t_{pwm}, \tag{3.78}$$

where i_s^0 denotes the mean value of the current ripple (without its fundamental component). The mean value of the current ripple itself represents the half of its amplitude under the assumption of a purely linear current ripple:

$$i_s^0 = \frac{\bar{i}_s(t_*)}{2}. \tag{3.79}$$

Starting from the linearized expression 3.65, applying the high frequency filter eliminates all dc components. Consequently, i_0 and i_s^0 are removed from the high-pass filtered current i_{HP}:

$$\begin{aligned} i_{HP}(t) &= \bar{i}_s(t) - i_0 - i_s^0 \\ &\approx \begin{cases} \left(\frac{U_{DC}}{R_\Sigma} - i_0\right) \frac{R_\Sigma}{L_\Delta} t - i_s^0 & \text{for } 0 \le t \le t_* \\ \left(\frac{U_{DC}}{R_\Sigma} - i_0\right) \frac{R_\Sigma}{L_\Delta} t_* + \left(\frac{-U_{DC}}{R_\Sigma} - i_s(t_*)\right) \frac{R_\Sigma}{L_\Delta} (t - t_*) - i_s^0 & \text{for } t_* \le t \le t_{pwm} \end{cases} . \end{aligned} \tag{3.80}$$

Applying the simplifications from Equations 3.70 and 3.71 and inserting the mean value of the current ripple leads to:

$$i_{HP}(t) \approx \begin{cases} \frac{2U_{DC}}{L_\Delta} (1-\alpha) t - \frac{U_{DC}}{L_\Delta} \alpha (1-\alpha) t_{pwm} & \text{for} \quad 0 \le t \le t_* \\ \frac{U_{DC}}{L_\Delta} (1-\alpha) t_* - \frac{2U_{DC}}{L_\Delta} \alpha (t - t_*) & \text{for} \quad t_* \le t \le t_{pwm} \end{cases} , \tag{3.81}$$

which can be further simplified to

$$i_{HP}(t) \approx \frac{U_{DC}}{L_\Delta} \begin{cases} 2(1-\alpha) t - \alpha (1-\alpha) t_{pwm} & \text{for} \quad 0 \le t \le t_* \\ (1-\alpha) t_* - 2\alpha (t - t_*) & \text{for} \quad t_* \le t \le t_{pwm} \end{cases} . \tag{3.82}$$

In a further step, the high-pass filtered current gets rectified by the full active rectifier:

$$\bar{i}_s(t) = i_{FAR}(t) = |i_{HP}(t)|, \tag{3.83}$$

where i_{FAR} denotes the rectified current ripple. A rectification leads to a signal, where all negative components are mirrored along the x-axis. Thus, in order to describe mathematically the signal, not only two cases (namely the positive and negative voltage pulses), but four cases are necessary. The condition for those cases can by determined by calculating the crossing points of the signal with the x-axis. Considering the first expression for the positive voltage pulse:

$$2(1-\alpha) t - \alpha (1-\alpha) t_{pwm} \overset{!}{=} 0, \tag{3.84}$$

leads to the first crossing point $t_1 = \frac{1}{2} t_*$. Evaluating the equation for the negative voltage pulse:

$$(1-\alpha) t_* - 2\alpha (t - t_*) \overset{!}{=} 0, \tag{3.85}$$

leads to the second crossing point $t_2 = \frac{1}{2} (\alpha + 1) t_{pwm}$. Thus, the rectifier output can be mathematically expressed as:

$$\begin{aligned}
\bar{i}_s(t) &\approx \frac{U_{DC}}{L_\Delta} \begin{cases} \left|2\left(1-\alpha\right)t - \alpha\left(1-\alpha\right)t_{pwm}\right| & \text{for} \quad 0 \leq t \leq \frac{1}{2}t_* \\ 2\left(1-\alpha\right)t - \alpha\left(1-\alpha\right)t_{pwm} & \text{for} \quad \frac{1}{2}t_* \leq t \leq t_* \\ \left(1-\alpha\right)t_* - 2\alpha\left(t-t_*\right) & \text{for} \quad t_* \leq t \leq \frac{1}{2}\left(\alpha+1\right)t_{pwm} \\ \left|\left(1-\alpha\right)t_* - 2\alpha\left(t-t_*\right)\right| & \text{for} \quad \frac{1}{2}\left(\alpha+1\right)t_{pwm} \leq t \leq t_{pwm} \end{cases} \\
&\approx \frac{U_{DC}}{L_\Delta} \begin{cases} -2\left(1-\alpha\right)t + \alpha\left(1-\alpha\right)t_{pwm} & \text{for} \quad 0 \leq t \leq \frac{1}{2}t_* \\ 2\left(1-\alpha\right)t - \alpha\left(1-\alpha\right)t_{pwm} & \text{for} \quad \frac{1}{2}t_* \leq t \leq t_* \\ \left(1-\alpha\right)t_* - 2\alpha\left(t-t_*\right) & \text{for} \quad t_* \leq t \leq \frac{1}{2}\left(\alpha+1\right)t_{pwm} \\ -\left(1-\alpha\right)t_* + 2\alpha\left(t-t_*\right) & \text{for} \quad \frac{1}{2}\left(\alpha+1\right)t_{pwm} \leq t \leq t_{pwm} \end{cases} . \qquad (3.86)
\end{aligned}$$

The output of the rectifier serves as input for the integrator stage, which is calculated with respect to the four cases of Equation 3.86:

$$\begin{aligned}
Q(t_{pwm}) &= \int_0^{t_{pwm}} \bar{i}_s(t)dt \\
&= \int_0^{\frac{1}{2}t_*} \bar{i}_s(t)dt + \int_{\frac{1}{2}t_*}^{t_*} \bar{i}_s(t)dt + \int_{t_*}^{\frac{1}{2}(\alpha+1)t_{pwm}} \bar{i}_s(t)dt + \int_{\frac{1}{2}(\alpha+1)t_{pwm}}^{t_{pwm}} \bar{i}_s(t)dt. \qquad (3.87)
\end{aligned}$$

The calculation of the individual integrals leads to the following expressions. For sake of brevity intermediate steps have been hidden:

$$\begin{aligned}
\int_0^{\frac{1}{2}t_*} \bar{i}_s(t)dt &= \frac{U_{DC}}{L_\Delta}\left(1-\alpha\right)\int_0^{\frac{1}{2}t_*}\left(-2t+t_*\right)dt \\
&= \frac{U_{DC}}{L_\Delta}\left(1-\alpha\right)\left[-t^2+t_*t\right]_0^{\frac{1}{2}t_*} \\
&= \frac{U_{DC}}{L_\Delta}\left(1-\alpha\right)\left(-\frac{1}{4}\alpha^2t_{pwm}^2+\frac{1}{2}\alpha^2t_{pwm}^2\right) \\
&= \frac{1}{4}\frac{U_{DC}}{L_\Delta}\left(1-\alpha\right)\alpha^2t_{pwm}^2, \qquad (3.88)
\end{aligned}$$

$$
\begin{aligned}
\int_{\frac{1}{2}t_*}^{t_*} \bar{i}_s(t)dt &= \frac{U_{DC}}{L_\Delta}\left(1-\alpha\right)\int_0^{\frac{1}{2}t_*}\left(2t-t_*\right)dt \\
&= \frac{U_{DC}}{L_\Delta}\left(1-\alpha\right)\left[t^2-t_*t\right]_{\frac{1}{2}t_*}^{t_*} \\
&= \frac{U_{DC}}{L_\Delta}\left(1-\alpha\right)\left(\alpha^2t_{pwm}^2-\alpha^2t_{pwm}^2-\frac{1}{4}\alpha^2t_{pwm}^2+\frac{1}{2}\alpha^2t_{pwm}^2\right) \\
&= \frac{1}{4}\frac{U_{DC}}{L_\Delta}\left(1-\alpha\right)\alpha^2t_{pwm}^2,
\end{aligned}
\tag{3.89}
$$

$$
\begin{aligned}
\int_{t_*}^{\frac{1}{2}(\alpha+1)t_{pwm}} \bar{i}_s(t)dt &= \frac{U_{DC}}{L_\Delta}\alpha\int_{t_*}^{\frac{1}{2}(\alpha+1)t_{pwm}}((1-\alpha)t_{pwm}-2(t-t_*))dt \\
&= \frac{U_{DC}}{L_\Delta}\alpha\left[(1-\alpha)t_{pwm}t-(t-t_*)^2\right]_{t_*}^{\frac{1}{2}(\alpha+1)t_{pwm}} \\
&= \frac{U_{DC}}{L_\Delta}\alpha((1-\alpha)t_{pwm}\frac{1}{2}(\alpha+1)t_{pwm}-(\frac{1}{2}(\alpha+1)t_{pwm}-t_*)^2 \\
&- (1-\alpha)t_{pwm}t_*) \\
&= \frac{U_{DC}}{L_\Delta}\alpha(\frac{1}{2}(1-\alpha)(\alpha+1)t_{pwm}^2-(\frac{1}{2}(1-\alpha)t_{pwm})^2-\alpha(1-\alpha)t_{pwm}^2) \\
&= \frac{U_{DC}}{L_\Delta}\alpha(1-\alpha)t_{pwm}^2(\frac{1}{2}(\alpha+1)-\frac{1}{4}(1-\alpha)-\alpha),
\end{aligned}
\tag{3.90}
$$

and

$$
\begin{aligned}
\int_{\frac{1}{2}(\alpha+1)t_{pwm}}^{t_{pwm}} \bar{i}_s(t)dt &= \frac{U_{DC}}{L_\Delta}\alpha\int_{\frac{1}{2}(\alpha+1)t_{pwm}}^{t_{pwm}}(-(1-\alpha)t_{pwm}+2(t-t_*))dt \\
&= \frac{U_{DC}}{L_\Delta}\alpha\left[-(1-\alpha)t_{pwm}t+(t-t_*)^2\right]_{\frac{1}{2}(\alpha+1)t_{pwm}}^{t_{pwm}} \\
&= \frac{U_{DC}}{L_\Delta}\alpha(-(1-\alpha)t_{pwm}t_{pwm}+(t_{pwm}-t_*)^2+(1-\alpha)t_{pwm}\frac{1}{2}(\alpha+1)t_{pwm} \\
&- (\frac{1}{2}(\alpha+1)t_{pwm}-t_*)) \\
&= \frac{U_{DC}}{L_\Delta}\alpha(-(1-\alpha)t_{pwm}^2+(t_{pwm}-t_*)^2+(1-\alpha)t_{pwm}\frac{1}{2}(\alpha+1)t_{pwm} \\
&- (\frac{1}{2}(1-\alpha)t_{pwm})^2) \\
&= \frac{U_{DC}}{L_\Delta}\alpha(1-\alpha)t_{pwm}^2(-1+(1-\alpha)+\frac{1}{2}(\alpha+1)-(\frac{1}{4}(1-\alpha))).
\end{aligned}
\tag{3.91}
$$

Summing all partial integrals into one complete integral yields:

$$
\begin{aligned}
Q(t_{pwm}) &= \int_{0}^{\frac{1}{2}t_*} \bar{i}_s(t)dt + \int_{\frac{1}{2}t_*}^{t_*} \bar{i}_s(t)dt + \int_{t_*}^{\frac{1}{2}(\alpha+1)t_{pwm}} \bar{i}_s(t)dt + \int_{\frac{1}{2}(\alpha+1)t_{pwm}}^{t_{pwm}} \bar{i}_s(t)dt \\
&= \frac{U_{DC}}{L_\Delta}\alpha(1-\alpha)t_{pwm}^2 \\
&\cdot \left(\frac{1}{4}\alpha + \frac{1}{4}\alpha + \frac{1}{2}(\alpha+1) - \frac{1}{4}(1-\alpha) - \alpha - 1 + (1-\alpha) + \frac{1}{2}(\alpha+1) - \frac{1}{4}(1-\alpha)\right) \\
&= \frac{U_{DC}}{L_\Delta}\alpha(1-\alpha)t_{pwm}^2 \cdot \frac{1}{2}. \qquad (3.92)
\end{aligned}
$$

Thus, the expression of the integral can be obtained:

$$
Q(t_{pwm}) = \frac{1}{2} \cdot \frac{U_{DC}}{L_\Delta} \cdot \alpha \cdot (1-\alpha) \cdot t_{pwm}^2. \qquad (3.93)
$$

Finally, the incremental inductance can be identified by:

$$
L_\Delta \approx \frac{1}{2}\frac{U_{DC}}{Q(t_{pwm})}t_{pwm}^2 \cdot \alpha \cdot (1-\alpha)\,. \qquad (3.94)
$$

Compared to the realization scenario 1 described by Equation 3.77, only a factor of $\frac{1}{2}$ is added to the estimation equation of the incremental inductance. Thus, this approach benefits of the same advantages of scenario 1, namely reduced measurement and calculation effort. Due to the usage of a high-pass filter instead of a sample-hold stage, the implementation effort is reduced and the SNR is increased, while its cut-off frequency further reduces the bandwidth of the estimation process.

3.2.2 Sensitivity analysis of the measurement errors

Similarly to Section 3.1.4, the simplified IDIM approach will be analyzed towards possible measurement errors in the sensors and in the integrator circuit. In the following, the definition of the gain and offset errors from Section 3.1.4 is used.

Gain errors in the measurements

In case of voltage and current gain errors, the estimation of the incremental inductance from Equation 3.77 changes to:

$$\begin{aligned}\tilde{L}_\Delta &\approx \frac{\tilde{U}_{DC}}{\tilde{Q}(t_e^-)} t_{pwm}^2 \cdot \alpha \cdot (1-\alpha)\\ &= \frac{G_u}{G_i}\frac{U_{DC}}{Q(t_e^-)} t_{pwm}^2 \cdot \alpha \cdot (1-\alpha)\\ &= \frac{G_u}{G_i} L_\Delta,\end{aligned} \tag{3.95}$$

where the estimate experiences a gain error that is proportional to the voltage gain error and inverse proportional to the current gain error.

Offset errors in the measurements

In the case of offset errors, the integral is not influenced since the offset-elimination stage (either realized by the sample-and-hold stage or by the high-pass filter) removes all offsets:

$$\begin{aligned}\tilde{L}_\Delta &\approx \frac{\tilde{U}_{DC}}{Q(t_e^-)} t_{pwm}^2 \cdot \alpha \cdot (1-\alpha)\\ &= \frac{U_{DC}+u_o}{Q(t_e^-)} t_{pwm}^2 \cdot \alpha \cdot (1-\alpha)\\ &= L_\Delta + \frac{u_o}{Q(t_e^-)} t_{pwm}^2 \alpha (1-\alpha).\end{aligned} \tag{3.96}$$

Consequently, the estimation process is only affected by the voltage offset error, that leads to an offset error that changes with the duty cycle.

Gain error in the integrator circuit

A gain error in the integrator circuit leads to a gain error in the estimate

$$\begin{aligned}\tilde{L}_\Delta &\approx \frac{U_{DC}}{\tilde{Q}(t_e^-)} t_{pwm}^2 \cdot \alpha \cdot (1-\alpha)\\ &= \frac{U_{DC}}{G_{RC} Q(t_e^-)} t_{pwm}^2 \cdot \alpha \cdot (1-\alpha)\\ &= \frac{1}{G_{RC}} L_\Delta,\end{aligned} \tag{3.97}$$

that is inversely proportional to the gain error of the integration stage.

Offset error in the integrator circuit

An offset error in the integration stage changes the estimate of the incremental inductance:

$$\begin{aligned}\tilde{L}_{\Delta} &\approx \frac{U_{DC}}{\tilde{Q}(t_e^-)} t_{pwm}^2 \cdot \alpha \cdot (1-\alpha) \\ &= \frac{U_{DC}}{Q(t_e^-) + Q_o} t_{pwm}^2 \cdot \alpha \cdot (1-\alpha) \\ &= f(L_{\Delta}, Q_o), \end{aligned} \tag{3.98}$$

in such a way, that the value of L_{Δ} is influenced in a nonlinear way. Thus, an offset error in the integration stage must be minimized or actively compensated by calibration.

3.3 Self-sensing based on the eddy currents

As seen within the state-of-the-art in Chapter 1.2, the incremental inductance is the desired parameter that is used for self-sensing the position of electromagnetic actuators. Nevertheless, in actuators which are strongly driven in magnetic saturation, the incremental inductance is not monotonous, thus, a bijective function for a unique position estimation cannot be found. This ambiguity in the position estimation can be solved by using prior knowledge about the actuator position and movement direction, but this approach always needs an initialization procedure with known position. Another parameter that can be used for position estimation is the parallel resistor R_p that represents iron losses inside the actuator. This parameter shows a monotonous behavior over the complete position range, thus it can be used as additional information for solving the ambiguity that is present inside the incremental inductance.

3.3.1 Derivation of the estimation equations

As previously discussed in Chapter 2.5, the eddy current model that is used in this work is of the first order, thus discontinuities are present inside the current ripple at the PWM switching instants. Due to the skin effect, these cusps are smoothed in reality since currents always have a finite slew rate. Nevertheless, the model described in Chapter 2.3 is able to approximate the height of the current cusp with good accuracy and, thus, higher model orders can be avoided with the merit of decreased calculation effort.

Recalling Equations 2.95 and 2.96, the height of the cusp can be easily put into relation to the parallel resistance, thus the estimation equations can be easily derived. The one for the switching instant from negative to positive voltage as:

$$R_p = \frac{2U_{DC}}{h_i^+} - R_\Sigma, \tag{3.99}$$

and the one from the transition from positive to negative voltage as:

$$R_p = \frac{-2U_{DC}}{h_i^-} - R_\Sigma. \tag{3.100}$$

With these equations, the parallel resistance can be calculated with few mathematical operations. Nevertheless, the value of R_Σ needs to be known in order to compensate for changes during self-heating as well as induced components during movement. Moreover, the practical implementation of this approach suffers from the fact that the height of the current cusps h_i^+ and h_i^- cannot be measured directly, since they happen theoretically at the same time instant. Therefore, the measurement time instants must be set closely enough to the discontinuity, as shown in Figure 3.9.

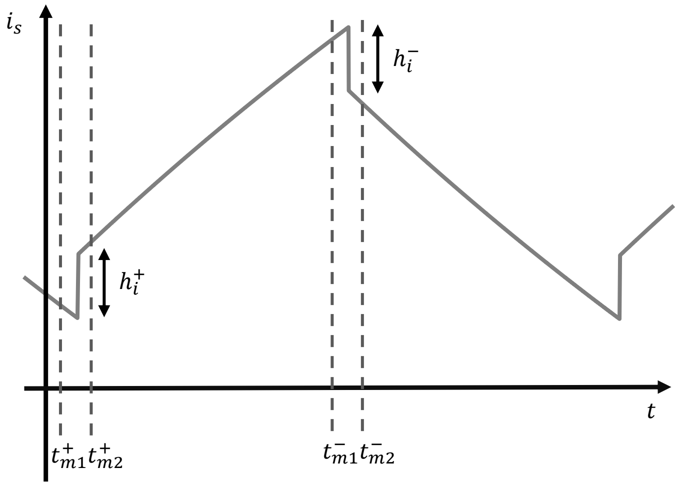

Figure 3.9: Estimation of the parallel resistance by measuring the height of the current cusps, adopted from [66].

Those time instants can be expressed as

$$t_{m1}^+ = -t_\delta, \tag{3.101}$$

$$t_{m2}^+ = t_\delta, \tag{3.102}$$

$$t_{m1}^- = t_* - t_\delta, \tag{3.103}$$

$$t_{m2}^- = t_* + t_\delta, \tag{3.104}$$

with a time delay t_δ, which is relatively small. The choice of t_δ is a trade-off between

SNR and accuracy. At the PWM switching instant, not only the cusps are existent, but also nonlinear effects of the power stage such as ringing and dead-time insertion. Moreover, the current sensor might have bandwidth and slew rate limitation at this time instant and, due to the negligence of the skin effect, not all eddy currents are already generated in all the layers. This motivates the need for increasing t_δ in order to avoid a distorted measurement and wait for the eddy currents to rise. Nevertheless, the longer t_δ, the more time passes, where the current ripple rises due to its inductive behavior and, consequently, the height of the cusp is measured incorrectly. Especially for large t_δ, the influence of the current rise due to the incremental inductance is significant, so that the identification of R_p overlaps with the identification of L_Δ. In such a case, the identified value of R_p also shows a non-monotonous behavior due to the increased estimation error which involves the incremental inductance. Due to its importance, the influence of the measurement time delay is derived and discussed in the next section and a possible method for compensation is shown.

3.3.2 Influence of the measurement time delay

In the following, the measured heights of the current cusps in presence of measurement delays are compared to the ideal height of the current cusps and the resulting identification error is defined. For the rising edge, the measured height yields:

$$\begin{aligned}
\hat{h}_i^+ &= i_s(t_\delta) - i_s(-t_\delta) \\
&= i_0 + \left(\frac{U_{DC}}{R_\Sigma} - i_0\right)\left(1 - e^{-\frac{t_\delta}{\tau_{el}}}\right) - i_0 - \left(\frac{-U_{DC}}{R_\Sigma} - i_0\right)\left(1 - e^{\frac{t_\delta}{\tau_{el}}}\right) + 2\frac{U_{DC}}{R_\Sigma + R_p} e^{\frac{t_\delta}{\tau_{el}}} \\
&\approx \frac{2U_{DC}}{R_\Sigma + R_p} e^{\frac{t_\delta}{\tau_{el}}} \\
&\approx \frac{2U_{DC}}{R_\Sigma + R_p}\left(1 + \frac{t_\delta}{\tau_{el}}\right) \\
&= h_i^+ + \underbrace{\frac{2U_{DC}}{R_\Sigma + R_p} \cdot \frac{t_\delta}{\tau_{el}}}_{e_i^+},
\end{aligned} \tag{3.105}$$

where simplifications where made by applying the Taylor approximation and by assuming a symmetric shape of the current ripple. Thus, the estimate of R_p can be obtained by taking into consideration the measurement error:

$$
\begin{aligned}
R_p &= \frac{2U_{DC}}{h_i^+} - R_\Sigma \\
&= \frac{2U_{DC}}{\hat{h}_i^+ - e_i^+} - R_\Sigma .
\end{aligned} \tag{3.106}
$$

The error can be summarized under the consideration of $R_\Sigma \ll R_p$ as:

$$
e_i^+ = \frac{2U_{DC}}{R_\Sigma + R_p} \frac{t_\delta}{\tau_{el}} = \frac{2U_{DC}}{R_\Sigma + R_p} \frac{t_\delta R_p R_\Sigma}{L_\Delta \left(R_p + R_\Sigma\right)} \approx \frac{2U_{DC} t_\delta R_\Sigma}{R_p L_\Delta}. \tag{3.107}
$$

For the falling edge, the same calculation leads to:

$$
\begin{aligned}
R_p &= \frac{-2U_{DC}}{h_i^-} - R_\Sigma \\
&= \frac{-2U_{DC}}{\hat{h}_i^- - e_i^-} - R_\Sigma .
\end{aligned} \tag{3.108}
$$

Consequently, the error, under simplification of $R_\Sigma \ll R_p$, amounts to:

$$
e_i^- = \frac{-2U_{DC}}{R_\Sigma + R_p} \frac{t_\delta}{\tau_{el}} = \frac{-2U_{DC}}{R_\Sigma + R_p} \frac{t_\delta R_p R_\Sigma}{L_\Delta \left(R_p + R_\Sigma\right)} \approx \frac{-2U_{DC} t_\delta R_\Sigma}{R_p L_\Delta}. \tag{3.109}
$$

The exact knowledge of L_Δ and R_p allows the calculation of an error-free estimation:

$$
R_p = \frac{2U_{DC}}{h_i^+} = \frac{2U_{DC}}{\hat{h}_i^+ - e_i^+} \approx \frac{2U_{DC}}{\hat{h}_i^+ - \frac{2U_{DC} t_\delta R_\Sigma}{R_p L_\Delta}} = \frac{2U_{DC} L_\Delta R_p}{h_i^+ R_p L_\Delta + 2U_{DC} t_\delta R_\Sigma}, \tag{3.110}
$$

which can be solved under the negligence of the solution $R_p = 0$ to

$$
R_p \approx \frac{2U_{DC} L_\Delta - 2U_{DC} t_\delta R_\Sigma}{\hat{h}_i^+ L_\Delta}. \tag{3.111}
$$

For the falling edge, the compensated estimation can be derived in a similar manner as:

$$
R_p \approx \frac{-2U_{DC} L_\Delta - 2U_{DC} t_\delta R_\Sigma}{\hat{h}_i^- L_\Delta}. \tag{3.112}
$$

During the compensation, attention has to be paid on the identified values of R_Σ and L_Δ, which are results of other estimation processes. An error in the estimation of those parameters can lead to a propagation of error, which leads to failure of the compensation.

3.3.3 Sensitivity analysis of measurement errors

Similarly to the techniques described before, also a sensitivity analysis on measurement errors is conducted for the parallel resistor estimator. The same voltage and current gain and offset errors are considered as in Section 3.1.4. In this sensitivity analysis, only the estimator is considered that does not make usage of the compensation of the measurement time delay. When considering the compensation, the identified values of R_Σ and L_Δ need to be known, which are on their own sensitive to measurement error.

Gain errors in the measurements

In the case of gain errors in the voltage and current measurement, the following equation can be obtained

$$\begin{aligned}\tilde{R}_p &\approx \frac{2\tilde{U}_{DC}}{\tilde{h}_i^+} - \tilde{R}_\Sigma \\ &= \frac{2U_{DC}G_u}{h_i^+ G_i} - \frac{G_u}{G_i}R_\Sigma \\ &= \frac{G_u}{G_i}R_p, \end{aligned} \tag{3.113}$$

when the sensitivity analysis of the series resistance R_Σ from Equation 3.24 is inserted. A similar result can be obtained for the estimation of R_p using the falling edge.

Offset errors in the measurements

Since h_i^+ is based on a current difference, an offset in the current measurement has no effect:

$$\begin{aligned}\tilde{R}_p &\approx \frac{2\tilde{U}_{DC}}{h_i^+} - \tilde{R}_\Sigma \\ &= \frac{2U_{DC} + 2u_o}{h_i^+} - \left(1 + \frac{1 + \frac{u_o}{U_{DC}}}{1 + \frac{A_o}{|\mathbf{A}|}}\right)R_\Sigma \\ &= R_p + \frac{2u_o}{h_i^+} + \left(\frac{1 + \frac{u_o}{U_{DC}}}{1 + \frac{A_o}{|\mathbf{A}|}}\right)R_\Sigma. \end{aligned} \tag{3.114}$$

Thus, only a dependence on an offset in the voltage measurement and remaining errors coming from the sensitivity of the series resistance are present in the estimate. A similar result is achieved for the estimation via the falling edge.

3.4 Implementation comparison of the different approaches

In the following, the different IDIM techniques will be compared in terms of implementation effort and use cases. In particular, the number of measurements needed and the number of mathematical operations will be compared in order to evaluate the computational effort of the techniques under observation. Moreover, the simplifications that were made during the derivation and analysis of the techniques are compared, thus giving hints for certain applications scenarios. Based on the error analysis that was made in Sections 3.1 and 3.2, the influence of measurement errors will be compared. This is especially important for practical implementation since the position estimation relies on absolute values of the incremental inductance and, therefore, errors in the measurement of the IDIM technique have a significant effect on the overall position estimation. Also, the SNR is compared in a qualitative manner. The results of this comparison are summarized in Table 3.1.

Measurement effort For the implementation of the IDIM technique shown in Section 3.1, in total 7 measurements need to be obtained, one for the DC link voltage, four for the measurement of the phase current at dedicated time instants and two for the measurement of the integral at dedicated time instants. Especially the triggering of the measurements of the current and the integral is cumbersome to implement since four (respectively two) synchronized measurements within one PWM period have to be triggered. This especially increases the implementation effort on the side of the ADC. For the simplified IDIM techniques derived in Section 3.2, only one DC link voltage measurement and one measurement of the integral at a dedicated time instant need to be performed, which can be easily implemented using standard ADCs. The eddy current estimator relies on a measurement of the DC link voltage as well as two samples of the phase current, that have a tight timing. While the DC link voltage is not problematic to measure, the two consecutive measurements of the current need to be obtained at dedicated time instants which are very close together, thus a high speed ADC or two parallel low-speed ADCs have to be used in order to gather these information.

Number of mathematical operations The IDIM technique in its full implementation requires the most mathematical operations, namely 17 additions, 13 multiplications and 2 divisions in case the series resistance is estimated as well as 5 additions, 3 multiplications and 1 division in case the series resistance is not estimated. The simplified IDIM approaches, on the other hand, only require 1 addition, 5 multiplications and one division. Usually additions and multiplications are the cheapest mathematical operations in microprocessors, while divisions tend to occupy several instructions, such as e.g. in the widely used Cortex ARM microcontrollers [91]. Thus, the simplified IDIM techniques allow an estimation that is computationally lightweight compared to the IDIM technique in its full derivation. The eddy current resistor estimator only relies on 1 addition, multiplication and division, exhibiting the smallest computational effort.

Applied simplifications Concerning the simplifications that were made during the derivation process and that further limit the range of possible applications, the IDIM technique in its full derivation shows the least restrictions. There is the simplification that the PWM period must be considerably smaller then the mechanical time constant and consequently, that the parameters of interest do not change during the time of one PWM pulse. This restriction applies to all techniques that are based on the evaluation of the current ripple [51] and, thus, represents no major limitation. This is also due to the fact that usually the PWM frequency is the highest frequency in the actuator system and all other frequencies, such as sampling frequency of position and current controllers, are considered smaller than this frequency. Another simplification that is applied is that the series resistance is considerably smaller then the parallel resistor, which usually holds for the most cases since the actuators are designed in such a way that losses are minimized. Thus, low series resistances and low iron losses (and consequently high parallel resistance) have to be considered. Also, the actuators shown in the experimental chapter exhibit those characteristics and their parallel resistance is usually one or two decades higher than the series resistance. Being the technique with the least simplifications, the full IDIM technique represents a technique that is suitable to most use cases. The simplified IDIM technique in its implementation with the SH stage (SIDIM a) adds other constraints onto the estimation process. In the derivation process, the parallel resistance and the series resistance were neglected, thus restricting the technique onto actuators with low losses and nearly inductive behavior. Thus, the technique cannot be applied in use cases with high current dynamics, since in these conditions the losses become relevant. In the according derivation, this low current dynamic was represented by the approximation $\tau_i \approx \tau_m$, restricting the time constant of the current to the mechanical time constant. In the IDIM technique with a high-pass filter and rectifier-based offset removal (SIDIM b), another constraint is set by applying a high-pass filter with a certain cut-off frequency that band-limits the current signal. The eddy current resistor estimator, instead, applies the same limits to the PWM frequency and the series resistance as the full IDIM technique does, but additionally requires the time difference between consecutive measurements being relatively small. In case this cannot be guaranteed, the error compensation shown in Equation 3.111 needs to be performed.

Dynamic range Based on the approximations that were made, the dynamic work range of the techniques is limited. The IDIM technique has its full dynamic working range, while "full" actually refers to the PWM frequency being the only limiting frequency. Instead, the simplified IDIM techniques are restricted by the current dynamic with its time constant τ_i (variant a) and by the high-pass cut-off frequency (variant b). The eddy current resistor estimator is not limited to a certain frequency.

Influence of measurement errors The measurement error sensitivity analysis reveals that all techniques suffer from an error propagation within the technique. While in the standard IDIM technique, gain and offset errors in the measurements and the integrator circuit lead to combined gain and offset errors in the inductance estimate, which can be easily compensated e.g. by a two point calibration, the simplified IDIM techniques tend to show gain errors for gain error-affected measurements and offset errors for offset-affected measurements. A nonlinear dependence on an offset error occurs when the integrator circuit is affected by an offset, making calibration cumbersome. Thus, focus has to be laid on a robust implementation of the circuit with tight tolerances (see Chapter 4).

Signal-to-noise ratio Compared to the other implementations, the IDIM technique in its full implementation suffers from a qualitatively bad SNR, since the estimation relies on current differences, a mathematical operation that usually increases the noise. Moreover, an appropriate anti-aliasing filter needs to be installed in front of the SH stage if noise should not be sampled and amplified by the integrator. An increase in SNR has the simplified IDIM technique (SIDIM a) with a SH stage-based offset removal, since it does not elaborate current differences but only one dedicated integral measurement. Also here the SH stage may be affected by aliasing, which needs to be prevented. The best SNR performance is obtained using the simplified IDIM variant b, which substitutes the SH-stage based offset removal by applying a high-pass filter and a rectifier. The obtained estimate does not rely on dedicated current triggering and does not make usage of current differences, thus the full capability of the integrator circuit can be used. Finally, the eddy current resistor estimator shows the weakest performance in SNR since it relies on current measurements within an extremely short time period, that are relatively small and further influenced by the transients that occur during the voltage switching. A proper filtering is definitely necessary in this type of estimator.

Application use-cases Summarizing the above made qualifications of the techniques, possible estimation use cases can be derived. The IDIM technique in its full extent requires the most measurements and the most mathematical operations while placing the least assumptions. Thus, this technique allows to evaluate the inductance with the highest possible bandwidth in the field, but with reduced SNR. Therefore, the technique is suited for applications requiring high bandwidth such as fast switching values or linear positioning actuators. Due to their nature, such actuation systems inherently require high-speed ADCs and computationally fast microcontrollers for control and driving purposes and the additional measurement and calculation effort can be compromised. The simplified IDIM techniques, instead, require less measurements and less mathematical operations, with the demerit of reduced bandwidth. Thus, such techniques can be implemented onto low-cost actuation systems, e.g. switching valves or switching actuators, where only the position in rest needs to be evaluated for security purposes. In particular, in those application fields, no or only small microcontrollers are embedded into the device, thus requesting strict constraints on calculations and measurements that the simplified IDIM techniques can offer. Instead, the eddy current estimator only serves as additional measurement. In general, the estimation through the eddy current resistor lacks accuracy and SNR and makes applicability of this approach compared to the inductance-based approach undesirable. Only when the inductance-based estimation lacks uniqueness, such as in the case of certain actuators that show non-bijective behavior, the estimation through the eddy current resistance gathers additional knowledge that allows to resolve the arising ambiguities.

Criteria	**IDIM**	**SIDIM a**	**SIDIM b**	**$\mathbf{R_p}$ estimator**
N measurements (u + i + Q)	1 + 4 + 2	1 + 0 + 1	1 + 0 + 1	1 + 2 + 0
N additions	with R_Σ 17 without R_Σ 5	1	1	1
N multiplications	with R_Σ 13 without R_Σ 3	5	5	1
N divisions	with R_Σ 2 without R_Σ 1	1	1	1
Simplifications	$t_{pwm} \ll \tau_m$ $R_\Sigma \ll R_p$	$t_{pwm} \ll \tau_m$ $\tau_i \approx \tau_m$ $R_p \rightarrow \infty$ $R_\Sigma \rightarrow 0$	$t_{pwm} \ll \tau_m$ $\tau_i \approx \tau_m$ $\tau_{HP} < \tau_m$ $R_p \rightarrow \infty$ $R_\Sigma \rightarrow 0$	$t_{pwm} \ll \tau_m$ $R_\Sigma \ll R_p$ $t_\delta \rightarrow 0$
Dynamic range	full	limited to f_i	limited to f_{HP}	full
Meas. gain error	Gain	Gain	Gain	Gain
Meas. offset error	Gain + offset	Offset	Offset	Offset
Int. gain error	Gain + offset	Gain	Gain	n.a.
Int. offset error	Gain + offset	Nonlinear	Nonlinear	n.a.
SNR	-	+	++	- -
Applications	High bandwidth self-sensing for control of fast switching actuators	quasi-static self-sensing, e.g. end-position detection	quasi-static self-sensing, e.g. end-position detection	Additional measurement when L_Δ is not bijective

Table 3.1: Comparison of the presented self-sensing techniques.

3.5 Position estimation based on model

Based on Sections 3.1 - 3.3, physical parameters can be identified that show a particular position and current dependency:

$$L_\Delta = f(x,i), \tag{3.115}$$

$$R_p = f(x,i). \tag{3.116}$$

In order to reconstruct position information out of these parameters, a suitable model needs to be identified and inverted. The inversion of the incremental inductance L_Δ is only possible in case the function $f(x,i)$ is bijective over the entire current and position range, otherwise the parallel resistance, that is well-known to be bijective, needs to be considered. For modeling the position and current dependency, two common approaches can be followed, namely the physical and the phenomenological approach. While the physical approach tries to identify the model parameters in a way that directly links to physical relations, the phenomenological approach simply tries to fit a certain input-behavior to a certain output-behavior in a mathematical manner. Physical approaches tend to allow a high interpretability while phenomenological approaches are characterized by high accuracy [92].

Physical modeling approaches As shown in Figure 2.8, a magnetic circuit can be modeled that contains the major contributions of the back-iron, the plunger and the air gap in the flux path. This equivalent circuit can now be redrawn based on the assumptions that were made in Chapter 2, namely the negligence of the leakage flux ($\mathcal{R}_l \rightarrow \infty$) and the assumption of a model complexity equal to one ($n_c = 1$), that allows to model the magnetic impedances of the back-iron and plunger as a series connection of a magnetic reluctance and magnetic inductance:

$$\mathcal{Z}_b = \mathcal{R}_b + s\mathcal{L}_b, \tag{3.117}$$

$$\mathcal{Z}_p = \mathcal{R}_p + s\mathcal{L}_p. \tag{3.118}$$

The resulting magnetic equivalent circuit is depicted in Figure 3.10.

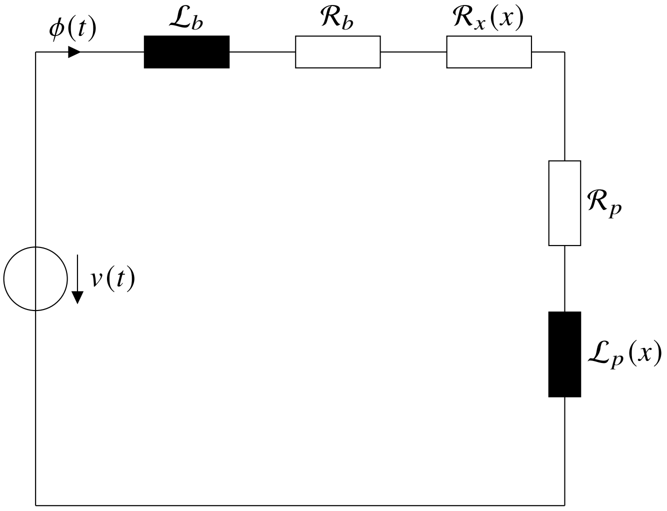

Figure 3.10: Simplified magnetic equivalent circuit used for physical modeling of the position dependence, consisting of magnetic reluctances and inductances of the back-iron, the plunger and the air gap.

The elements of that circuit can be modeled physically by means of the definition of the magnetic inductance

$$\mathcal{L}_b = \sigma_{el,b}\frac{A_b}{l_b}, \tag{3.119}$$

$$\mathcal{L}_p(x) = \sigma_{el,p}\frac{A_p}{l_p + x}, \tag{3.120}$$

with $\sigma_{el,b}$ and $\sigma_{el,p}$ being the conductivity of the back-iron material and of the plunger, respectively, and A_b, A_p, l_b and l_p being the geometrical quantities of the back-iron and the plunger. The electrical conductivity is strongly temperature-dependent and the effect of temperature on this estimation parameters need to be considered during the estimation process. The magnetic reluctances can be modeled by their definition as:

$$\mathcal{R}_b = \frac{l_b}{\mu_{\Delta b}A_b}, \tag{3.121}$$

$$\mathcal{R}_p(x) = \frac{l_p + x}{\mu_{\Delta p}A_p}, \tag{3.122}$$

with $\mu_{\Delta b}$ and $\mu_{\Delta p}$ being the incremental permeabilities of the back-iron and the plunger. Consequently, the air gap can be calculated as:

$$\mathcal{R}_x(x) = \frac{x}{\mu_0 A_x}, \tag{3.123}$$

with A_x being the effective cross-section of the air gap. The parameters L_Δ and R_p are physically linked to those magnetic reluctances and inductances by means of Equation 2.69 as:

$$R_p = \frac{N^2}{\mathcal{L}_b + \mathcal{L}_p(x)}, \tag{3.124}$$

$$L_\Delta = \frac{N^2}{\mathcal{R}_x(x) + \mathcal{R}_p(x) + \mathcal{R}_b}, \tag{3.125}$$

which allows for a physical modeling of the position dependence. Thus a model for the parallel resistance can be obtained as

$$R_p(x) = \frac{N^2}{\sigma_{el,b}\frac{A_b}{l_b} + \sigma_{el,p}\frac{A_p}{l_p+x}}. \tag{3.126}$$

In the case of the incremental inductance L_Δ, the modeling can get cumbersome because of the magnetic permeability. In particular, the magnetic permeability underlies saturation and hysteretic effects that cause current dependency with memory. Furthermore, the parameters of the magnetic permeability are slightly temperature-dependent. Most materials show a significant saturation over the current, thus a function $\mu(i)$ needs to be considered for modeling:

$$L_\Delta(x,i) = \frac{N^2}{\frac{x}{\mu_0 A_x} + \frac{l_p+x}{\mu_{\Delta p}(i)A_x} + \frac{l_b}{\mu_{\Delta b}(i)A_b}}. \tag{3.127}$$

There exist various approaches in literature for modeling the saturation curve by means of e.g. hyperbolic arctangent or hyperbolic cosine functions [92]. For more precise modeling, also the hysteretic nature of the material needs to be considered. Treating materials with hysteresis is covered thoroughly in Section 3.6. On the other hand, when materials with strong permeability ($\mu_\Delta \rightarrow \infty$) are used, the current dependency can be neglected, allowing a simplified identification and modeling procedure:

$$L_\Delta(x) = \frac{N^2 A_x \mu_0}{x}. \tag{3.128}$$

The modeling by means of physical approaches consequently allows a white-box/grey-box identification approach where the parameters to be identified rely on physical quantities such as length, cross sections and electrical and magnetic properties. While this approach allows good interpretation capability, the accuracy can be reduced e.g. due to model uncertainties and unmodeled physical effects such as parasitic flux paths.

Phenomenological modeling approaches Phenomenological approaches allow a modeling with high accuracy and medium calculation and identification effort by means of mathematical interpolators. Based on an offline-identified training data-set, the models can be tuned and fitted until a certain accuracy is achieved.

First works [42, 44] in the field made usage of look-up tables with linear interpolation. While being easy to implement, such approaches usually lead to considerable memory usage when high accuracy is desired. Thus, works such as [93] apply polynomial curve fitting on the parameters in order to extract the position information:

$$f(x, i) = \Sigma_{k=0}^{n_x} \Sigma_{l=0}^{n_i} C_{kl} \cdot x^k \cdot i^l, \tag{3.129}$$

where n_x and n_i are the model orders for the position and current dependency. Weighting of the different polynomials is obtained by the coefficients C_{kl}. Instead of obtaining a model of the parameter and then inverting it for position estimation, a pseudo-inverse model can be directly fitted:

$$x = \Sigma_{k=0}^{n_p} \Sigma_{l=0}^{n_i} C_{kl} \cdot p^k \cdot i^l, \tag{3.130}$$

where p is a parameter that is either the incremental inductance or the parallel resistance and n_p is a model order for that particular parameter.

In the more recent years, sophisticated works such as [94] apply artificial neural networks (ANN) such as multilayer perceptrons (MLPs) in order to model the actuator characteristic and use it for position estimation. MLPs have proven to provide good inter- and extrapolation capability with high accuracy [95]. For instance, Figure 3.11 shows a MLP for position estimation based on the incremental inductance. The input layer processes the inputs in form of the incremental inductance, the parallel resistance and the actual current. The output layer provides the estimate of the actuator position. The layer between is called hidden layer and combines the information of the layers before by means of a linear combination of its inputs based on certain weights Θ and an activation function. For the hidden neurons, usually a sigmoid or arctangent function is used while the output layer is based on linear functions as activation functions [95, 96].

During the training process of MLPs, particular focus has to be laid on the training data in order to avoid overfitting. That can be achieved by dividing the identification data into a training, validation and testing set. While this as well as the training methods would clearly expand the scope of this thesis, the interested reader is guided to [95].

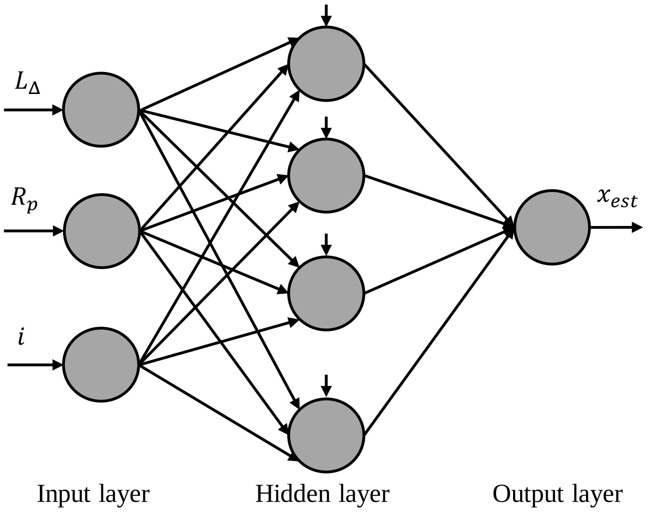

Figure 3.11: Structure of a MLP neural network used for position estimation. Each neuron of each layer is connected to the neurons in the next layer with a certain weight factor.

3.6 Compensation of hysteretic phenomena

In Section 3.5, physical and phenomenological models were presented that allow using the identified incremental inductance for position estimation. Those models are capable to model the properties of magnetic materials such as eddy currents and saturation effects. Nevertheless, such materials also exhibit magnetic hysteresis, that adds a memory-dependent characteristic onto the nonlinear characteristic that is usually covered successfully by those models. Mathematically, hysteresis brings a memory element into the model, that can be described as:

$$\mu_\Delta = f(i, \mu_{\Delta 0}), \tag{3.131}$$

where $\mu_{\Delta 0}$ is the incremental permeability at the initial time. Based on Equation 3.127, this hysteretic dependency can be added onto the model:

$$L_\Delta(x, i, L_{\Delta 0}) = \frac{N^2}{\frac{x}{\mu_0 A_x} + \frac{l_p + x}{\mu_{\Delta p}(i, \mu_{\Delta p0}) A_x} + \frac{l_b}{\mu_{\Delta b}(i, \mu_{\Delta b0}) A_b}}. \tag{3.132}$$

In literature, various models for the identification and compensation of hysteretic phenomena exist, either based on physical or phenomenological considerations. The work [97] gives a through overview over model classes and well-known models. Nevertheless, for compensation of the hysteresis in the incremental inductance, first the coupling between the air gap reluctance and the back-iron and plunger reluctance, that is present in the equation, needs to be solved. Only then a hysteresis model can be applied.

Separation principle Decoupling between the air gap and the plunger as well as back-iron reluctance can be obtained by applying a separation principle [59]. Doing so allows to decouple the position dependency of L_Δ from the current dependency of L_Δ that causes hysteresis. The necessary assumption for this is that the air gap is considerably smaller than the length of the plunger: $x \ll l_p$. In most actuators this consideration is fulfilled since the air gap is minimized for the highest force. By applying this simplification, the equation can be obtained to:

$$L_\Delta(x, i, L_{\Delta 0}) = \frac{N^2}{\frac{x}{\mu_0 A_x} + \frac{l_p}{\mu_{\Delta p}(i, \mu_{\Delta p 0}) A_x} + \frac{l_b}{\mu_{\Delta b}(i, \mu_{\Delta b 0}) A_b}}, \tag{3.133}$$

whose components can be summarized as:

$$L_\Delta(x, i, L_{\Delta 0}) = \frac{N^2}{\mathcal{R}_x(x) + \mathcal{R}_{\Delta Fe}(i, \mathcal{R}_{\Delta Fe 0})}, \tag{3.134}$$

with $\mathcal{R}_{\Delta Fe}$ being the hysteretic iron reluctance summarizing all reluctances in the actuator that exhibit a magnetic hysteresis, namely the back-iron and the plunger. This magnetic circuit that stems from the equation with separation is depicted in Figure 3.12.

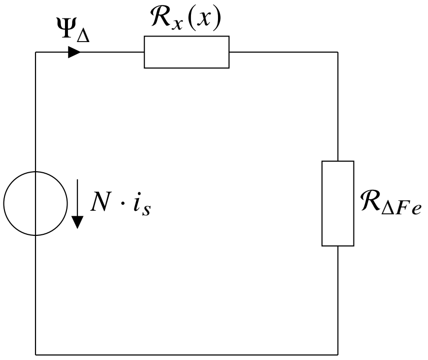

Figure 3.12: Reduced magnetic circuit for self-sensing with hysteresis compensation, adopted from [71].

Thus, the total magnetic reluctance that is present in the actuator is the sum of the air gap and iron reluctance:

$$\mathcal{R}_{\Delta tot} = \mathcal{R}_x + \mathcal{R}_{\Delta Fe}, \tag{3.135}$$

while the air gap reluctance is represented by a function (either based on physical or phenomenological considerations) that is zero when the air gap is closed:

$$\mathcal{R}_x = f(x) \quad with \quad \mathcal{R}_x(x=0) = 0. \tag{3.136}$$

Thus, it can be concluded that the total reluctance resembles the iron reluctance in case the air gap equals zero:

$$\mathcal{R}_{\Delta tot}(i, x=0) = \mathcal{R}_{\Delta Fe}. \tag{3.137}$$

The following compensation strategy is based on the comparison between the total reluctance under closed air gap $\mathcal{R}_{\Delta tot}(i, x=0)$, that can be modeled and estimated by means of an online model of the iron core reluctance $\hat{\mathcal{R}}_{\Delta Fe}(i, x=0)$, and the actual total reluctance at a particular air gap $\mathcal{R}_{\Delta tot}(i)$ that is obtained by measurement. The difference between these quantities is dependent on the air gap reluctance and consequently on the position. This difference can be evaluated for position estimation by inverting the function $f(x)$.

Considering Equation 3.136, a simple identification of the iron reluctance is possible when the actuator position is blocked to a zero air gap, since no position dependency is present. With this identification, a hysteresis model can be tuned that allows to estimate the value of the iron core reluctance:

$$\begin{aligned} \hat{\mathcal{R}}_{\Delta Fe}(i, x=0) &\approx \frac{i}{\hat{\psi}_\Delta(i, x=0)} \\ &= \frac{i}{M(i)}, \end{aligned} \tag{3.138}$$

where M indicates the trained hysteresis model. It estimates the incremental flux $\hat{\psi}_\Delta$ that describes the flux that is present inside a PWM-caused minor loop on the BH-curve. In the next paragraph this parameter will be further described and an estimation procedure will be given. On the other side, the total reluctance during operation at varying air gap can be calculated as

$$\mathcal{R}_{\Delta tot}(i, x) = \frac{i}{\psi_\Delta}. \tag{3.139}$$

Knowing both the estimated iron core reluctance and the total reluctance, the air gap reluctance can be calculated:

$$\hat{\mathcal{R}}_x(x) = \mathcal{R}_{\Delta tot} - \hat{\mathcal{R}}_{\Delta Fe}, \tag{3.140}$$

and inverted for position information extraction. The algorithm in total can be consequently described as:

$$\begin{aligned} x_{est} &= f^{-1}(\hat{\mathcal{R}}_x) \\ &= f^{-1}\left(\mathcal{R}_{\Delta tot} - \hat{\mathcal{R}}_{\Delta Fe}(i, x = 0)\right) \\ &= f^{-1}\left(\frac{i}{\psi_\Delta} - \frac{i}{M(i, x = 0)}\right). \end{aligned} \tag{3.141}$$

The function $f()$ then allows the estimation of the position by exploiting the position dependency of the air gap reluctance. The function must be strictly monotonous in order to be invertible. Theoretically, only a position dependency is present, but practically, due to unmodeled parasitic flux paths and uncertainties in the hysteresis model, also a current dependency is present. Thus, in order to increase the accuracy of the position estimator, a function of the form $f(x, i)$ is recommended that takes into consideration the dependency on both position and current.

Hysteresis model In the previous paragraph, an estimation approach for the air gap reluctance was shown that allows decoupling the hysteretic core reluctance from the air gap and thus allows compensating for hysteretic phenomena. For calculating the iron core reluctance, the incremental flux ψ_Δ needs to be known, that represents the flux inside a minor loop, as depicted in Figure 2.4. A suitable hysteresis model then estimates this quantity under the assumption that the air gap is vanished. Such type of hysteresis model will be used here for the identification and estimation of the incremental flux and the incremental reluctance of the core.

In practice, two challenges have to be faced: first, the incremental flux ψ_Δ is not directly available as an estimate. The techniques discussed in Sections 3.1 and 3.2 directly estimate the incremental inductance L_Δ of the actuator. This parameter is directly obtainable out of the current ripple of the actuator by means of the IDIM technique. Secondly, the incremental inductance shows a butterfly hysteresis, as visible in Figure 2.5. Such a butterfly hysteresis cannot be modeled by means of a standard hysteresis model, independently of the model nature, because they try to identify classical B-H-curves like characteristics. Thus, the butterfly hysteresis behavior of the incremental inductance first needs to be transformed into a classical BH-curve hysteretic characteristic. This procedure will be carried out by means of an integration approach, that directly delivers the incremental flux as output, whose hysteresis is of a BH-nature.

In the following, only the fundamental current will be considered that represents the operation point (H_0, B_0) respectively (i, ψ_0) on the hysteresis curve. Under consideration of Equation 2.18, an integral can be defined that allows estimating the incremental flux under knowledge of the incremental inductance, that is obtained by the IDIM technique:

$$\psi_{\Delta} = \int L_{\Delta} \Delta i. \tag{3.142}$$

Continuously evaluating the integral allows to estimate the incremental flux during operation of the actuator. The incremental flux has a purely BH-curve like hysteretic behavior and allows the adaptation of standard physical and phenomenological hysteresis models onto this problem. Nevertheless, this approach has several issues related to the implementation. These are:

- Initialization: in order to successfully track the actual magnetic working point, the integral of Equation 3.142 needs to be correctly initialized. Since magnetic materials exhibit remanence effects, first the actuator needs to be fully demagnetized, so that the actuator material is in its origin point and the virgin curve is followed once a current is applied. Demagnetization can be achieved by applying a demagnetization signals that first drives the actuator into full magnetic saturation and then applies a sine signal with decreasing amplitude until the origin point is reached. Such an initialization procedure is anyways needed for the underlying hysteresis model $M(i)$.
- Numerical implementation of the integral: Equation 3.142 represents a time-continuous integral that needs to be implemented on a time-discrete system. Consequently, a numerical integration method needs to be implemented. As a good trade-off between accuracy and computational effort, the trapezoidal rule is considered [98]:

  $$\psi_{\Delta j+1} = \psi_{\Delta j} + \frac{i_{j+1} - i_j}{2} \left(L_{\Delta j+1} + L_{\Delta j} \right), \tag{3.143}$$

  where j stands for the actual sample of the current and the incremental inductance.
- Integrator drifting: a practical implementation of an integrator suffers from continuous drifting due to small measurements errors as well as numerical precision limitation. Since those errors sum up continuously, drifting and consequently saturation of the integrator is a major problem for the estimation algorithm. In order to prevent this issue, the integrator needs to be corrected and actively compensated at well known points on the BH- respectively the ψ-i-curve. Because of the ambiguities that arise from hysteresis, this has to be done at unique working points, such as the saturation that occurs at maximum positive and negative currents. Applying the drift compensation at those two saturation points inherently limits the drifting. Further increase in accuracy can be achieved by forcing the integral value to a fixed value at the origin, where the concrete operation point is known when the moving

direction is known. Thus, under consideration of the saturation points and the origin, the drift can be compensated at every quarter cycle of the major BH-curve.

By applying the integration approach, an estimate of the incremental flux can be obtained that serves as training data and output of the hysteresis model. For the presented work, the Modified Prandtl-Ishlinskii (MPI) model is used due to good accuracy and its low computational effort. The model itself is easy to identify and to optimize since it is based on a quadratic problem [99]. Furthermore, the model can be inverted algebraically, a property that separates this technique from other existing models that only allow numerical inversion [99]. The MPI model consists of simple operators that are superimposed. Figure 3.13a shows the play operator that is used to model memory while Figure 3.13b shows the superposition operator that allows to model nonlinearities. In those figures, the operators are shown with a generic input x and a generic output y.

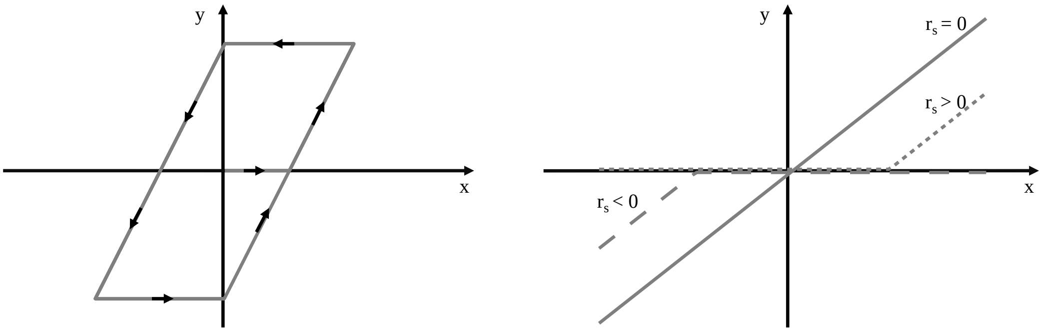

(a) Play operator with moving directions, adopted from [71, 99]. **(b)** Superposition operator, adopted from [71, 99].

Figure 3.13: Characteristics of the Play and Superposition operators, that model systems with memory and nonlinearities, respectively.

The play operator can be mathematically described by:

$$H(x, y, r_H) = max\left(x - r_H, min\left(x + r_H, y\right)\right), \tag{3.144}$$

with r_H being the threshold that describes the width of the hysteresis [99]. The superposition operator, instead, can be modeled by

$$S(x(t), r_S) = \begin{cases} max\left(x(t) - r_S, 0\right) & \text{for} \quad r_S > 0 \\ x(t) & \text{for} \quad r_S = 0 \\ min\left(x(t) - r_S, 0\right) & \text{for} \quad r_S < 0 \end{cases}, \tag{3.145}$$

with r_S being a threshold that describes the width of the one-sided dead-zone [99]. By linear superposition of several operators and weighting with certain factors, a hysteresis in the form of a BH-curve can be modeled successfully [99]. Such a model based on superposition is formulated as [100]:

$$M\left[i\right](t) = \mathbf{w_s}^T \mathbf{S_{r_s}} \left[\mathbf{w_h}^T \mathbf{H_{r_H}} \left[i, \mathbf{z_{H0}}\right]\right](t), \tag{3.146}$$

with $\mathbf{w_H}$ and $\mathbf{w_S}$ being the weight vectors of the play and superposition operators as well as $\mathbf{H_{r_H}}$ and $\mathbf{S_{r_S}}$ being the vector containing the play and superposition operators. The vector $\mathbf{z_{H_0}}$ contains the initial values of the model. This model can be algebraically inverted:

$$M^{-1}\left[\psi_\Delta\right](t) = \mathbf{w_H}'^T \mathbf{H_{r_H}} \left[\mathbf{w_S}'^{\mathbf{T}} \mathbf{S_{r_s}} \left[\psi_\Delta, \mathbf{z}'_{\mathbf{H0}}\right]\right](t), \tag{3.147}$$

where the inverted weights are denoted with '. More about the model, its identification and its inversion is given in the work [99]. Within the previous paragraphs, a hysteresis compensation approach was shown. Figure 3.14 shows the complete algorithm in detail. First, the current of the actuator is measured. This quantity serves as input for the MPI model $M(i)$, that provides an estimate of the incremental flux that is used for the calculation of the core reluctance. In parallel, the IDIM technique estimates the incremental inductance, that together with the measured current, is integrated in order to obtain an estimate of the incremental flux that is used to estimate the total magnetic reluctance. The difference between core reluctance and total reluctance yields the air gap reluctance that can be inverted for position estimation.

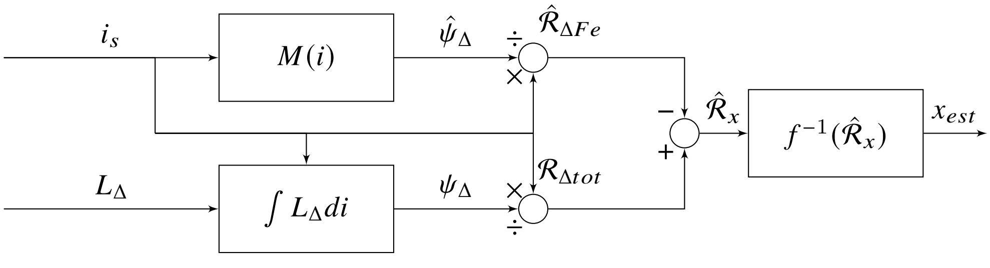

Figure 3.14: Used hysteresis compensation, adopted from [71].

4 Experimental results

In this section, experimental results of the shown self-sensing algorithms will be presented and compared to high precision measurement devices. Before showing the experiments, a short description of the implementation details of the integrator circuit is shown due to its importance on the self-sensing approach. Then, a short overview on the experimental test-setup is given. Afterwards, the IDIM techniques are compared in terms of SNR to a standard oversampling technique in order to prove the computational lightweightness of the approach while maintaining an acceptable SNR. Finally, position estimation results are shown on a switching actuator, on an actuator with hysteresis compensation and on a switching actuator with non-monotonous characteristic.

4.1 Implementation of the integrator circuit

As shown in Chapter 3, the integrator circuit is the main part of the presented self-sensing techniques. Thus, implementation limitations and issues in that circuit can have a significant impact on the performance of the self-sensing algorithm. Therefore, the implementation of the integrator circuit will be shown in detail in this section.

As shown in Figure 3.3, the integrator resembles an inverting integrator stage realized with an operational amplifier. Since the integrator is inverting, a negative supply rail is needed in order to cover the complete signal range [88]. Providing a negative supply rail is usually linked with increased component effort and, consequently, higher costs. A suitable solution to this is the usage of fully differential operational amplifiers that are single-voltage-supplied and provide a common mode voltage for the signal [101]. Such operational amplifiers are additionally more robust against noise and consequently are better suited for applications requiring high resolution and accuracy [101]. Figure 4.1 shows the implementation of an inverting integrator in fully differential analog technology. In particular, two feedback paths are present and the components in those parts must be equal: $C_1 = C_2 = C_{int}$ and $R_1 = R_2 = R_{int}$. Thus, the output voltage can be described as:

$$u_{out}(t) = -\frac{1}{R_{int}C_{int}} \int_{r(t)\neq 1} u_{in}(t)dt. \tag{4.1}$$

In this case, the voltage u_{out} is measured differentially and can have a negative value since both differential signals are based on a positive bias voltage. In Chapter 3, an error analysis was shown that revealed the sensitivity of the method towards gain errors. In particular, tolerances in the passive components, namely the integration resistor and capacitance, can lead to such errors during self-sensing. Thus, it is desirable to decrease the tolerances in those components, consequently leading to higher costs. A solution to this is offered by the so-called Switched Capacitor technology (SC) that is used in integrated analog circuits in order to decrease cost while decreasing tolerances [102, 103].

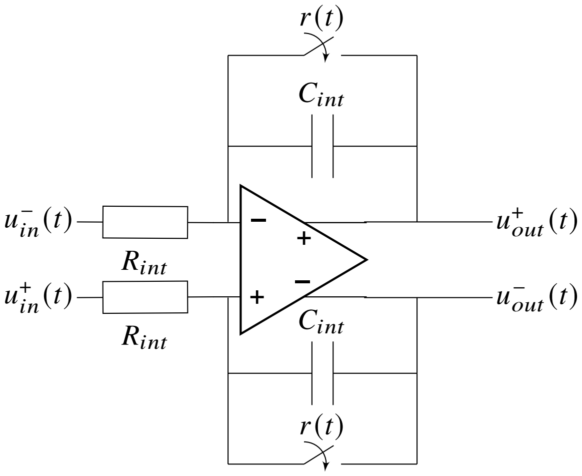

Figure 4.1: Fully differential analog integrator with reset capability, adopted from [104].

The SC technology is based on an observation from James Maxwell that a capacitor that is switched at sufficiently high frequency behaves like a resistive component [102]. This can be used in a technological manner because in MOS (Metaloxide Semiconductor) processes, capacitances can be easily realized. When the switching frequency of the capacitor is considered significantly higher then the bandwidth of the signal: $f_c \gg f_{sig}$, it can be assumed that the current flowing through the capacitor is almost constant and the switched capacitor behaves like a resistor [103]:

$$R_{eq} = \frac{T_c}{C_R}, \tag{4.2}$$

with R_{eq} being the equivalent resistor, $T_c = \frac{1}{f_c}$ being the time interval of switching and C_R being the switched capacitor. Thus, resistances in analog circuitries can be replaced by capacitances. This has several merits compared to the classical implementation: First, capacitors can be simply realized with high tolerances in MOS processes [103]. Secondly, the ratio of capacitances is producible with tolerances less than 0.1%, because those capacitor arrays can be physically matched [103]. And finally, since resistances with large values can be avoided, also large time constants in integrators and filters can be realized, which is especially useful for the implementation of the IDIM technique [103]. The implementation of an inverting fully-differential integrator circuit in SC technology is shown in Figure 4.2. The resistors are replaced by switched capacitors with two complementary clocks Φ_1 and Φ_2, that are non-overlapping and switched at a frequency f_c. During phase Φ_1, the voltage at the input is sampled on the capacitor while in phase Φ_2, the charge on C_{R1} is transferred to C_1, where it is summed upon the already existing charge, which resembles an integration [103]. The equation of the integrator circuit in SC technology yields to [103]:

$$u_{out} = f_C \frac{C_{R1}}{C_1} \Sigma_{r(t)\neq 1} u_{in}(t)\Delta t, \tag{4.3}$$

with $f_C \frac{C_{R1}}{C_1}$ being the integration constant that is now based on a ratio of capacitors. The time of each integration step is denoted as Δt. Another positive side-effect is that the reset switches, that are needed for the reset of the integrator circuit, are already available in SC technology.

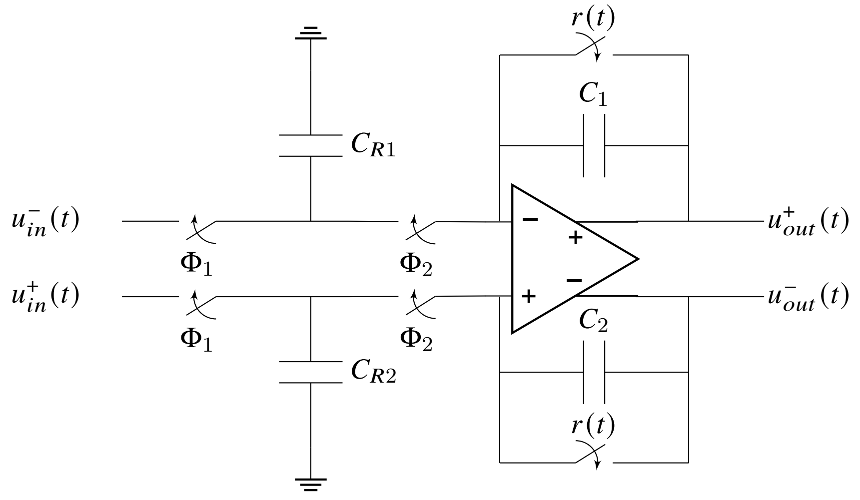

Figure 4.2: Fully differential analog integrator with reset capability realized in SC technology, adopted from [104].

A platform that was used during the experimental tests was based on rapid prototyping of those SC circuits by means of a Field Programmable Analog Array (FPAA) that allows to fully configure certain circuit typologies by means of programming. In particular, the FPAA AN231 from the company Anadigm was used [105]. This FPAA features seven freely programmable analog cells consisting of operational amplifiers, comparators and programmable capacitor arrays [105]. The software library contains standard operational amplifier circuits with programmable gains and cut-off frequencies and, consequently, allows to implement the IDIM technique in all of its implementations.

Because the FPAA is merely a rapid prototyping solution with limited bandwidth, a fully integrated circuit covering the resettable integrator circuit was designed and realized in cooperation with the Institute for Microelectronic Circuits and Systems (IMS) in Duisburg, Germany. The resulting application-specified integrated circuit (ASIC) is shown in Figure 4.3. For more information, the interested reader is guided to [104]. The ASIC contains the circuitries that are necessary for the IDIM technique in its full and simplified variants. The gains and cut-off frequency can be tuned through programmable capacitor arrays [104]. With its dimensions of 2.5x4 mm^2, its operating voltage of 3.3 V and a switching frequency of f_c =213 MHz [104], the ASIC is well suited for the usage of in integrated electronics.

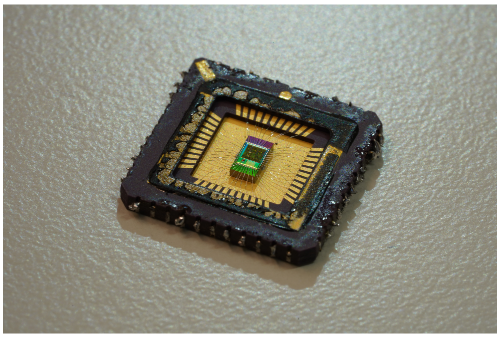

Figure 4.3: ASIC implementing the SC integrator for the IDIM technique.

4.2 Test-bench used for experiments

Figure 4.4 shows the used test-bench in a schematic way while Figure 4.7 shows the actual realization of the test-bench that is used for experimental identification and measurements. It consists of a high-precision positioning table that serves as counter-actuator for the solenoid under test, the solenoid itself, a Printed Circuit Board (PCB) as well as a measurement computer. The positioning table is the model M403.DG from Physic Instruments [106] and allows the precise control of the position of the rod within a range of 100 mm with a minimum step size of 200 nm. It also involves a high precision magnetic incremental encoder with 200 nm resolution that serves as reference for the measurements. The positioning table is current- and position controlled and holds its actual position until a blocking force of 50 N is reached [106]. Thus, it can block the actuator plunger at a desired reference position even when a force-generating current onto the actuator is applied. The PCB has been developed at the Laboratory of Actuation Technology (LAT) and it contains three half-bridges operating at 24 V with currents up to 10 A. In this use case, two half-bridges are connected to a full H-Bridge. The current is measured by means of the current shunt amplifier AD8418 from Analog Device [107], that has a gain of 20 and a bandwidth of 250 kHz [107]. The shunt is placed in series with the actuator, so that a direct measurement of i_s is possible. The PCB additionally contains the microcontroller unit STM32H743 from STMicroelectronics, that is a 32 bit microprocessor with 16-bit AD converters and double precision FPU (floating point unit). The microcontroller is overdimensioned in comparison to usual industrial set-ups in order to allow the measurement and evaluation of all techniques and quantities. The PCB also involves a swappable pinheader that allows to mount the FPAA or ASIC circuitry for the implementation of the IDIM techniques. Finally, a USB connection to a computer allows the transmission of all measurement data. In all set-ups, a current controller was tuned accordingly with the modulus optimum criteria in order to supply the actuator with a fixed current even under varying supply voltages, inducted voltages or increasing resistance due to self-heating.

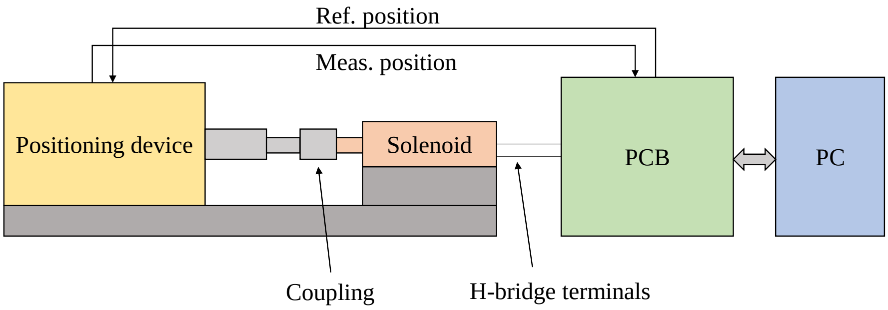

Figure 4.4: Schematic of the used experimental test-bench.

4.3 Comparison of the techniques in terms of noise

As discussed in the state-of-the-art, some techniques make usage of oversampling (OS) in order to estimate the actual actuator inductance. While this significantly increases the SNR, a certain amount of computational power needs to be available. The IDIM technique aims at avoiding oversampling while preserving the SNR. Thus, a comparison in terms of noise power is useful to understand the potential of the techniques as well as at which number of samples the IDIM technique outperforms the oversampling approaches. In general, oversampling approaches take a certain number of samples per each voltage and current signal at dedicated time instants, so that the vectors

$$\mathbf{t} = \left[t_s^+ ... t_e^+ t_s^- ... t_e^-\right], \tag{4.4}$$

$$\mathbf{u} = \left[u(t_s^+) u(t_e^+) ... u(t_s^-) ... u(t_e^-)\right], \tag{4.5}$$

$$\mathbf{i} = \left[i_s(t_s^+) ... i_s(t_e^+) i_s(t_s^-) ... i_s(t_e^-)\right], \tag{4.6}$$

are available in order to perform regression algorithms and curve fitting methods. It is important to wait a certain time t_r after the transients in order to ensure that no nonlinear inverter effects, glitches in the measurements and decaying eddy currents are sampled that otherwise would lead to a biased identification of the inductance [51, 53]. For sake of brevity, those techniques will not be discussed in detail here. For the experiments, the technique from the work [53] is used, that evaluates the data set by means of a LMS algorithm in order to estimate the series resistance and the inductance. In particular, the work used 1600 samples per PWM period at a PWM frequency of 500 Hz in order to perform the estimation.

In the next paragraph, the IDIM technique will be compared to the estimation via those techniques in terms of noise power, that allows for a statement about the SNR of those techniques. Due to the absence of an 'exact' inductance value, the deviation is calculated based on the mean value of the identified inductance $\bar{L}_\Delta$:

$$n(j) = L_\Delta(j) - \bar{L}_\Delta, \tag{4.7}$$

where $n(j)$ stands for the noise of the actual value. The noise power is defined as [108]:

$$P_n = \frac{1}{L}\Sigma_{j=1}^{L} n(j)^2, \tag{4.8}$$

where L is the length of the data vector. It can be seen that the noise power resembles the definition of the signal variance σ^2. The noise power is preferred since its actual value is independent on the amplitude of the signal, unlike the definition of the signal-to-noise ratio, which is cumbersome to evaluate when the amplitude of the signal varies or is close to zero.

Figures 4.5 as well as 4.6 show the estimated incremental inductance for two working points of the actuator MSM GTC-A 40, which is described in detail in Section 4.4. In order to simplify the evaluation of the noise power, two working points of the actuator have been chosen that are the extreme working points. Figure 4.5 shows the actuator when it is opened, meaning that the air gap is maximum (x = 8 mm) and when it is without driving current ($i_d = 0$ A). In such a working point, the inductance shows no saturation and consequently has a large value. Figure 4.6 shows a working point in which the actuator is closed, meaning that the air gap is minimal ($x = 0$ mm) and the

Technique	$\mathbf{P_n}$ in dB (opened)	$\mathbf{P_n}$ in dB (closed)
IDIM	-55.0	-57.1
SIDIM	-74.8	-72.3
OS 50	-44.4	-53.6
OS 100	-48.6	-57.2
OS 250	-51.2	-59.2
OS 500	-54.3	-61.8
OS 1000	-56.1	-62.7

Table 4.1: Comparison of the noise power P_n for different techniques with different number of samples when the actuator is opened and without driving current and when the actuator is closed and driven with its nominal current.

actuator is driven with its nominal current ($i_d = 0.35$ A). In particular, the inductance is driven deeply into saturation at this working point, thus leading to a minimal inductance value. The estimated inductance is obtained by the IDIM technique, the simplified IDIM technique and the previously shown oversampling approach with different number of samples ranging from 50 to 1000 samples per PWM period at a PWM frequency of 500 Hz. Oversampling techniques with different number of samples are not shown, since in the case of less than 50 samples per PWM period, the algorithm fails to converge and for values larger than 1000 samples, the computational power of the microcontroller is exceeded. For both working points, the noise power values have been obtained using Equation 4.8 for all the mentioned techniques. The values of the different noise powers are summarized in Table 4.1 for the opened actuator and for the closed actuator.

For the working point with zero mean current and opened plunger position, the simplified IDIM technique achieves the best performance with -74.8 dB, followed by the OS approach with 1000 samples. Then, the IDIM technique in its full definition follows in the ranking with -55 dB, leaving the OS approaches with less than 1000 samples behind. The worst performance is achieved by the OS approach with 50 samples per PWM period with a noise power of -44.4 dB. In the experiments, all techniques show identification biases. The OS approaches especially suffer from biases in case the decaying eddy current cusps are taken into the consideration. Maximizing the waiting time t_r decreases the biases significantly, leading to the same mean value of all OS approaches. Instead, the IDIM techniques show a larger biases, that results from the limitations that have been made during derivation of those technique, especially in the case of the SIDIM technique. For conclusion, it can be said, that for the particular working point, the IDIM technique outperforms the OS approaches with less than 500 samples, while the SIDIM technique outperforms all approaches.

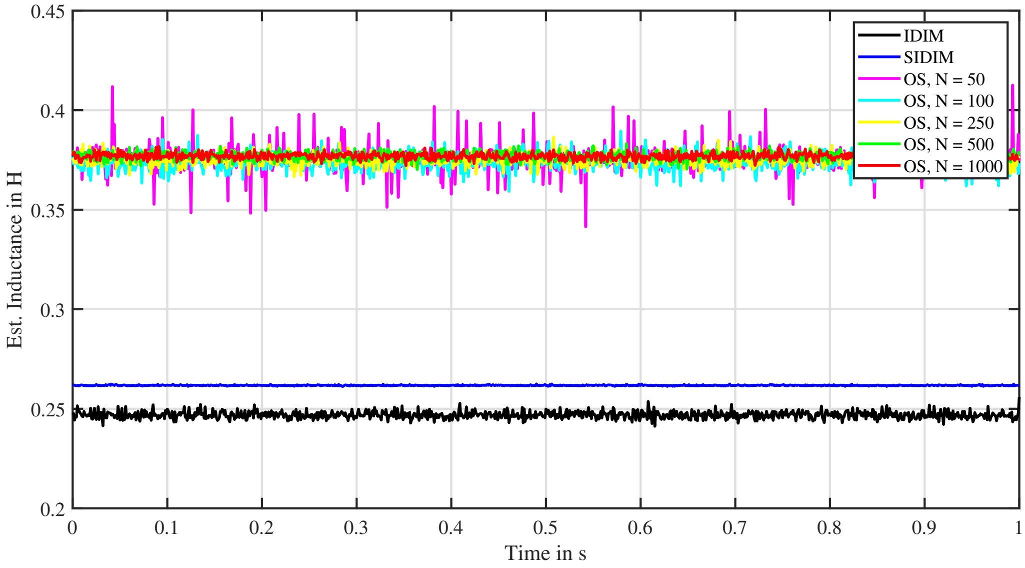

Figure 4.5: Estimated inductance value when the actuator is opened and without driving current. The value is shown for different estimation techniques and different number of samples.

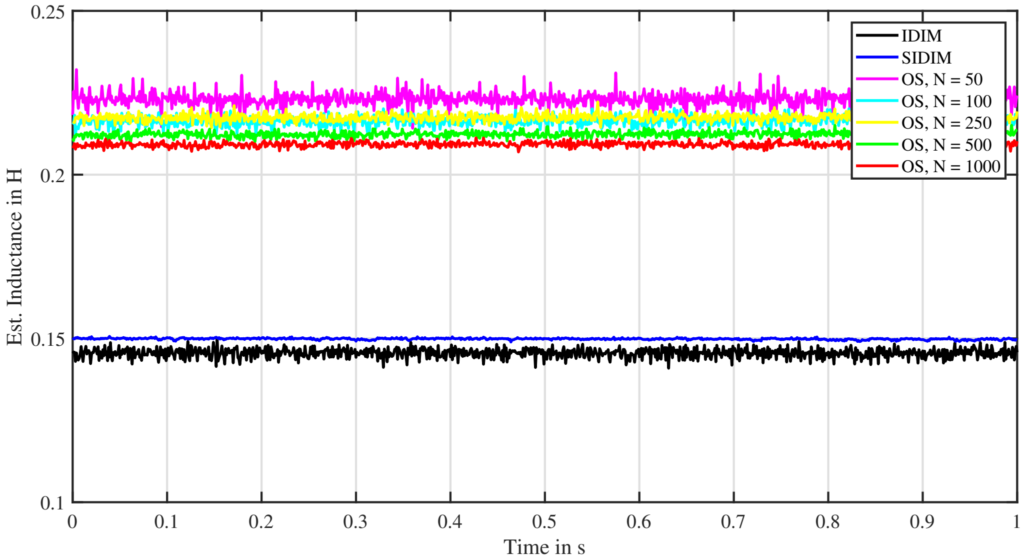

Figure 4.6: Estimated inductance value when the actuator is closed and driven with its nominal driving current. The value is shown for different estimation techniques and different number of samples.

The same considerations have been also conducted for the operating point involving the nominal current of the actuator, which leads to the movement of the plunger into the closed position. Also there, the SIDIM technique shows the best performance with −72.3 dB, followed by the OS approaches with 1000, 500 and 250 samples per PWM period. The IDIM technique in its full definition and the OS approach with 100 samples nearly shows the same noise power with −57.1 dB and −57.2 dB, respectively. At the last position is the OS approach with 50 samples per PWM period. Also here the approaches show identification biases like in the experiment with the opened working point. It can be said that in this experiment, the SIDIM technique outperforms all approaches while the IDIM technique shows the performance of an OS approach with 100 samples.

It can be concluded, that the SIDIM technique provides the best result for both extreme working points, showing a noise power that is smaller than the OS approach with 1000 samples per PWM period. The IDIM technique shows comparable results with an OS 100 approach for the current-driven actuator while being slightly more noise-free than an OS 500 approach for the opened actuator. The difference in the estimation performance for opened and closed actuator mainly lies in the resulting current ripple. While an opened actuator is not affected by saturation and consequently has an higher inductance, the closed actuator is driven in its magnetic saturation leading to a strong decrease in inductance. As shown by Equation 2.93, the current ripple is dependent on the inverse of the inductance, and consequently, a smaller inductance causes bigger current ripples, which can be more easily sensed. Finally, it can be said, that especially the SIDIM technique is able to outperform OS approaches, while the IDIM technique also shows good results for higher inductances.

4.4 Position estimation on switching actuators

In the following, experimental results on position estimation algorithms for electromagnetic actuators will be shown. In particular, three cases will be discussed thoroughly. First, the end position detection on an industrial solenoid actuator from Magnet-Schultz-Memmingen by means of the IDIM and SIDIM techniques. In this case, only two working points will be evaluated: when the actuator is without driving current and when the actuator is driven with its nominal current. In such switching actuators, the information if the actuator has opened or closed in the right way is important, and in case complete closure/opening is not fulfilled, the rest position is of interest. The second case involves the same switching actuator, but instead of having two dedicated working points, a linear operation of the actuator is studied. In this case, the hysteretic behavior of the actuator has to be fully compensated for precise position estimation. In particular, the complete current range is studied and the self-sensed inductance is compensated with the previously presented hysteresis model. The last case involves an industrial switching solenoid from Red Magnetics that exhibits a remarkable ambiguity in position estimation due to its strong magnetic saturation behavior. In this case, the eddy current estimator is experimentally verified and a position fusion algorithm by means of a Multilayer Perceptron neural network is proposed and verified. For all experiments, a characteristic of the actuator is identified and analyzed before applying the above mentioned self-sensing algorithms.

4.4.1 End position detection with self-sensing

In this experiment, the industrial switching actuator GTC-A-40 from Magnet Schultz Memmingen [109] is used, as depicted in Figure 4.7. Its full characteristics in terms of actuator parameters and IDIM settings are shown in Table 4.2. The shown experimental results have been previously published by the author in [65]. Figure 4.8 shows the current ripple of that actuator when a PWM with a frequency of 500 Hz is applied. Furthermore, the reset signal $r(t)$ is measured for the IDIM and SIDIM techniques. The reset signal is chosen in such a way that the cusps and measurement glitches in the current ripple are avoided. The last plot shows the measurement of the output of the integrator circuit $Q(t)$ that is obtained by the IDIM techniques.

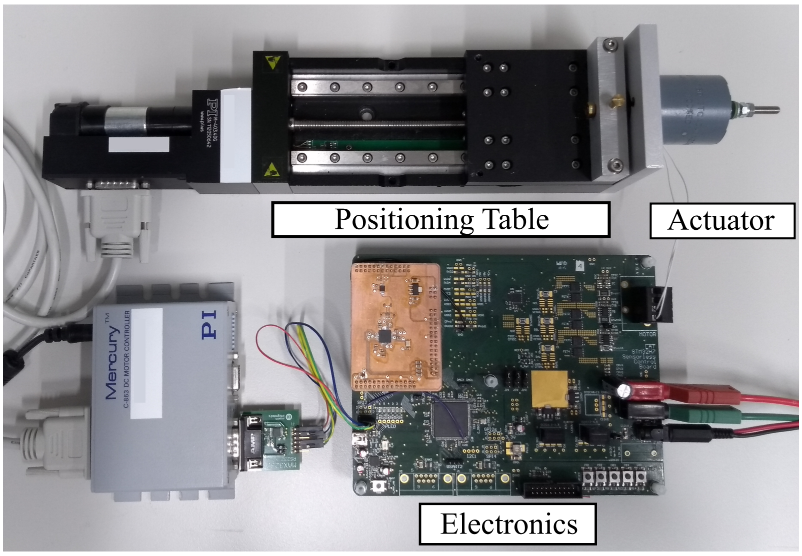

Figure 4.7: Actuator GTC-A-40 from Magnet-Schultz-Memmingen used for position detection experiments with and without hysteresis compensation [65].

Parameter	**Value**
DC link voltage	24 V
Nominal power	12.9 W
Nominal resistance R_s	44.6 Ω
Nominal stroke	8 mm
Max. force	34.8 N
PWM frequency	500 Hz
Reset time t_r	50 μs
Integration gain	0.015 $1/\mu s$

Table 4.2: Parameters and nominal values of the used MSM GTC-A-40 actuator with settings of the IDIM technique used in the end position experiments with and without hysteresis compensation, adopted from [65].

In order to apply self-sensing approaches, first the characteristic of the inductance has to be fully studied. This has been obtained by using the above mentioned test-bench that allows to apply driving currents while the actuator plunger is fixed at a certain position. While modifying the actuator current and position in a dedicated measurement campaign, the characteristic of the incremental inductance can be obtained. Figure 4.9 shows the identified characteristic over the entire position and current range. In particular, the position was varied between 0 mm and 8 mm with a step size of 500 um while the current was varied between 0 A and 0.35 A with a step size of 50 mA. In order to increase visibility, the inductance was averaged over 200 values and in the three-dimensional plot, the hysteresis was removed by averaging the inductance value for the forward and backward directions. More in detail, the mapping is almost bijective for the entire working range except for small currents. In fact, for small currents, the knee of the B-H-curve is being operated, a section where the incremental inductance looses its monotonicity. In Figures 4.10a and 4.10b, the three-dimensional characteristic is cut for minimum, middle and maximum current and position values. The incremental inductance shows a remarkable hysteresis in the position dependency as well as the current dependency. For higher currents, this hysteresis gets smaller and vanishes nearly for the nominal current. This is especially visible in the current dependency measurement.

Nonetheless, the curves for minimum and maximum currents show a slight hysteresis and a nearly monotonous behavior over the position and those conditions are the usual working currents for an actuator in switching applications. Thus, only the red and black curve in Figure 4.10a are used for self-sensing the position in an end position detection scenario. The prefiltered identification curves are used as input for fitting a 4^{th} order polynomial, one for zero current operation and one for nominal current operation.

The prefiltering has been only applied for the training data of the polynomial, while in

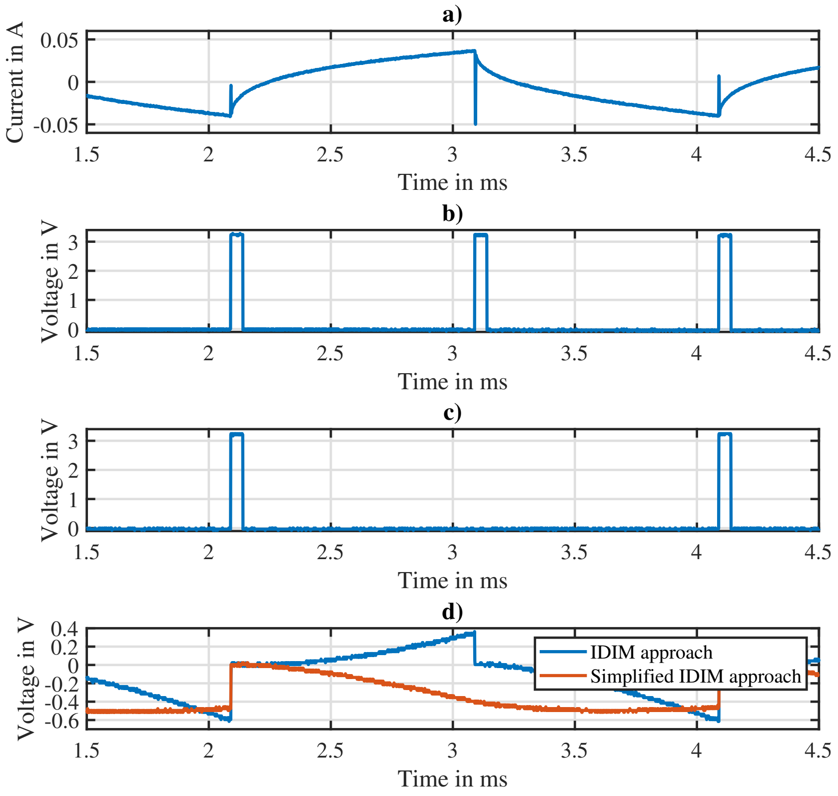

Figure 4.8: Measured signals of the analog circuitry that has been applied for the IDIM technique. From top to bottom: a) Current ripple in the actuator, b) Reset signal $r(t)$ for the IDIM technique, c) Reset signal $r(t)$ for the SIDIM technique and d) Resulting output $Q(t)$ of the integrator circuit [65].

the self-sensing experiment, unfiltered values for current and incremental inductance are used. Figure 4.11 illustrates an estimation of the actuator position when the actuator is without driving current and Figure 4.12 shows the estimate when the actuator is operated with nominal current. In particular, the estimated positions of the IDIM and the SIDIM techniques are compared with the measured position by the high-precision encoder from the test-bench. During the experiment, the plunger of the actuator has been moved with the linear position table in a quasi static manner in the forward and backward directions over the entire position range. For both operating currents, the IDIM and SIDIM techniques are able to track the position. As expected, the SIDIM technique shows less noise than the IDIM technique. In the case of the actuator without driving current, the IDIM and the SIDIM techniques track the position with a mean error of 0.13 mm and a mean error of -0.02 mm, respectively. The maximum error amounts to

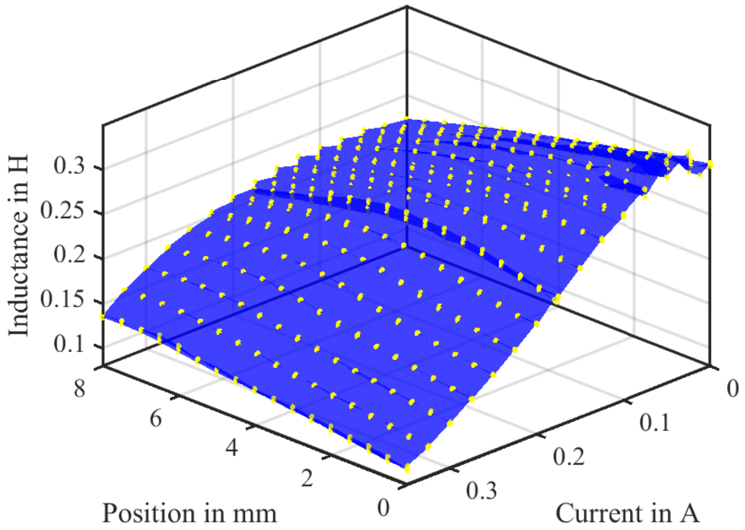

Figure 4.9: Characteristic of the incremental inductance of the MSM actuator over the entire position and current range. The blue curve is the interpolated behavior while the dots represent the measured working points [65].

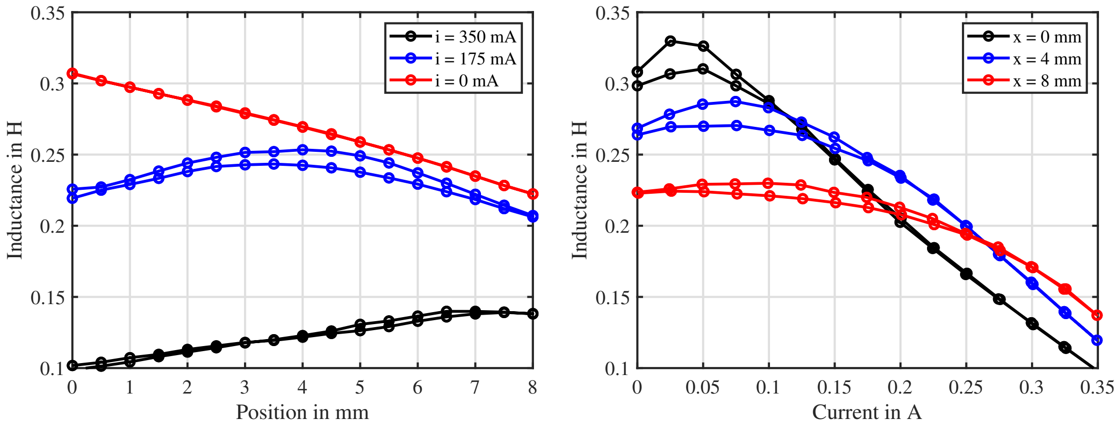

(a) Position dependency for fixed driving currents [65].

(b) Driving current dependency for fixed positions [65].

Figure 4.10: Characteristic of the incremental inductance of the MSM actuator for dedicated positions and currents.

2.11 mm in the IDIM case and to 1.28 mm in the SIDIM case. In the case of the actuator driven with nominal current, the estimates show a non-ideal following of the position due to the presence of ambiguities and magnetic hysteresis, which where not taken into consideration for this experiment and affect the estimation significantly. In particular, it can be seen that the estimate shows a different value for the forward and backward directions, which is caused by magnetic hysteresis. Nonetheless, the estimate for small positions is still good, which allows for a precise determination of the plunger position in case the actuator is nearly closed. The IDIM and SIDIM techniques exhibit a mean error of 0.98 mm and 0.79 mm, respectively, and a maximum error of 4.7 mm and 5.3 mm, which are mainly due to the unmodeled hysteresis effects.

To conclude, it can be said that the IDIM and SIDIM techniques are capable of identifying the actuator position in an end position detection scenario with good accuracy for the case with zero mean current and for small and middle positions in the case of nominal current. In case high currents and large positions are being used, the estimate is affected by hysteretic behavior that needs to be modeled. Thus, in the following section, a hysteresis compensation is evaluated for the shown switching actuator that allows for a quasi linear operation of the solenoid.

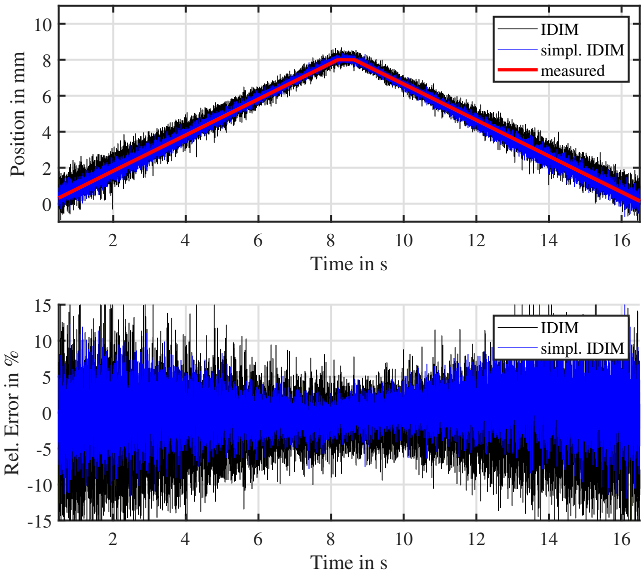

Figure 4.11: Self-sensed plunger position by means of the IDIM and SIDIM techniques compared to the measured position in case the actuator is driven with zero current and moved in a quasi static manner.

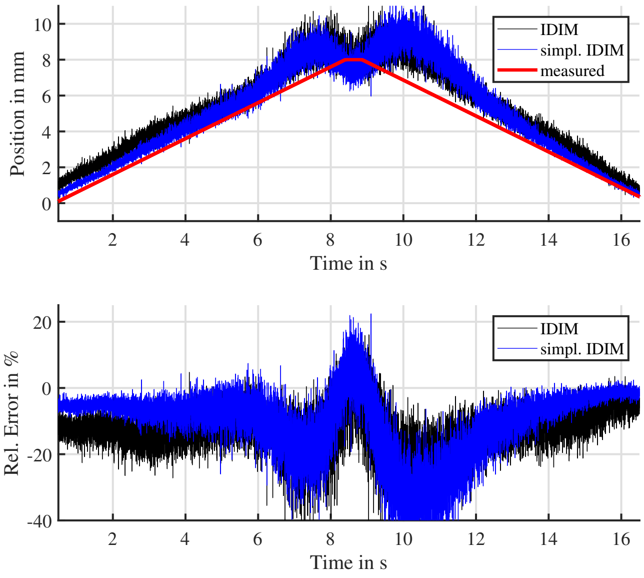

Figure 4.12: Self-sensed plunger position by means of the IDIM and SIDIM techniques compared to the measured position in case the actuator is driven with its nominal current and moved in a quasi static manner.

4.4.2 Position self-sensing with hysteresis compensation

In the following, the MSM actuator is used in a linear operation manner, so that the current can have more than two working points. The shown experimental results have been previously published by the author in [71]. Figure 4.13 shows the characteristic of the incremental inductance over current and position similar to Figure 4.9, but with highlighted hysteretic behavior. In particular, for increasing position (namely increasing air gap), the hysteretic curves get thinner. Instead for the maximum position, the hysteretic behavior nearly vanishes since for such large strokes, the ferromagnetic plunger is almost removed from the coil. For an air gap of 0 mm, the maximum width of the hysteresis is obtained since the core is fully inserted into the actuator. Figure 4.14 shows that hysterestic behavior of the incremental inductance at minimum air gap ($x = 0$ mm) for both positive and negative currents. The butterfly hysteresis from Figure 2.5 is obtained, with a slight asymmetric curve for positive and negative currents. This non-ideal behavior can be explained by the anisotropy of the material. It is observable for different materials, especially when being exposed to various fabrication processes that cause a preferred magnetization direction in the material [77].

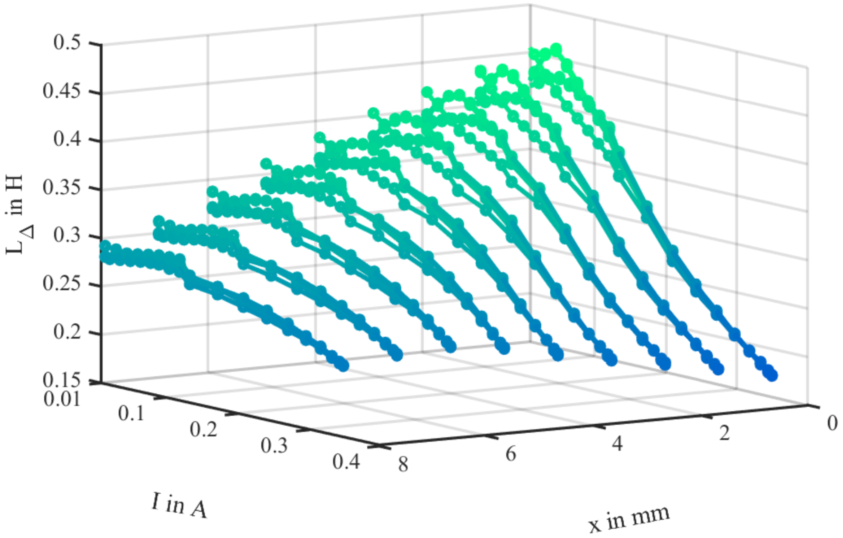

Figure 4.13: Characteristic of the incremental inductance over the entire position and current ranges with hysteresis [71].

The obtained incremental inductance from Figure 4.14 is the basis for the hysteresis model that is used for compensation of the electromagnetic hysteresis. First, the incremental inductance is numerically integrated over the current by means of Equation 3.142 to obtain the incremental flux. Figure 4.15 shows the obtained incremental flux over the current together with the identified hysteresis model. First, the experimentally

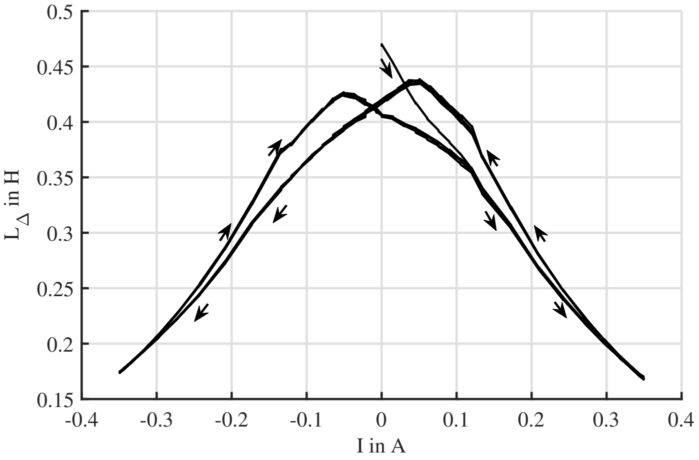

Figure 4.14: Incremental inductance for zero air gap ($x = 0$ mm) showing a butterfly hysteresis [71].

obtained incremental flux shows a BH-curve like hysteresis over the entire current range. Thus, it can be modeled by means of standard hysteresis models such as the MPI model that has been chosen. Figure 4.15 shows such MPI model, that has been trained on the experimentally obtained incremental flux. In particular, the MPI involves 6 play-operators and 10 superposition operators, which have been chosen as a good trade-off between accuracy and required computational resources. The trained model achieves a good accuracy with a maximum relative error of 1.6 % and thus it can be used for the hysteresis compensation algorithm. In the next experiments, only positive currents are considered since reluctance actuators are usually operated with unipolar voltage.

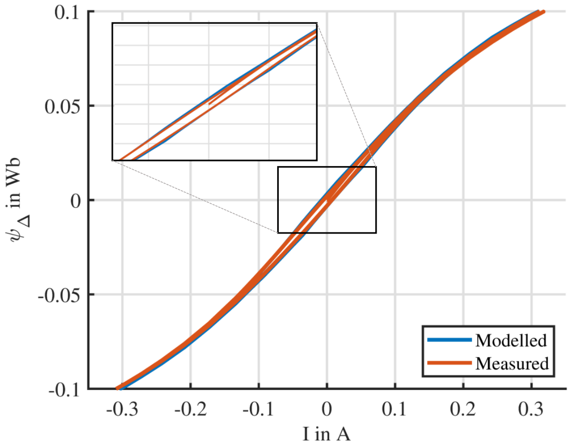

Figure 4.15: Experimentally obtained incremental flux together with the incremental flux estimated by the trained MPI model [71].

Based on the incremental flux and the actual actuator current, the total magnetic reluctance $\mathcal{R}_{\Delta tot}$ can be obtained for different positions and currents. Figure 4.16 shows the obtained characteristic for the forward and backward directions of the current for different fixed positions. It can be seen that the characteristic is strongly hysteretic and position-dependent. Hysteretic behavior and position dependency overlap each other, so that a position estimation is significantly degraded due to the hysteresis, making an unique position determination cumbersome. As expected, the total reluctance is increasing with increasing air gap.

In the following, the trained model from Figure 4.15 is used as estimator for the iron core reluctance $\hat{\mathcal{R}}_{\Delta Fe}$ and the characteristic from Figure 4.16 is used for $\mathcal{R}_{\Delta tot}$. Based on Equation 3.140, an estimate of the air gap reluctance $\hat{\mathcal{R}}_x$ can be analytically calculated, that is shown in Figure 4.17.

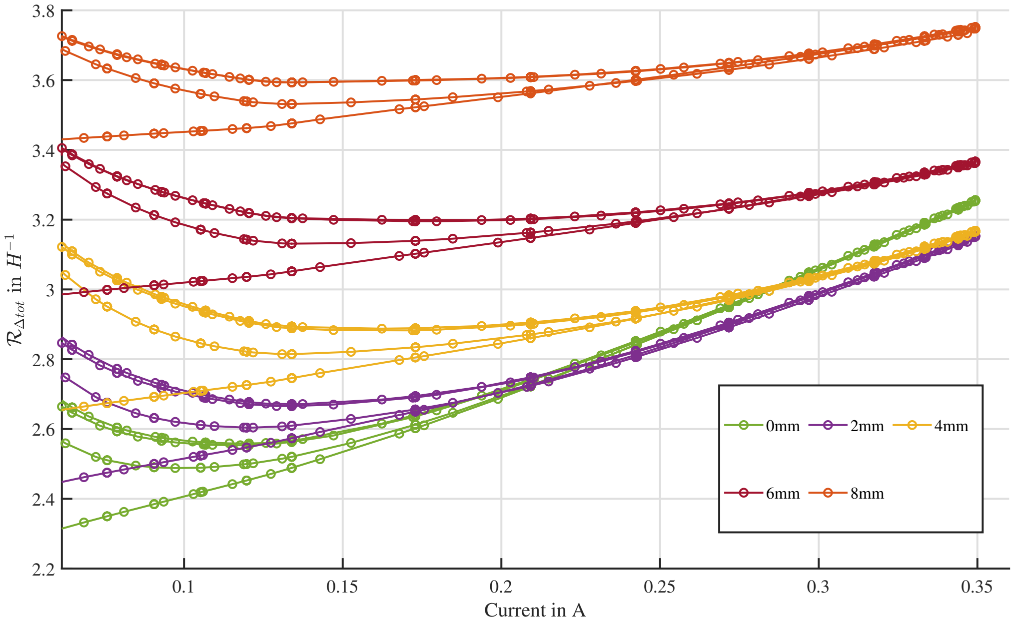

Figure 4.16: Characteristics of the total reluctance over the current for different fixed positions, adopted from [71].

Compared to Figure 4.16, this characteristic has less hysteretic behavior. Nevertheless, hysteretic effects are still visible which are mainly caused by modeling errors in the MPI model. Also, the air gap reluctance shows a little current dependency, although it should be theoretically current independent. This is also caused by modeling errors in the MPI model and unmodeled flux paths, such as leakage flux and parasitic air gaps in the magnetic circuit. Such inaccuracies also lead to a negative value of the reluctance

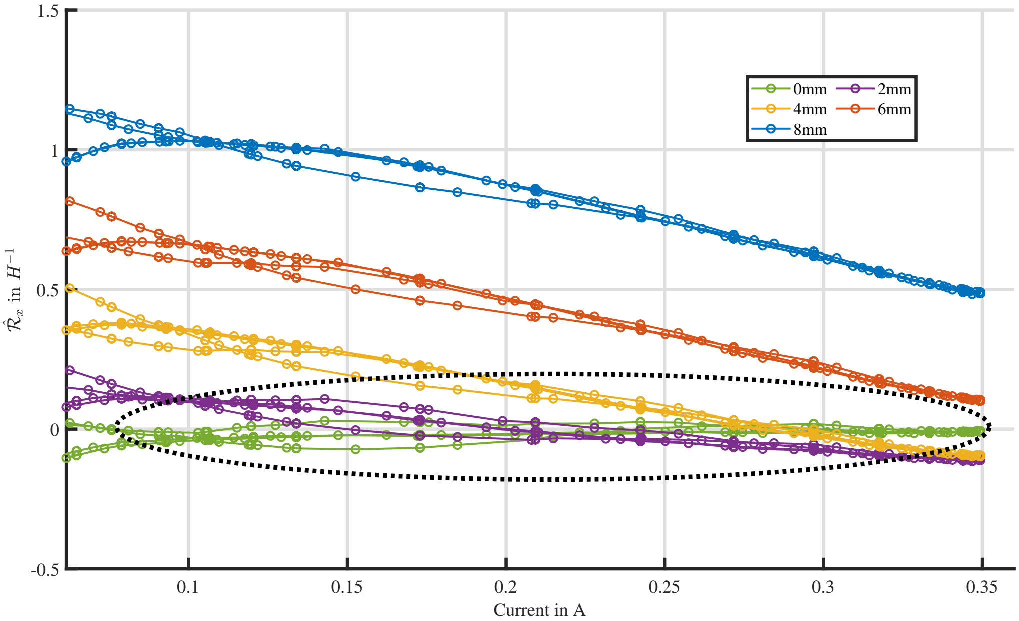

Figure 4.17: Characteristics of the air gap reluctance over the current for different fixed positions. The ellipse highlights ambiguous working points that are not considered during the self-sensing experiment, adopted from [71].

at 0 mm, which is physically not feasible. Increasing the modeling effort both in the magnetic equivalent circuit and the MPI model can address this issue. Nevertheless, the amount of hysteresis has been clearly reduced, so that in the position range from 5 mm to 8 mm, an unique position determination is possible since the curves do not overlap anymore. For smaller positions, the non-hysteretic curves still overlap. This is due to ambiguities in the characteristic of the incremental inductance of the actuator shown in Figure 4.9 and a low sensitivity of the inductance on the position in those working points. The ellipse in Figure 4.17 highlights these working points that do not allow for an unique estimation of the actuator position. In the following, these working points will not be considered, since for their compensation also the eddy current resistance R_p needs to be considered. While this is a favorable solution in actuators with little hysteretic behavior, a compensation of hysteretic effects involving both incremental inductance and eddy current resistance is a challenging task and an object for further research works.

By removing the ambiguous working points from the characteristic, the remaining mapping is completely strictly monotonous and can be exhibited for position estimation. The characteristic of the air gap reluctance $\mathcal{R}_x$ is modeled by means of a polynomial model with a model of the 3^{rd} order for the reluctance and a model of the 3^{rd}order for the current. As previously stated, the current dependency is mainly caused by unmodeled effects and, although physically not present, can be compensated by involving the current dependency into the polynomial. By doing so, an inverted function $f^-1(\mathcal{R}_x, i)$ is obtained that can be used for position estimation.

In the following experiment, the plunger of the actuator was moved in a quasi-static manner over the entire position range. While being moved, the current was varied from zero to its nominal value in forward and backward directions. The position controlled table ensures the position of the plunger stays fixed even under generated reluctance forces. In particular, the current loops have a finer step size around the origin in order to prove the capability of the model to track the initial curve of the actuator. Ambiguous working points have been operated but are left out of the validation since the resulting error would falsify the evaluation of the error metrics. Figure 4.18 shows the experiment in detail. At the top figure, the position of the actuator measured by the high precision encoder is compared to the estimated position in case the hysteresis is not compensated (x_{est}) and in case the hysteresis is compensated ($x_{est,c}$). The middle figure shows the current loops that have been applied. The current loops are unipolar with finer step size around the origin. The figure at the bottom shows the resulting relative error between the uncompensated (ϵ_{est}) and compensated ($\epsilon_{est,c}$) position self-sensing. It can be seen that the compensated algorithm tracks the position in a better way while, especially for small positions, the uncompensated estimator shows large deviations. In particular, the uncompensated estimator shows a maximum relative error of 49.3 % over all considered working points, while its compensated counterpart achieves a better performance with 9.0 % maximum relative error over the entire working space. For an air gap close to zero, the improvement gets relevant since the iron core has the most contributions to the total reluctance. It is clearly visible that, for the current peak values, the estimation error becomes the biggest in the case of the uncompensated estimator. For a larger air gap, the algorithms nearly show the same performance since the total reluctance is mainly composed of the air gap reluctance.

To conclude, it can be observed, that the presented hysteresis compensation allows to decrease the error in position estimation from 49.3 % to 9.0 %. Nevertheless, this is still a large, although often acceptable, error considering that the actuator at those working points exhibits low sensitivity and ambiguities.

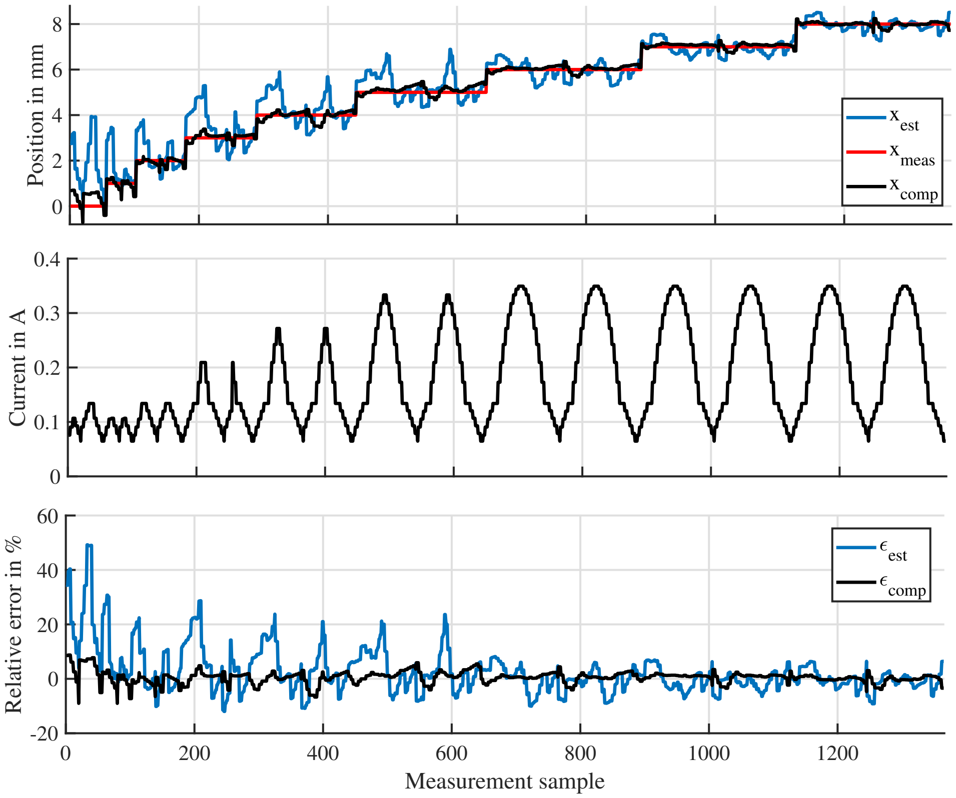

Figure 4.18: Validation of the proposed hysteresis-compensated self-sensing algorithm. Top: Comparison of the measured position to the estimated position obtained by the uncompensated and compensated algorithms. Middle: Driving current during the experiment. Bottom: Relative error between measured position and estimated position obtained by the uncompensated and compensated algorithms, adopted from [71].

4.4.3 End position detection on ambiguous actuator

In this section, the self-sensing algorithm in an end position detection scenario is studied in case the actuator exhibits a non-monotonous behavior of the incremental inductance. The actuator under test is the ITS-LZ 1949 from Red Magnetics [110], which is depicted in Figure 4.19 and its full specifications as well as settings for the IDIM technique are given in Table 4.3. The presented results have been previously published by the author in [66]. Figure 4.20 shows the measurement of the analog signals that are being evaluated. First, the current ripple is shown when the actuator is excited with a PWM with a frequency of 1000 Hz. In this actuator, the current cusps are clearly visible and they provide nearly the biggest contribution onto the current ripple itself. This is due to the fact that the actuator plunger is made of a solid piece of ferromagnetic material and the

Parameter	**Value**
DC link voltage	24 V
Nominal power	7 W
Nominal resistance R_s	23 Ω
Nominal Stroke	10 mm
Max. force	6 N
PWM frequency	1000 Hz
Reset time t_r	50 μs
Integration gain	0.015 $1/\mu s$
Meas. time t_{m1}^{+}	-12 μs
Meas. time t_{m2}^{+}	20 μs

Table 4.3: Parameters and nominal values of the ITS-LZ 1949 actuator from Red Magnetic used during end position detection experiments involving position ambiguities, adopted from [66].

actuator itself designed in such a way that the eddy currents are maximized in order to dampen the movement of the actuator. Along with the measured current ripple, also the trigger $r(t)$ and the resulting output signal $Q(t)$ of the integrator circuit are shown in case the full IDIM technique is applied.

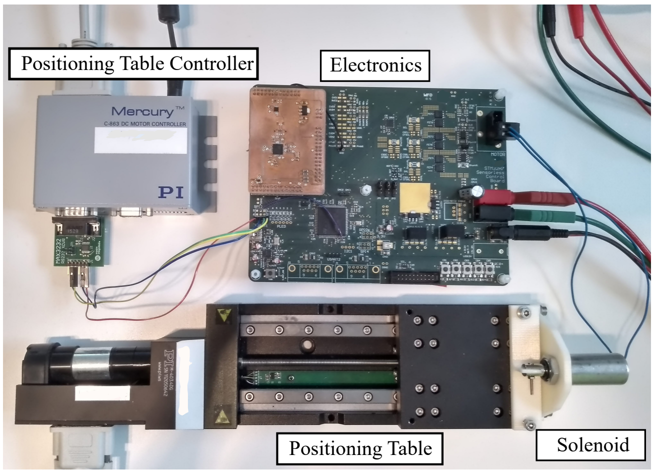

Figure 4.19: Actuator ITS-LZ 1949 from Red Magnetics used for end position detection experiments involving position ambiguities [66].

Similarly to the estimation scenarios before, a characterization campaign was conducted to obtain the measurements of the incremental inductance and the parallel resistance over the entire current and position range. In particular, the current was varied between 0 A and 0.4 A with a step size of 50 mA and the position between 0 mm and 10 mm with a step size of 500 um. The estimated values of the incremental inductance and the

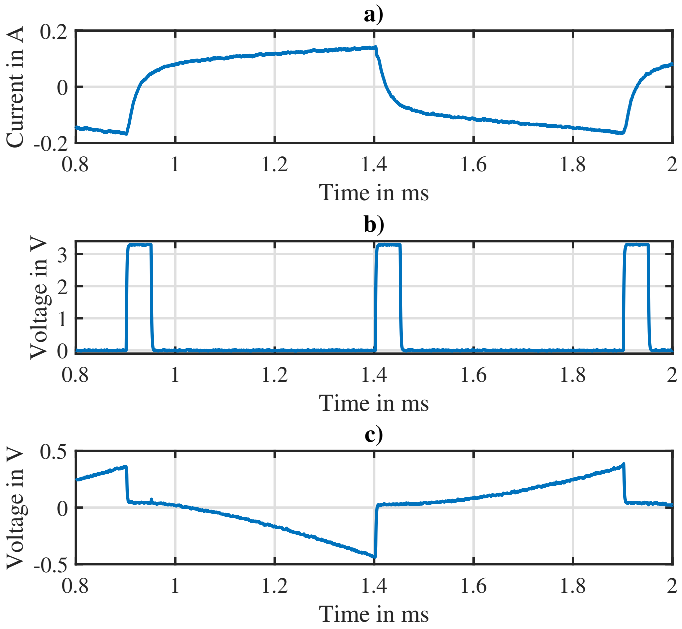

Figure 4.20: Measured signals of the analog circuitry that has been applied for the IDIM technique. From top to bottom: a) Current ripple in the actuator, b) Reset signal $r(t)$ for the IDIM technique and c) Resulting output $Q(t)$ of the integrator circuit [66].

parallel resistance were averaged over 1000 samples in order to allow a better graphical representation and, at the same time, for better tuning of the neural network. Figures 4.21a and 4.21b show the identified characteristics of the incremental inductance and the parallel resistance. In particular, Figures 4.22a and 4.22b show the dependency of the parameters on the plunger position at fixed currents. This representation is especially important for the purpose of end position detection.

The inductance characteristic shown in Figure 4.22a reveals a hyperbolic dependency of the incremental inductance on the position. Moreover, there is a significant current dependency. Especially for small positions, the inductance drastically decreases with increasing current due to the saturation of the plunger material. With increasing position, the saturation vanishes and the inductance increases again, until a maximum is reached and the inductance decreases again due to the removal of the plunger. The arising extreme point from this is current-dependent and moves along the x-axis for higher currents. Due to the presence of these extreme points, the inductance suffers from a non-monotonicity, which leads to an ambiguity in case only this parameter is exhibited for position estimation. Beside these extrema, the incremental inductance shows a slight

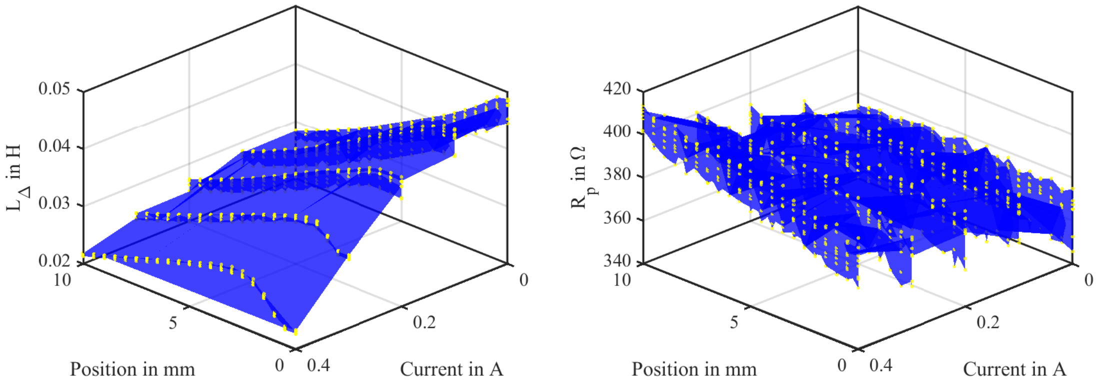

(a) Incremental inductance.   **(b)** Parallel resistance.

Figure 4.21: Characteristic of incremental inductance and parallel resistance of the Red Magnetic actuator over the entire position and current ranges. The blue curve is the interpolated behavior while the dots represent the measured working points.

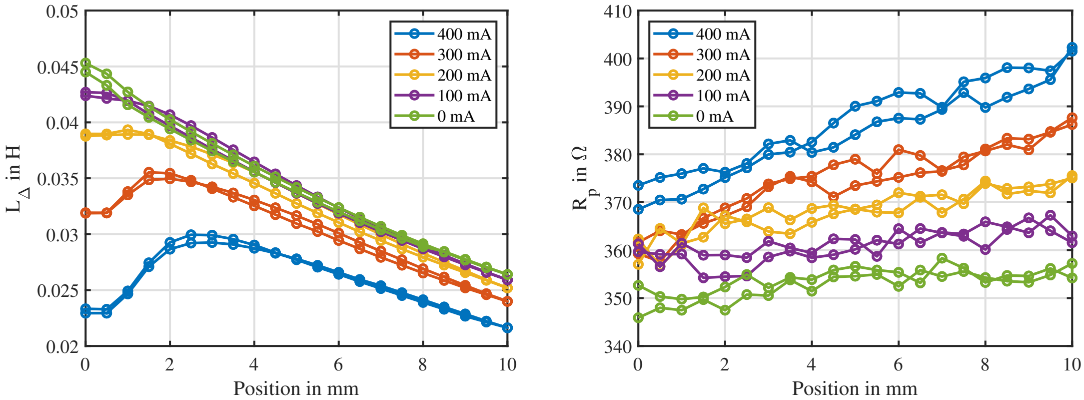

(a) Incremental inductance, adopted from [66]. **(b)** Parallel resistance, adopted from [66].

Figure 4.22: Characteristic of the incremental inductance and parallel resistance over the entire position range for fixed currents.

hysteretic behavior, due to the ferromagnetic material and due to mechanical hysteresis. Because of its small contribution to the characteristic, the effect of hysteresis is going to be neglected in the following experiments.

Instead, the parallel resistance characteristic, shown in Figure 4.22b, is almost linearly dependent on the position for the shown currents. The starting value and the slope of these curves increase with increasing current. Nevertheless, the estimate of the parallel resistance is strongly affected by a high measurement variance, as it is described also in the work [45]. Together with hysteretic components in the estimate due to ferromagnetic hysteresis and mechanical hysteresis, a linear interpolation is necessary. By applying this interpolation, the parallel resistance shows a monotonous behavior over the entire actuator working range and, thus, a position estimate is possible without any ambiguities. During the experiment, a significant dependence of the parallel resistance on the temperature was visible. In particular, the magnetic inductance and, consequently, the parallel resistance is strongly temperature dependent due to the term of the electrical conductivity as shown in Equation 3.120. In this experiment, the actuator was supplied with its maximum current to heat up completely and then the measurement campaign was conducted in a relatively short time in order to obtain a quasi isothermal result. In practice, the resistance estimator proposed in Section 3.1.3 needs to be implemented in order to estimate the copper resistance and consequently the coil temperature during self-heating that occurs in normal operation. This is a subject for further investigations.

In this experiment, a sensorless end position detection is going to be validated. Thus, only the characteristic for a driving current of $i_d = 0$ A and a nominal driving current of $i_d = 0.4$ A are relevant for this application scenario. For the case of zero driving current, a position estimator relying only on the incremental inductance can be used, since its curve is strictly monotonic, and consequently, an unique position estimation is possible. In this case, the curves for the forward and backward directions are averaged into a hysteresis-free curve and fitted by a polynomial model of the second order. In the case of the actuator driven with nominal current, the characteristic is ambiguous and a globally invertible function does not exist. In particular, the extreme point occurs at approx. 2.5 mm, while before and after the characteristic is monotonous. Thus, the parallel resistance R_p needs to be considered. This is done by means of a data fusion algorithm based on a neural network.

Data fusion algorithm Taking into consideration merits and demerits of the identification procedures for incremental inductance and eddy current resistor, merging of the information is desirable. In particular, the parallel resistance can deliver a rough estimate, in what monotonic area the position estimate lays, while the inductance information can deliver a precise estimate. Thus, it is possible to combine advantages of both approaches, namely precision and uniqueness. Works from literature mainly apply a binary decision making algorithm based on the identified value of R_p [56]. Nevertheless, this approach can fail when e.g. the noise resulting from the estimation of R_p triggers the decision making rule. Instead, in this experiment, an MLP is used for data fusion. During training, the MLP can adapt its weights in such a way that more attention is given to the incremental inductance and less attention to the parallel resistance, that is only used around the extremum point as supporting information. Thus, a MLP with two inputs L_Δ and R_p is created. Behind the input layer, there is a hidden layer with 15 neurons based on a sigmoidal activation function. The output layer that estimates the position is based on one neuron with a linear activation function. The weights of the MLP are trained based on the Bayesian Regularization back-propagation algorithm and by dividing the measurement data into training, validation and test sets. Also, in this fitting approach, the hysteresis is canceled by calculating the average of the forward and backward curves. Given the relatively small size of the neural network, the estimation algorithm is still computationally lightweight in combination with the IDIM technique.

Figure 4.23 summarizes the algorithm in detail: a current controller based on the modulus optimum criteria ensures a stable control of the actuator current. The electromagnetic actuator from Red Magnetics is operated by a H-bridge with current sensor. This current sensor is used for the estimation of the incremental inductance by means of the IDIM technique and of the parallel resistance by means of the estimator shown in Section 3.3. Both estimates are filtered by a low-pass filter. Since the estimate of the parallel resistance is very noisy, a cut-off frequency of 20 Hz is chosen. Although the incremental inductance does not need further filtering, the same filter is used to avoid phase shifts between the estimates, that would lead to an identification bias. Then, the above mentioned MLP is applied for position estimation.

The end-position detection experiment is conducted by exposing the actuator either to zero current or to nominal current and moving the plunger by means of the linear positioning table in a quasi-static manner over the entire position range. The position measured by the high-precision encoder serves as reference. Also here the experiment was conducted in a short time to overcome the effect of self-heating. Figure 4.24 and Figure 4.25 show the estimated position compared to the reference sensor and the relative error for the zero and nominal current conditions. In the case of zero current, the polynomial approach is able to track the position with a relative error less than 2.7 % referred to the nominal stroke of 10 mm of the actuator. The estimation algorithm is consequently able to reconstruct the position in a quantitative and qualitative manner.

In the case of nominal current, the algorithm based on the data fusion MLP is also able to reconstruct the position without any ambiguities with a maximum relative error of approximately 8 %. Especially the critical position at 2.5 mm is reconstructed although,

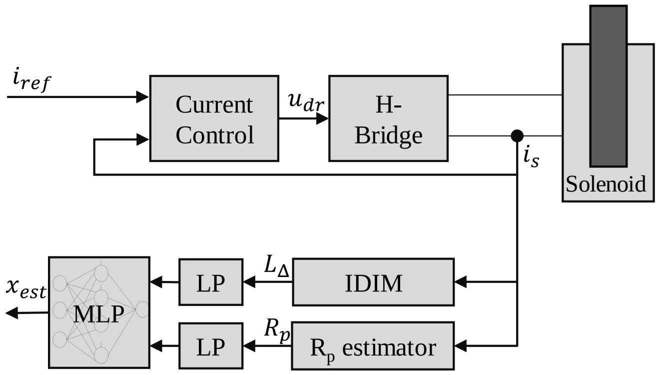

Figure 4.23: Schematic of the data fusion algorithm based on a MLP relying on inductance and resistance estimation, adopted from [66].

at this position, the relative error is at its maximum. In this particular working point (visible around the time intervals [1 s 3 s] and [15 s 17 s]), the estimate is especially affected by a low SNR. Due to a vanishing sensitivity of L_Δ at this position, the position estimator only relies on the value of R_p. Thus, the low SNR of R_p leads consequently to a low SNR of the estimated position. Nevertheless, the estimator shows errors of around 2% at the minimum and maximum stroke, showing that the presented approach can reconstruct the position over a large position range. Nonetheless, there is still a slight influence of hysteresis, which is visible in different estimated positions for forward and backward directions: in the time interval [4 s 8 s], there is a negative error of -3 % while for the same reference position in backwards direction at the time interval [10 s 14 s], a positive error of 5 % is obtained. This deviation can be explained by the hysteretic dependency of both parameters that was neglected during the experiment. Future works can involve the hysteresis compensation explained in Section 4.4 together with the parallel resistance in order to overcome these limitations. In conclusion, it can be observed that, by applying the above mentioned data fusion neural network, the ambiguities are solved and an unique position estimation with less than 8 % relative error is possible on actuators that are affected by non-monotonicity.

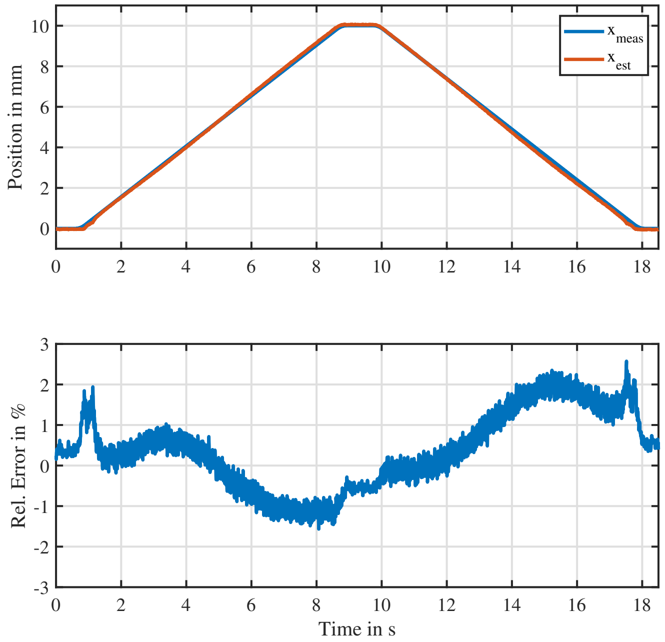

Figure 4.24: Position estimation when the actuator is at zero mean current. Top: Estimated compared to measured position. Bottom: Relative error [66].

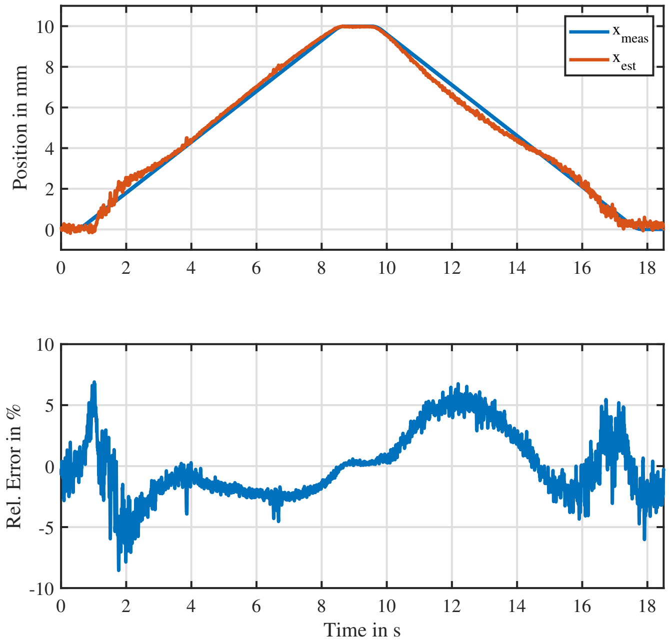

Figure 4.25: Position estimation when the actuator is at nominal mean current. Top: Estimated compared to measured position. Bottom: Relative error [66].

5 Sensorless control of an active magnetic levitator

In the following, the self-sensing algorithm shown in Chapter 3.1 will be applied on an electromagnetic levitator to prove that the discussed technique is able to estimate the position in a reliable manner also in closed-loop systems with sensorless position feedback. Electromagnetic levitators (EML) are popular systems used for the validation of sensorless techniques due to their inherent instability and their non-linear system dynamics. Thus, they require high demands concerning quality of the position feedback, control bandwidth and stability, and hence, serve as a good benchmark system. In particular, the works [34, 51, 53, 111] use such kind of EMLs in order to prove the robustness and stability of their self-sensing approaches. In the following, the IDIM technique will be evaluated on such an EML device with particular focus on stability, robustness and computational lightness. In particular, a similar test-bench compared to [51] is used, where a single coil is able to levitate a hollow steel ball. Ferrite core and hollow ball are dimensioned according to [51] in order to have a comparable validation test-bench. Similarly to this work, the ferrite core PM 87/70 from TDK [112] is used. The identified parameters of the actuator as well as the used IDIM settings are summarized in Table 5.1. Figure 5.1 shows the realized experimental test-bench consisting of a coil with ferrite core, a hollow steel ball with a diameter of 40 mm, the electronics that is based on the PCB shown in Chapter 4, and a high-precision laser sensor with 10 μm accuracy used for comparison. With the presented experimental test-bench, self-sensing experiments are carried out, which are explained and discussed in the following. The presented results have been previously published in the work [70].

System dynamics Figure 5.2 shows the physical working principle of an electromagnetic levitator. A current in the coil generates a magnetic flux which flows through the air gap and the ferromagnetic object. In this case, the object resembles a ferromagnetic steel ball and is called flotor. As explained in Chapter 2.1, the system tries to minimize its energy by decreasing the air gap, thus generating a force that pulls the flotor towards the coil. The counteracting force is solely the gravity force and the initial force of the flotor.

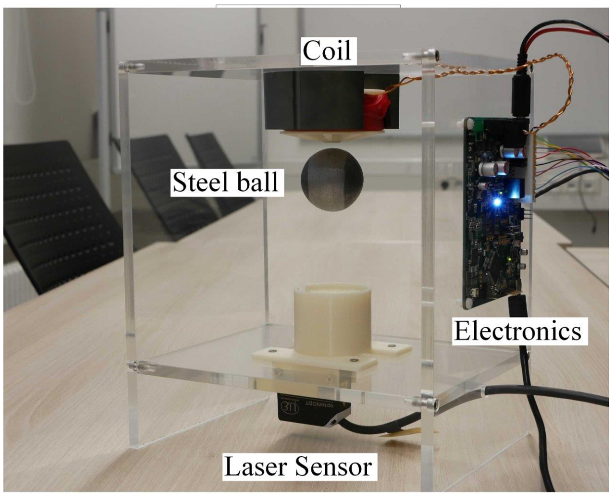

Figure 5.1: Electromagnetic levitator set-up including coil, flotor and electronics involving the sensorless control algorithm and laser sensor for comparison [70] (©2019 IEEE).

Parameter	**Value**
DC link voltage	24 V
Nominal resistance R_s	2.4 Ω
Nominal stroke	10 mm
Electromagnetic constant C	$3.3 \cdot 10^{-5} Nm^2/A^2$
Position x_0	3 mm
Mass of the flotor m	80 g
PWM frequency	1000 Hz
Controller sampling frequency	1000 Hz
Reset time t_r	3.1 μs
Integration gain	0.008 $1/\mu s$

Table 5.1: Parameters of the electromagnetic levitator used during the experiments involving sensorless control, adopted from [70].

The system dynamics can be written as:

$$m \cdot \ddot{x} = m \cdot g - F_m(x, i), \tag{5.1}$$

with m being the mass of the flotor, g being the gravity constant equal to $9.81\ \frac{m}{s^2}$, x being the air gap and F_m being the reluctance force. In this model, air friction is neglected due to its minimal contribution to the overall forces. The magnetic force is solely attracting and can be represented by the well-known quadratic dependency on the current and inverse quadratic dependency on the air gap, as given in the work [34]:

$$F_m(x, i) = C \cdot \frac{i^2}{(x - x_0)^2}, \tag{5.2}$$

with an additional term x_0, that represents a residual air gap. Such an introduction of x_0 allows to simplify the control of the system due to the absence of an infinite force at zero air gap. The parameter C is called electromagnetic constant and models the relationship between current, position and force. From the model it can be observed, that the system is inherently nonlinear and unstable. Thus, a control algorithm considering the nonlinear dynamics of the system needs to be applied.

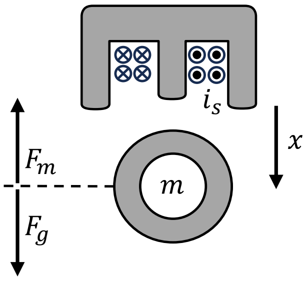

Figure 5.2: Physical working principle of electromagnetic levitation. Reluctance force F_m counteracts the gravity force F_g.

Characterization of the EML actuator Similarly to the discussed actuators in Chapter 4, a characterization campaign is carried out in order to obtain a complete mapping of the incremental inductance over current and position. This allows identifying a model that is later used for self-sensing. Contrary to the previously discussed actuators, the EML actuator is inherently unstable, making a systematic characterization of all the working points cumbersome. Thus, only working points for dedicated conditions are recorded, e.g. for vanishing air gap and infinite air gap. Middle positions are obtained by clamping the ball to the mechanical framework of the test-bench. Figure 5.3 shows the identified characteristic over the entire current and position range. In particular, the figure shows the already identified mapping that was obtained by fitting a polynomial with a order of 3 for current and position. Figure 5.4 shows the current dependency for the discussed positions of vanishing air gap and infinite air gap. In this case, the air gap not only consists of a magnetic but also a mechanical air gap due to the mechanical framework of the set-up. Thus, for a position of x = 7 mm, the flotor already touches the mechanical body of the coil, while there is still a magnetic air gap.

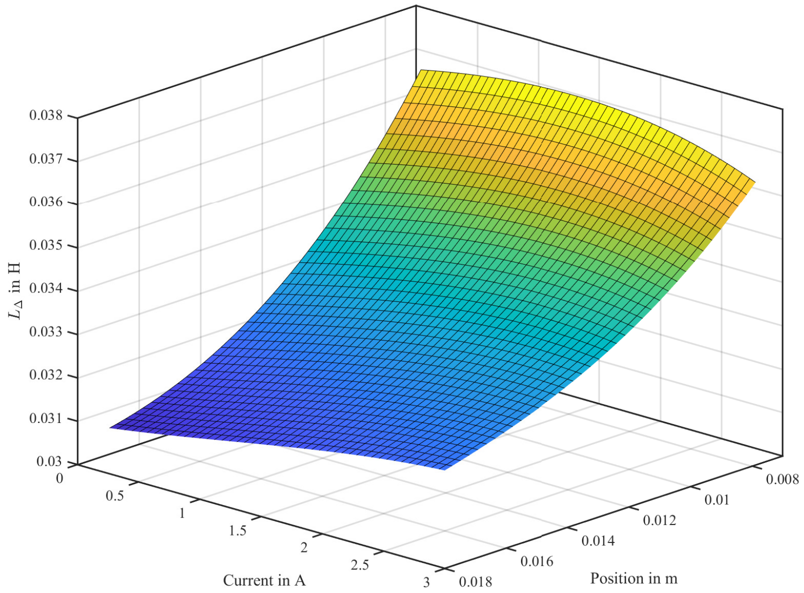

Figure 5.3: Characteristic of the incremental inductance of the EML actuator over the entire position and current ranges. The characteristic is interpolated based on measured data points, adopted from [70].

When the air gap is infinite, the incremental inductance is linearly dependent on the driving current. It increases about 3 % over the entire current range. This slight increase in inductance can be explained by the ongoing magnetization process in the ferrite core material, where μ_Δ increases for increasing current. When the flotor touches the coil (x = 7 mm), the effect of the ferromagnetic flotor is visible. The incremental inductance increases by 23 % and exhibits a hysteretic behavior. Furthermore, the incremental inductance saturates at higher currents. Because of the hysteretic effects as well as saturation effects, the mapping is not bijective anymore starting from currents above 2.5 A. When excluding these currents from the EML actuator working range, the hysteresis effects can be neglected and a monotonous mapping is obtained. Consequently,

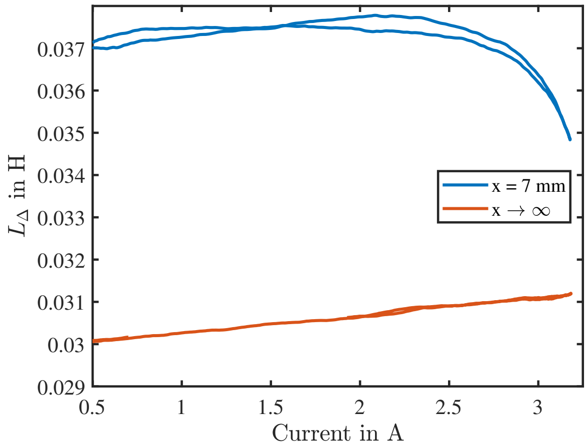

Figure 5.4: Characteristic of the incremental inductance of the EML actuator over the entire current range for two given positions: the flotor is near the coil (blue) and the flotor is in infinite distance from the coil (red), adopted from [70].

the above mentioned polynomial of the third order for current and position dependency can be applied, that allows for a unique position estimation in the current range up to 2.5 A.

Control strategy The EML application resembles an electro-magnetic-mechanical system with non-linear characteristic. For controlling such a system, a control strategy has been designed that is summarized in Figure 5.5. A cascaded control approach is chosen with an outer position control loop and an inner current control loop. The underlying electrical system is controlled by a dedicated current controller with an reference current as input and the driving voltage as output. In particular, the current controller is a PI controller whose gains are tuned based on the modulus optimum criteria [11] with the given electrical parameters of the coil. The driving voltage is then generated by a PWM-operated H-Bridge. The position controller is based on a Super-Twisted Sliding Mode Controller (STSMC). The STSMC takes the reference position and the actual position and calculates the magnetic force that is needed for stabilizing the position of the flotor. The magnetic force is non-linearly dependent on position and current. Consequently, it represents a static nonlinearity and can be inverted for the given working conditions. Thus, the characteristic can be linearized by applying output linearization by means of the inverted model. The position feedback is closed with the self-sensed position obtained by the IDIM technique and the inverted polynomial model based on the current and the estimated incremental inductance.

The position controller is chosen to be a STSMC due to the high robustness of such

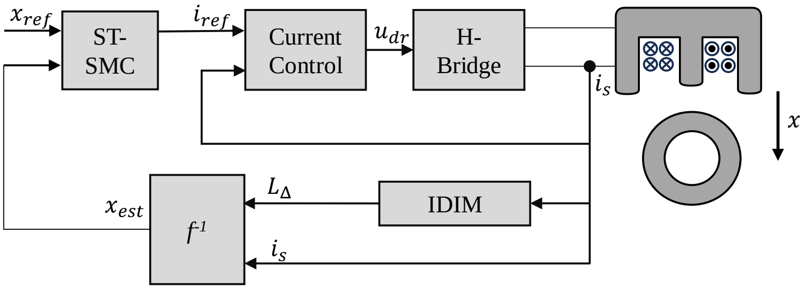

Figure 5.5: Overall schematic of the closed loop control scheme, including the inductance estimation by means of the IDIM technique, the inductance model, the STSMC position controller, current controller and H-Bridge, adopted from [70].

type of controllers towards model uncertainties, external disturbances and parameter uncertainties. This is especially helpful for the given EML actuator since there will be modeling errors due to the neglected hysteretic behavior and parameter variations due to a temperature rise. While a thorough analysis and description of such controllers would clearly expand the scope of the thesis, only basic relationships are given here for general comprehension. The interested reader is guided to a fundamental book [113] for further derivations and theoretical background. Sliding Mode Controllers (SMC) of the first order achieve a high robustness to uncertainties and disturbances due to a discontinuous control term based on the signum function:

$$sign(\sigma) = \begin{cases} 1 & \text{for} \quad \sigma > 0 \\ 0 & \text{for} \quad \sigma = 0 \\ -1 & \text{for} \quad \sigma < 0 \end{cases} , \tag{5.3}$$

with σ being the sliding variable that represents the error in the system. Applying such a signum function in the control law allows eliminating bounded uncertainties and disturbances in the theoretical case of infinite bandwidth. Nevertheless, in discrete systems, the usage of such a function inherently introduces a high-frequency content in the control action, the so-called chattering, that is usually undesired. The problem of chattering has been addressed by higher order SMCs, where the signum function is placed on derivatives of the control action instead on the control action itself. A particular version of a second order SMC is the STSMC, which strongly decreases chattering [113]. In the reference tracking problem, the error between reference and actual position can be formulated as

$$\epsilon = x - x_{ref}, \tag{5.4}$$

and based on the error, a suitable sliding variable can be chosen:

$$\sigma = \dot{\epsilon} + \lambda \epsilon, \tag{5.5}$$

with λ being a gain parameter. Based on the chosen sliding variable, the control law of the STSMC can be applied [113]

$$F_m = \lambda \cdot sign(\sigma) \cdot \sqrt{|\sigma|} + \omega, \tag{5.6}$$

$$\dot{\omega} = b \cdot sign(\sigma), \tag{5.7}$$

with b being a tunable factor and ω being a helping variable. It can be seen that in this case the signum function only acts on $\dot{\omega}$, and consequently, the chattering can be reduced by the integration of that variable. The control law is able to drive $\sigma \to 0$ and thus $x \to x_{ref}$ by applying a certain magnetic force F_m [113]. Convergence to the reference position is guaranteed even when an external disturbance $\Phi(x, \dot{x}, t)$ is present, whose derivative is bounded $\dot{\Phi}(x, \dot{x}, t) < L$. In this case, L represents a Lipschitz constant and can be used for tuning of the parameters λ and b [113]. For further theoretical background and proof of convergence reference is given to [113].

Experimental results In the following, the performance of the discussed sensorless control approach is verified on the experimental set-up. In particular, the SMC parameters have been chosen to $\lambda = 20$ and $b = 8$ as a good trade-off between reference tracking and remaining chattering. Then, stepwise and sinusoidal reference positions are given to the controller to validate the reference tracking of the controller. The position feedback is closed with the self-sensed position, while the sensor only serves as comparison measurement.

Figure 5.6 shows the performance of the controller for the stepwise and sinusoidal references. At the top figure, the measured, estimated and reference position are shown and compared. The middle plot indicates the driving current that is applied. The bottom plot shows the deviation between measured and estimated position. In the case of the stepwise reference, the controller is able to stabilize the flotor in the given positions and is able to track the reference position with a maximum error of 1.5 mm. The transitions between the reference steps are followed in a stable way with small settling time. The position error consists of a high-frequency component and a static component. The high-frequency component is based on the high-frequency content in the driving current which is caused by the remaining chattering. Because of this, small errors in the position estimation are introduced which are fed back into the system, thus causing more chattering. The static error is mainly caused by the modeling errors in the incremental inductance. As stated previously, hysteretic effects have been neglected in the phenomenological modeling of the incremental inductance. Thus, it can be seen that, especially for small air gaps, where the contribution of the hysteretic flotor is more present, the error increases. For larger positions, the error minimizes. In the case of the sinusoidal reference, the same observations can be made. The flotor is able to levitate in a stable way and follows the reference in a clear way with minimal phase shift. Also here, the error consists of two contributions: a static one and a high-frequency one, which are caused by the above mentioned problems.

In the complete experiment, it is visible that the self-sensing based control has a significant merit compared to the sensor-based control. While the laser sensor only measures a small spot on the surface of the flotor, the self-sensing technique is able to sense "the volume" of the flotor. Thus, small deviations in the y- or z-directions have less influence on the position information in the self-sensing case than in the sensor-based case. Consequently, higher stability and robustness can be achieved by this kind of control.

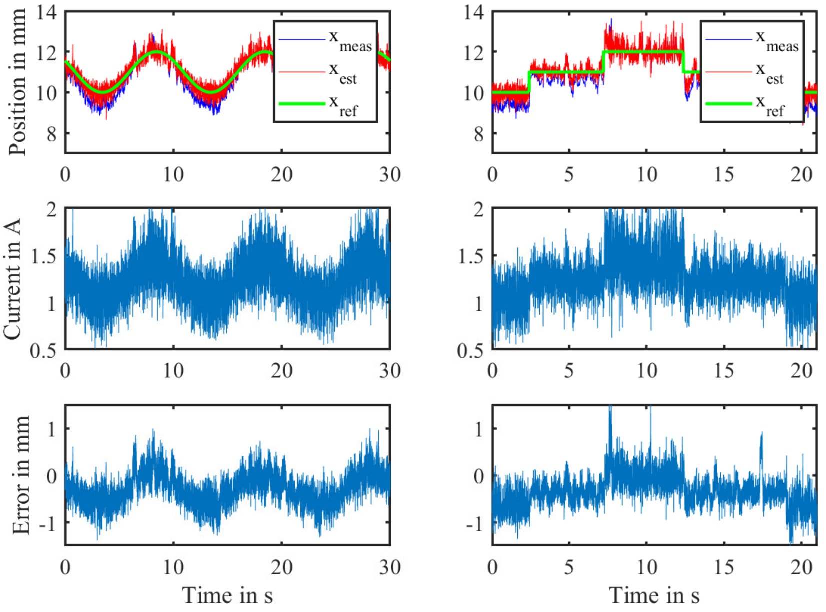

Figure 5.6: Position controller with sinusoidal (left) and step (right) references. Top: Reference position compared to measured and estimated position, Middle: Applied driving current, Bottom: Position error between estimation and measurement, adopted from [70].

6 Conclusions

6.1 Summary and discussion

Electromagnetic actuators such as solenoids are well established since around 200 years. Their simple and robust construction has the merit of high forces and large strokes but the demerit of a nonlinear force characteristic involving hysteresis. Thus, sophisticated control methods including position sensors are required. In high quality applications, the sensor is usually embedded into the actuator system. Instead, in the low-cost segment or in environments, where sensor wiring is cumbersome, sensors are avoided and the actuators are driven in an open loop manner with reduced efficiency and performance. Self-sensing, which is based on the estimation of mechanical quantities through electrical measurements, seems therefore desirable. Such self-sensing relies on three physical principles, namely the magnetic flux, the inductance and the iron losses. The first one is only able to operate at middle to high speeds while the latter ones allow an estimation in standstill and low-speed conditions.

This work focuses on the position estimation at low speeds and standstill since the actuators under observation are mainly used for position applications. Compared to well-known injection-based approaches, this work uses the current ripple that is inherently induced by PWM-switching electronics. After a basic introduction into the working principle of those actuators and the properties of softmagnetic materials, an electrical equivalent circuit for those actuators is developed under the consideration of iron losses. Based on this, a self-sensing strategy is proposed with the main focus laying on the reduction of computation and measurement effort. Since the estimation through the incremental inductance shows ambiguities at higher currents, an additional estimation strategy based on iron losses is considered. Through a data fusion by means of an ANN, a unique position estimation can be obtained. Another point concerns the hysteresis that affects the position estimation significantly. In order to compensate for hysteretic phenomena, an approach involving a core separation principle is presented. Experimental results on industrial actuators prove the accuracy and robustness of the presented techniques. In the last chapter, a sensorless control of an electromagnetic levitator is shown that proves the robustness of the technique in case the estimated position is used as feedback signal.

In the following, the main contributions of the work are being highlighted and discussed.

Modeling and analysis of current ripples

For a successful implementation of position self-sensing techniques, the modeling of the underlying physical effects is crucial. This work starts from the properties of softmagnetic materials. A physical model describes the position dependency of these properties by means of magnetic equivalent circuits. In particular, the magnetic characteristic of the back-iron, plunger and the air gap is studied under the consideration of eddy currents, and, for larger material sizes, the skin effect. Based on the magnetic equivalent circuit, an electrical equivalent circuit is derived that transforms the magnetic effects into electrical components such as resistance, inductance and back-EMF voltage, that can be analyzed based on well-known circuit theory. In particular, the circuit is simplified to a combination of series resistance, series inductance and parallel resistance when a PWM voltage is applied. In case of neglected iron losses, the classical current response of a first order system to a step voltage is obtained. In case iron losses are considered, cusps in the current are visible and an additional term representing the decay of eddy currents is visible. The height of such a cusp is dependent on the parallel resistance, and, consequently, on the position. Such an analytical model of the current ripple under PWM excitation is a contribution to the state-of-the-art, where only numerical models existed. It serves as a basis for the self-sensing strategies that are being proposed. Experimental results prove that the model achieves a fit performance of 87% while keeping the computational effort low.

Computational lightweight self-sensing

Based on the obtained analytical model of current ripples, a self-sensing strategy is proposed that estimates the actuator position by exploiting the position dependency of the incremental inductance and the parallel resistance. Using the current ripple is a minimally invasive approach, since no further injection is required and the PWM excitation is inherently available in the system. In particular, the IDIM technique for the estimation of the incremental inductance is presented, that processes the current ripple by means of an analog integrator circuit with reset. This allows, on one hand, a robust identification of the inductance since current derivatives are avoided, and, on the other hand, a reduction of the computation and measurement effort since oversampling is avoided. Thus, the technique can be implemented in cost-critical applications. Beside the IDIM technique in its full derivation, a simplified IDIM technique is presented in case less estimation bandwidth is required. This SIDIM technique relies on a simplified current ripple model, where iron losses are neglected and a linear slope of the current ripple is assumed. Therefore, the SIDIM technique is suited for quasi-static position estimation and requires less measurement samples and calculations than the IDIM technique. Moreover, the SNR is increased due to the absence of current differences in the estimation process. Experiments on a switching actuator are conducted that show the signal quality of the IDIM and SIDIM techniques compared to a well-known oversampling technique. It can be seen that the SIDIM technique is able to outperform the IDIM technique and oversampling approaches with up to 1000 samples per PWM period in terms of noise power while the IDIM technique outperforms oversampling approaches with up to 100 samples per PWM period. Following these results, an experiment validated the position detection in case of a switching actuator. In particular, the (S)IDIM technique is able to identify the actuator position in a precise way for the undriven actuator, while, for the actuator under nominal current, an error occurs due to working points showing ambiguities and hysteretic behavior. It has to be denoted, that in those experiments, no low-pass filtering was applied, in order to observe the estimation noise, and the estimation variance can be drastically decreased by implementing such type of filter.

An additional experiment involving an electromagnetic levitator proves the robustness of the technique in case a position control loop is closed with the estimated position as feedback. In the presented case of a sinusoidal and stepwise reference, the control loop maintained stable and was able to stabilize the flotor in case of a large air gap ($x = 12\ mm$).

Furthermore, an error analysis was conducted that shows the sensitivity of the technique towards measurement and electronic component variations. It has been identified that a gain and an offset error are critical errors that affect the estimation accuracy significantly. In order to address this issue, while keeping the component costs low, an ASIC was designed that embeds the integrator circuit by means of the Switched Capacitor technology. By applying this type of technology, the integrator stage exhibits tight tolerances and can be parameterized during operation.

Solution to ambiguities

The incremental inductance can show non-monotonicities at higher currents in certain actuators, that leads to the presence of ambiguities. State-of-the-art works use the parallel resistance as further estimation input to solve these ambiguities. In this work, the parallel resistance is estimated by means of a computationally lightweight method, that requires only 3 measurements per PWM period. Thus, it serves as a good extension to the IDIM technique in terms of implementation effort. Instead of binary rules and/or look-up-tables, that are being used in the state-of-the-art, this work applies a lightweight MLP for the data fusion of the incremental inductance and parallel resistance. This leads to a higher accuracy and a higher SNR since the estimates of the incremental inductance and parallel resistance are weighted based on their information content. The experiments on an industrial actuator prove that the combined estimator is able to track the position with less than 2.5% of error.

Hysteresis compensation

For the case of actuators exhibiting significant hysteretic behavior, a hysteresis compensation based on a separation principle is presented. In particular, the B-H curve hysteresis is modeled by the well known Modified Prandtl-Ishlinskii (MPI) model, which is a phenomenological model with inherent algebraic invertability and reduced calculation effort. The separation principle allows to isolate the hysteretic behavior of the iron core from the non-hysteretic behavior of the air gap, and, consequently allows to reduce the position and current dependent hysteresis into a hysteresis, which is only current dependent. Nevertheless, the incremental inductance shows a butterfly hysteresis that cannot be modeled by standard hysteresis models. Consequently, this work introduces a transformation approach that allows to link the butterfly hysteresis with the B-H curve hysteresis. In experimental validation, the hysteresis compensator is applied to an industrial switching actuator. By using the hysteresis model that has been pre-identified, and by excluding working points with poor position sensitivity, the hysteresis compensator is able to reduce the position error from 49.3% to 9%.

6.2 Outlook

During the experiments, certain effects and limitations have been discovered that can serve as a starting point for future research activities:

Temperature effects

Electromagnetic actuators are usually driven close to their thermal limits. Thus, a significant temperature range can be covered due to self-heating or because of environmental influences. As seen during the experiments, the parallel resistance exhibits a strong influence on the temperature due to the temperature dependency of the electrical conductivity. Furthermore, the incremental inductance is slightly temperature-dependent. As already discussed, an estimation of the copper resistance, e.g. by evaluation of the series resistance or by identification through LMS/RLS approaches, can serve as basis for temperature estimation and compensation. While this solution seems theoretically simple, further modeling and validation effort has to be undertaken. In particular, different ambient temperatures have to be simulated, e.g. by means of a climate chamber.

Extending the hysteresis model

As seen within the self-sensing experiments with hysteresis compensation, further research steps have to be taken in order to extent the hysteresis compensator for industrial applications. First, the experiment was conducted in a quasi-static manner. While this still serves as a good application scenario for low-speed actuators, the model needs to be extended for dynamical operation. In particular, the hysteresis needs to be tracked reliably during dynamic operation, and the frequency dependency of the hysteresis needs to be modeled. Due to increasing iron losses, the width of the hysteresis increases with increasing frequency, making an extension for dynamic operation necessary. Another point concerns the modeling effort in the magnetic circuit. In this work, leakage paths and parasitic air gaps have been neglected, resulting into modeling errors. In order to improve the estimation performance, such components in the magnetic path should be considered. Furthermore, it has been observed that the compensated characteristic of the actuator still shows ambiguities, making a combination of an inductance-based and parallel resistance-based estimator involving hysteresis compensation necessary.

Beside unmodeled physical effects, further works can be built on top of the already existing technique:

Combination with state observers

Similarly to self-sensing approaches in the field of electrical machines, a combination of the IDIM technique with a state observer seems desirable. Such a supervising observer could track the superimposed mechanical system, allowing for a robust estimation of the position. Furthermore, also the magnetic force and external load forces could be tracked.

Application on multi-phase actuators

With the discussed merits of the IDIM technique, an extension of the technique to multi-phase actuators such as (a)synchronous machines as well as stepper motors, seems plausible.

List of symbols

General

x, X	Quantities
$\mathbf{x}$	Vectors
$\mathbf{X}$	Matrices

Accents

$\tilde{\ }$	Error-affected quantities
$\bar{\ }$	Offset-removed quantities
$\hat{\ }$	Estimated quantities

Subscripts, can be combined

Δ	incremental
Σ, tot	summarized
0	initial condition
b	back-iron
e	eddy currents
h	hysteresis losses
p	plunger
s	series
x	air gap

Superscripts

$+$	Referred to the positive PWM voltage pulse, positive signal
$-$	Referred to the negative PWM voltage pulse, negative signal

Quantities

α	Duty cycle
δ	Dirac function
$\Delta i^+, \Delta i^-$	Current differences within PWM period
$\Delta t^+, \Delta t^-$	Time differences within PWM period
η	Coefficient of the Steinmetz law
Γ	Magnetic transfer function nominator polynomial
Λ	Electrical transfer function denominator polynomial
λ	SMC parameter
μ	Magnetic permeability
μ_0	Magnetic permeability in air
μ_d	Differential relative magnetic permeability
μ_r	Relative magnetic permeability
μ_{rev}	Reversible relative magnetic permeability
μ_s	Static relative magnetic permeability
ω	Helping variable for SMC
σ_{el}	Electrical conductivity
σ	Sliding Variable
σ^2	Variance
ϕ	Magnetic flux
Φ	External disturbance
Φ_1, Φ_2	Clocks for SC technology
ψ	Magnetic flux linkage
τ_{el}	Time constant of the electrical subsystem
τ_{HP}	High-pass filter time constant
τ_i	Time constant the current (controller) dynamics
τ_m	Time constant of the mechanical subsystem
τ_{th}	Time constant of the thermal subsystem
θ	Magneto-Motive Force
Θ	Heaviside step function
$\Theta_{x,y}$	Weighting gains for the neurons in the MLP
Υ	Magnetic transfer function denominator polynomial
Ξ	Electrical transfer function nominator polynomial
A	Matrix with integral measurements
A_{eff}	Effective cross section of a piece of magnetic material
B	Magnetic flux density

b	SMC parameter
b_i	Bias for the neurons in the MLP
c	Spring constant
C	Electromagnetic constant
C_0	Unit SC capacitor
C, C_1, C_2, C_{int}	Integration capacitances
C_{kl}	Coefficients of the polynomial fitting
C_p	Parallel capacitance
C_R	SC resistor capacitance
d	Damping coefficient
e	Coefficient of the Steinmetz law
e_i^+, e_i^-	Errors in the estimated current cusp height
f_C	SC frequency
f_{HP}	Cut-off frequency of the high-pass filter
F_m	Magnetic force
f_{pwm}	PWM frequency
g	Gravity constant
G	Measurement Gain
G_i	Gain error in current measurement
$G_{RC}, \Delta G_{RC}$	Gain error in the integrator
G_u	Gain error in voltage measurement
H	Magnetic Field Strength
h_i	Height of the current cusp
$\mathbf{H}_{r_H}$	Vector of play operator with thresholds r_S
i	Electrical current
i_d	Driving current
i_{FAR}	High-pass filtered and rectified current
i_{HP}	High-pass filtered current
$i_{mean}^+, i_{mean}^-, i_{mean}$	Mean value of current during PWM period
i_o	Offset error current
i_{ref}	Current reference
i_s^0	Mean value of the current ripple
L	Inductance
L	Lipschitz constant
$\mathcal{L}$	Magnetic inductance
l_{eff}	Effective length of a piece of magnetic material
L_s	Static inductance

m	Mass
M	Hysteresis model
n	Noise
N	Number of windings
n_c	Model order used for the eddy current model
n_i	Model order of the polynomial for the current
n_p	Model order of the polynomial for the self-sensing parameter
n_x	Model order of the polynomial for the position
P_n	Noise power
Q	Integral value of the IDIM technique
Q_o	Offset error in the integrator
r	Reset signal
$\mathcal{R}$	Magnetic reluctance
$\mathcal{R}_{\Delta Fe}$	Iron core reluctance
R_{eq}	Equal resistance
R_{int}	Integration resistance
$\mathcal{R}_l$	Magnetic reluctance representing leakage fluxes
R_p	Parallel resistance representing iron losses
$\mathcal{R}_\int$	Magnetic static reluctance
R_{shunt}	Shunt resistance
s	Laplace value
$\mathbf{S}_{r_s}$	Vector of superposition operators with thresholds r_S
T_C	SC time period
t_δ	Time delay for eddy current measurement
$t^+_{m1}, t^+_{m2}, t^-_{m1}, t^-_{m2}$	Time instants for eddy current measurement
t_{pwm}	PWM time period
t_r	Waiting time
$t^+_s, t^+_e, t^-_s, t^-_e$	Time instants within PWM period
u	Electrical voltage
u_C	Capacitor voltage
U_{DC}	DC link voltage
u_{dr}	Electrical driving voltage (from controller)
u_{ind}	Induced Voltage
u_{meas}	Measured voltage
u_{mean}	Mean voltage
u_{shunt}	Shunt voltage
u_o	Offset-error voltage

u_{off}	Offset voltage
u_{out}	Output voltage
v	Magnetic voltage
W_{mag}	Magnetic energy
$\mathbf{w}_s, \mathbf{w}_s^{'}$	Weights and inverse weights of the superposition operator
$\mathbf{w}_Z, \mathbf{w}_H^{'}$	Weights and inverse weights of the play operator
x	Position, air gap size
x_0	Position offset
x_{est}	Estimated position
x_{meas}	Measured position
x_{ref}	Position reference
$\mathcal{Z}$	Magnetic impedance
$\mathbf{z}_{H0}, \mathbf{z}_{H0}^{'}$	Initial and inverse initial conditions of the play operator

Bibliography

[1] S. Thompson, *Lectures on the Electromagnet* (Nineteenth Century Collections Online (NCCO): Science, Technology, and Medicine: 1780-1925). New York, NY, USA: W.J. Johnston Company, Limited, 1891, digitalized. [Online]. Available: `https://books.google.de/books?id=Ed0EAAAAYAAJ` (visited on 09/13/2023).

[2] E. Kallenbach, R. Eick, T. Ströhla, K. Feindt, M. Kallenbach, and O. Radler, *Elektromagnete: Grundlagen, Berechnung, Entwurf und Anwendung*, 5th ed. Wiesbaden, Germany: Springer Vieweg, 2017, OCLC: 1001340156, ISBN: 978-3-658-14788-4.

[3] I. Boldea, *Linear electric machines, drives, and maglevs handbook*. Boca Raton, FL, USA: CRC Press/Taylor & Francis Group, 2013, ISBN: 978-1-4398-4514-1.

[4] T. Kramer, J. Weber, G. Pflug, and B. Harnisch, “Intelligent Condition Monitoring of Bi-stable Process Valves,” in *Fluid power networks*, Aachen, Germany: RWTH, Mar. 2018, pp. 382–393. DOI: `10.18154/RWTH-2018-224801`.

[5] T. Kramer, M. Petzold, J. Weber, O. Ohligschläger, and A. Müller, “Smart control of electromagnetically driven dosing pumps,” Dresden, Germany, Mar. 2016, pp. 385–398.

[6] T. Kramer, J. Weber, G. Pflug, and B. Harnisch, “Investigations on Condition Monitoring and Potential Energy Savings of Bi-Stable Process Valves Using Position Estimation,” Sarasota, Florida, USA: American Society of Mechanical Engineers Digital Collection, Dec. 2017. DOI: `10.1115/FPMC2017-4272`.

[7] A. Gadyuchko, F. Bussinger, E. Kallenbach, and O. Radler, “Control concept for hysteresis free behaviour of proportional solenoid,” in *7th International Fluid Power Conference*, vol. 4, Aachen, Germany: Apprimus, 2010, pp. 509–522, ISBN: 978-3-940565-93-8.

[8] T. Braun, J. Reuter, and J. Rudolph, “Sensorlose Positionsregelung eines hydraulischen Proportional-Wegeventils mittels Signalinjektion,” *at - Automatisierungstechnik*, vol. 65, no. 4, 2017, ISSN: 0178-2312. DOI: `10.1515/auto-2017-0003`.

[9] S. Richter, *Ein Beitrag zur Integration von Maßnahmen der Funktionalen Sicherheit in einen geregelten elektrohydraulischen Antrieb für stationäre Anwendungen* (Fluidmechatronische Systeme), dissertation. Herzogenrath, Germany: Shaker, 2016, ISBN: 978-3-8440-4542-0.

[10] A. Espinosa, J.-R. Ruiz, J. Cusido, and X. Morera, “Sensorless Control and Fault Diagnosis of Electromechanical Contactors,” *IEEE Transactions on Industrial Electronics*, vol. 55, no. 10, pp. 3742–3750, 2008, ISSN: 0278-0046. DOI: `10.1109/TIE.2008.925773`.

[11] D. Schröder, *Elektrische Antriebe - Regelung von Antriebssystemen*, 4th ed. Heidelberg, Germany: Springer Vieweg, 2015, ISBN: 978-3-642-30096-7.

[12] O. Benjak and D. Gerling, “Review of position estimation methods for IPMSM drives without a position sensor part II: Adaptive methods,” in *The XIX International Conference on Electrical Machines - ICEM 2010*, Rome, Italy: IEEE, Sep. 2010. DOI: `10.1109/ICELMACH.2010.5607980`.

[13] O. Benjak and D. Gerling, “Review of Position Estimation Methods for PMSM Drives Without a Position Sensor, Part III: Methods based on Saliency and Signal Injection,” in *2010 International Conference on Electrical Machines and Systems*, Incheon, South Korea: IEEE, Oct. 2010.

[14] O. Benjak and D. Gerling, “Review of position estimation methods for IPMSM drives without a position sensor part I: Nonadaptive methods,” in *The XIX International Conference on Electrical Machines - ICEM 2010*, Rome, Italy: IEEE, Sep. 2010. DOI: `10.1109/ICELMACH.2010.5607978`.

[15] M. Schrödl, “Detection of the rotor position of a permanent magnet synchronous machine at standstill,” Pisa, Italy, 1988.

[16] M. Schrödl, *Sensorless control of A. C. machines* (Fortschritt-Berichte VDI : Reihe 21, Elektrotechnik ; 117), dissertation. Düsseldorf, Germany: VDI-Verl., 1992, vol. 117, ISBN: 978-3-18-141721-8.

[17] M. Schrödl, “Sensorless control of AC machines at low speed and standstill based on the "INFORM" method,” in *IAS ’96. Conference Record of the 1996 IEEE Industry Applications Conference Thirty-First IAS Annual Meeting*, vol. 1, San Diego, CA, USA: IEEE, Oct. 1996, pp. 270–277. DOI: `10.1109/IAS.1996.557028`.

[18] M. J. Corley and R. D. Lorenz, “Rotor position and velocity estimation for a permanent magnet synchronous machine at standstill and high speeds,” in *IAS ’96. Conference Record of the 1996 IEEE Industry Applications Conference Thirty-First IAS Annual Meeting*, vol. 1, Oct. 1996, 36–41 vol.1. DOI: `10.1109/IAS.1996.556994`.

[19] M. Linke, R. Kennel, and J. Holtz, “Sensorless position control of permanent magnet synchronous machines without limitation at zero speed,” in *IEEE 2002 28th Annual Conference of the Industrial Electronics Society. IECON 02*, vol. 1, Sevilla, Spain: IEEE, Nov. 2002, pp. 674–679. DOI: `10.1109/IECON.2002.1187588`.

[20] D. Paulus, P. Landsmann, and R. Kennel, “Sensorless field- oriented control for permanent magnet synchronous machines with an arbitrary injection scheme and direct angle calculation,” in *2011 Symposium on Sensorless Control for Electrical Drives*, Birmingham, United Kingdom: IEEE, Sep. 2011, pp. 41–46. DOI: `10.1109/SLED.2011.6051543`.

[21] P. Landsmann and R. K. Kennel, “Saliency-based sensorless predictive torque control with reduced torque ripple,” *IEEE Transactions on Power Electronics*, vol. 27, no. 10, pp. 4311–4320, Oct. 2012, ISSN: 0885-8993. DOI: `10.1109/TPEL.2012.2192137`.

[22] M. Balakrishnan and N. Kumar N, “Detection of Plunger Movement in DC Solenoids,” Texas Instruments, Bangalore, India, Tech. Rep., 2015. [Online]. Available: `https://www.ti.com/lit/pdf/ssiy001` (visited on 09/11/2023).

[23] M. Koteich, "Flux estimation algorithms for electric drives: A comparative study," in *2016 3rd International Conference on Renewable Energies for Developing Countries (REDEC)*, Zouk Mosbeh, Lebanon: IEEE, Jul. 2016, pp. 1–6. DOI: `10.1109/REDEC.2016.7577558`.

[24] G. Bergstrom, "System to Determine Solenoid Position and Flux Without Drift," US6300733B1, Oct. 2001. [Online]. Available: `https://patents.google.com/patent/US6300733B1/en` (visited on 09/12/2023).

[25] H. Q. Nguyen, "Observer-Based Tracking Control for Polysolenoid Linear Motor with Unknown Disturbance Load," *Actuators*, vol. 9, no. 1, p. 23, 2020, ISSN: 2076-0825. DOI: `10.3390/act9010023`.

[26] A. Szabo, T. Becsi, P. Gaspar, and S. Aradi, "State estimation of an electro-pneumatic gearbox actuator," *IFAC-PapersOnLine*, vol. 52, no. 5, pp. 329–334, 2019, ISSN: 24058963. DOI: `10.1016/j.ifacol.2019.09.053`.

[27] P. B. Eyabi, "Modeling and sensorless control of solenoidal acutators," dissertation, The Ohio State University, Columbo, Ohio, USA, 2003. [Online]. Available: `https://rave.ohiolink.edu/etdc/view?acc_num=osu1054142598` (visited on 09/12/2023).

[28] T. Braun, M. Schwab, F. Strausberger, and J. Reuter, "State estimation for fast-switching solenoid valves - A Nonlinear sliding-mode-observer approach," in *2014 19th International Conference on Methods and Models in Automation and Robotics (MMAR)*, Miedzyzdroje: IEEE, Sep. 2014, pp. 282–287. DOI: `10.1109/MMAR.2014.6957365`.

[29] T. Braun, F. Strausberger, and J. Reuter, "State estimation for fast-switching solenoid valves: A study on practical nonlinear observers and new experimental results," in *2015 20th International Conference on Methods and Models in Automation and Robotics (MMAR)*, Miedzyzdroje, Poland: IEEE, Aug. 2015, pp. 862–867. DOI: `10.1109/MMAR.2015.7283990`.

[30] T. Braun and J. Reuter, "Sliding Mode Observation with Iterative Parameter Adaption for Fast-Switching Solenoid Valves," in *Variable-Structure Approaches*, A. Rauh and L. Senkel, Eds., Cham, Germany: Springer International Publishing, 2016, pp. 189–212. DOI: `10.1007/978-3-319-31539-3_7`.

[31] T. Braun, J. Reuter, and J. Rudolph, "Observer Design for Self-Sensing of Solenoid Actuators With Application to Soft Landing," *IEEE Transactions on Control Systems Technology*, vol. 27, pp. 1720–1727, 2018, ISSN: 1063-6536. DOI: `10.1109/TCST.2018.2821656`.

[32] T. Braun, *Ein Beitrag zum Beobachterentwurf und zur sensorlosen Folgeregelung translatorischer Magnetaktoren* (Schriftenreihe der Institute für Systemdynamik (ISD) und optische Systeme (IOS)), dissertation. Wiesbaden, Germany: Springer Vieweg, 2020, ISBN: 978-3-658-29248-5.

[33] L. Ljung, *System Identification - Theory for the User*, 2nd ed. NJ, USA: Prentice Hall, 1999, ISBN: 0-13-656695-2.

[34] L. Kučera, "Zur sensorlosen Magnetlagerung," dissertation, Eigenössische Technische Hochschule Zürich, Zürich, Switzerland, 1997. [Online]. Available: `https://www.ifr.mavt.ethz.ch/publications/kucera97b.pdf` (visited on 09/12/2023).

[35] I. Dülk and T. Kovácsházy, "Modelling of a linear proportional electromagnetic actuator and possibilities of sensorless plunger position estimation," in *2011 12th International Carpathian Control Conference (ICCC)*, Velke Karlovice, Czech Republic, May 2011, pp. 89–93. DOI: `10.1109/CarpathianCC.2011.5945822`.

[36] J. Maridor, "Design, Optimization, and Sensorless Control of a Linear Actuator," dissertation, École Polytechnique Fédérale de Lausanne, Lausanne, Switzerland, 2011. [Online]. Available: `https://doi.org/10.5075/epfl-thesis-5187` (visited on 09/12/2023).

[37] I. Dülk and T. Kovácsházy, "A Sensorless Method for Detecting Spool Position in Solenoid Actuators," *Carpathian Journal of Electronic and Computer Engineering*, vol. 6, no. 1, pp. 36–43, 2013, ISSN: 1844-9689.

[38] T. Braun, J. Reuter, and J. Rudolph, "Position Observation for Proportional Solenoid Valves by Signal Injection," *IFAC-PapersOnLine*, vol. 49, no. 21, pp. 74–79, 2016, ISSN: 24058963. DOI: `10.1016/j.ifacol.2016.10.513`.

[39] A. E. Hafni, M. Abdelrahem, and R. Kennel, "Position estimation for linear electromagnetic actuators," in *2017 IEEE International Symposium on Sensorless Control for Electrical Drives (SLED)*, Catania, Italy: IEEE, Sep. 2017, pp. 219–224. DOI: `10.1109/SLED.2017.8078453`.

[40] G. Schweitzer and E. H. Maslen, Eds., *Magnetic bearings: theory, design, and application to rotating machinery.* Berlin Heidelberg, Germany: Springer, 2009, ISBN: 978-3-642-10153-3.

[41] M. Rahman, N. Cheung, and K. Lim, "A sensorless position estimator for a nonlinear solenoid actuator," in *Proceedings of IECON '95 - 21st Annual Conference on IEEE Industrial Electronics*, vol. 2, Orlando, FL, USA: IEEE, 1995, pp. 1208–1213. DOI: `10.1109/IECON.1995.483969`.

[42] M. Rahman, N. Cheung, and K. W. Lim, "Position estimation in solenoid actuators," *IEEE Transactions on Industry Applications*, vol. 32, no. 3, pp. 552–559, May 1996, ISSN: 1939-9367. DOI: `10.1109/28.502166`.

[43] D. Pawelczak and H.-R. Tränkler, "Sensorless position/force control of electromagnetic linear actuator," in *Proceedings of the 13th International Symposium CSIC/AIA*, Madrid, Spain, 2003, ISBN: 84-607-9693-0.

[44] D. Pawelczak and H.-R. Trankler, "Sensorless position control of electromagnetic linear actuator," in *Proceedings of the 21st IEEE Instrumentation and Measurement Technology Conference*, Como, Italy, May 2004, pp. 372–376. DOI: `10.1109/IMTC.2004.1351066`.

[45] D. Pawelczak, *Nutzung inhärenter Messeffekte von Aktoren und Methoden zur sensorlosen Positionsmessung im Betrieb* (Berichte aus der Steuerungs- und Regelungstechnik), dissertation. Aachen, Germany: Shaker, 2005, ISBN: 978-3-8322-4184-1.

[46] J.-C. Renn and Y.-S. Chou, "Sensorless Plunger Position Control for a Switching Solenoid," *JSME International Journal Series C*, vol. 47, no. 2, pp. 637–645, 2004, ISSN: 1347-538X. DOI: `10.1299/jsmec.47.637`.

[47] T. Kamf and J. Abrahamsson, "Self-Sensing Electromagnets for Robotic Tooling Systems: Combining Sensor and Actuator," *Machines*, vol. 4, no. 3, p. 16, Aug. 2016, ISSN: 2075-1702. DOI: `10.3390/machines4030016`.

[48] T. Glück, W. Kemmetmüller, A. Kugi, and C. Tump, "Measurement errors analysis for a position estimator for self-sensing magnetic levitation systems," in *Proceedings of VDI Mechatronik 2011*, Dresden, Germany, Mar. 2011.

[49] T. Glück, W. Kemmetmüller, C. Tump, and A. Kugi, "A novel robust position estimator for self-sensing magnetic levitation systems based on least squares identification," *Control Engineering Practice*, vol. 19, no. 2, pp. 146–157, 2011, ISSN: 09670661. DOI: `10.1016/j.conengprac.2010.11.003`.

[50] I. Dülk and T. Kovácsházy, "Sensorless position estimation in solenoid actuators with load compensation," in *2012 IEEE International Instrumentation and Measurement Technology Conference Proceedings*, Graz, Austria: IEEE, May 2012, pp. 268–273. DOI: `10.1109/I2MTC.2012.6229339`.

[51] T. Glück, *Soft landing and self-sensing strategies for electromagnetic actuators* (Modellierung und Regelung komplexer dynamischer Systeme 18), dissertation. Aachen, Germany: Shaker, 2013, ISBN: 978-3-8440-2428-9.

[52] I. Dülk and T. Kovácsházy, "Resistance Estimation in Solenoid Actuators by Considering Different Resistances in the PWM Paths," *Periodica Polytechnica Electrical Engineering and Computer Science*, vol. 58, no. 3, pp. 109–120, 2014, ISSN: 20645279. DOI: `10.3311/PPee.7353`.

[53] S. Ahmed, Van-Duc Doan, and T. Koseki, "Electromagnetic levitation control with sensorless large air gap detection for translational motion application using measured current-ripple slope," in *IECON 2016 - 42nd Annual Conference of the IEEE Industrial Electronics Society*, Florence, Italy: IEEE, Oct. 2016, pp. 4275–4280. DOI: `10.1109/IECON.2016.7793418`.

[54] M. Noh, "Self-Sensing Magnetic Bearings Driven by a Switching Power Amplifier," dissertation, University of Virginia, Virginia, USA, 1996. [Online]. Available: `https://www.proquest.com/openview/7073a62dffab3073359cd5ef2f74bca7/1?pq-origsite=gscholar&cbl=18750&diss=y` (visited on 09/12/2023).

[55] M. Noh and E. Maslen, "Self-sensing magnetic bearings using parameter estimation," *IEEE Transactions on Instrumentation and Measurement*, vol. 46, no. 1, pp. 45–50, 1997, ISSN: 00189456. DOI: `10.1109/19.552155`.

[56] F. Straussberger, M. Schwab, T. Braun, and J. Reuter, "New results for position estimation in electro-magnetic actuators using a modified discrete time class A/B model reference approach," in *2014 19th International Conference on Methods and Models in Automation and Robotics (MMAR)*, Miedzyzdroje, Poland: IEEE, Sep. 2014, pp. 229–234. DOI: `10.1109/MMAR.2014.6957356`.

[57] F. Straussberger, M. Schwab, T. Braun, and J. Reuter, “Position estimation in electro-magnetic actuators using a modified discrete time class A/B model reference approach,” in *2014 American Control Conference*, Portland, OR, USA: IEEE, Jun. 2014, pp. 3686–3691. DOI: `10.1109/ACC.2014.6858841`.

[58] E. Ramirez-Laboreo, M. G. L. Roes, and C. Sagues, “Hybrid Dynamical Model for Reluctance Actuators Including Saturation, Hysteresis, and Eddy Currents,” *IEEE/ASME Transactions on Mechatronics*, vol. 24, no. 3, pp. 1396–1406, 2019, ISSN: 1941-014X. DOI: `10.1109/TMECH.2019.2906755`.

[59] I. MacKenzie and D. L. Trumper, “Real-Time Hysteresis Modeling of a Reluctance Actuator Using a Sheared-Hysteresis-Model Observer,” *IEEE/ASME Transactions on Mechatronics*, vol. 21, no. 1, pp. 4–16, 2016, ISSN: 1941-014X. DOI: `10.1109/TMECH.2015.2513769`.

[60] F. Straußberger and J. Reuter, “Position Estimation in Electro-Magnetic Actuators Taking into Account Hysteresis Effects,” *IFAC-PapersOnLine*, vol. 49, no. 21, pp. 206–212, 2016, ISSN: 24058963. DOI: `10.1016/j.ifacol.2016.10.549`.

[61] T. Kramer and J. Weber, “Self-Sensing Design of Proportional Solenoids,” Virtual, Online: American Society of Mechanical Engineers Digital Collection, Oct. 2020. DOI: `10.1115/FPMC2020-2811`.

[62] T. Kramer and J. Weber, “Self-Sensing position determination on a sensor-designed proportional solenoid,” in *Volume 3 - Conference*, Dresden, Germany: Technische Universität Dresden, Jun. 2020, pp. 269–280. DOI: `10.25368/2020.115`.

[63] E. Ranft, G. van Schoor, and C. d. Rand, “Self-sensing for electromagnetic actuators. Part II: Position estimation,” *Sensors and Actuators A: Physical*, vol. 172, no. 2, pp. 410–419, 2011, ISSN: 09244247. DOI: `10.1016/j.sna.2011.09.037`.

[64] M. D. Noh, D. Montie, E. H. Maslen, and A. Kondoleon, “A Simulation Model for the Analysis of Transient Magnetic Bearing Performance,” in *The Seventh International Symposium on Magnetic Bearings*, Zürich, Switzerland: International Center for Magnetic Bearings, Aug. 2000, pp. 177–182. [Online]. Available: `https://infoscience.epfl.ch/record/97422` (visited on 09/12/2023).

[65] N. König, M. Nienhaus, and E. Grasso, “Analysis of Current Ripples in Electromagnetic Actuators with Application to Inductance Estimation Techniques for Sensorless Monitoring,” *Actuators*, vol. 9, no. 1, Mar. 2020, ISSN: 2076-0825. DOI: `10.3390/act9010017`.

[66] N. König and M. Nienhaus, “A Solution to Ambiguities in Position Estimation for Solenoid Actuators by Exploiting Eddy Current Variations,” *Sensors*, vol. 20, no. 12, p. 3441, Jun. 2020, ISSN: 1424-8220. DOI: `10.3390/s20123441`.

[67] N. Koenig, E. Grasso, D. Merl, and M. Nienhaus, “A Position Estimation Method for Single-Phase Electrical Machines Without Injecting Extra Test Pulses,” in *2018 IEEE 9th International Symposium on Sensorless Control for Electrical Drives (SLED)*, Helsinki, Finland, Sep. 2018, pp. 42–47. DOI: `10.1109/SLED.2018.8485843`.

[68] N. König, E. Grasso, and M. Nienhaus, “Sensorless Closed-Loop Control of Solenoid Actuators Using IDIM Technique,” in *2018 AEIT International Annual Conference*, Bari, Italy: IEEE, Oct. 2018, pp. 1–6. DOI: `10.23919/AEIT.2018.8577452`.

[69] E. Grasso, N. König, M. Nienhaus, and D. Merl, “Method and device for determining inductivity of an electromagnetic actuator,” EP3544173A1, Sep. 2019. [Online]. Available: `https://patents.google.com/patent/EP3544173A1/en?oq=EP3544173` (visited on 09/12/2021).

[70] N. Koenig, G. Anzelmi, D. Naso, M. Nienhaus, and E. Grasso, “An Improved IDIM Technique for Sensorless Control of Single-Phase Electromagnetic Drives,” in *2019 IEEE 10th International Symposium on Sensorless Control for Electrical Drives (SLED)*, Turin, Italy: IEEE, Sep. 2019, pp. 1–6. DOI: `10.1109/SLED.2019.8896303`.

[71] N. König, Y. Carbon, M. Nienhaus, and E. Grasso, “A Self-Sensing Method for Electromagnetic Actuators with Hysteresis Compensation,” *Energies*, vol. 14, no. 20, p. 6706, Oct. 2021, ISSN: 1996-1073. DOI: `10.3390/en14206706`.

[72] T. Ströhla, *Ein Beitrag zur Simulation und zum Entwurf von elektromagnetischen Systemen mit Hilfe der Netzwerkmethode*, dissertation. Ilmenau, Germany: Wissenschaftsverlag Ilmenau, 2002, ISBN: 3-936404-00-3.

[73] H. C. Roters, *Electromagnetic Devices.* New York, NY, USA: John Wiley & Sons Inc, Dec. 1941, ISBN: 978-0-471-73920-3.

[74] J. R. Brauer, *Magnetic actuators and sensors.* Hoboken, N.J, USA: Wiley, 2006, ISBN: 978-0-471-73169-6.

[75] E. Ivers-Tiffée and W. v. Münch, *Werkstoffe der Elektrotechnik: mit 40 Tabellen* (Lehrbuch Elektrotechnik), 10th ed. Wiesbaden, Germany: Teubner, 2007, ISBN: 978-3-8351-0052-7.

[76] G. Fasching, H. Hauser, and W. Smetana, *Werkstoffe für die Elektrotechnik. Hauptbd: Mikrophysik, Struktur, Eigenschaften*, 4th ed. Wien, Austria: Springer, 2005, ISBN: 978-3-211-22133-4.

[77] R. M. Bozorth, *Ferromagnetism.* Piscataway, N.J, USA: IEEE Press, 1993, ISBN: 978-0-7803-1032-2.

[78] K. Küpfmüller, W. Mathis, and A. Reibiger, *Theoretische Elektrotechnik: elektromagnetische Felder, Schaltungen und elektronische Bauelemente*, 20th ed. Berlin, Germany: Springer Vieweg, 2017, OCLC: 987574947, ISBN: 978-3-662-54837-0.

[79] P. Guillery, *Werkstoffkunde für Elektroingenieure*, 3rd ed. Wiesbaden, Germany: Vieweg+Teubner Verlag, 1974, ISBN: 978-3-528-23508-6. DOI: `10.1007/978-3-322-86420-8`.

[80] G. Bertotti, *Hysteresis in magnetism: for physicists, materials scientists, and engineers.* San Diego, CA, USA: Academic Press, 1998, ISBN: 978-0-12-093270-2.

[81] T. Chevalier, A. Kedous-Lebouc, B. Cornut, and C. Cester, “A new dynamic hysteresis model for electrical steel sheet,” *Physica B: Condensed Matter*, vol. 275, no. 1-3, pp. 197–201, 2000, ISSN: 09214526. DOI: `10.1016/S0921-4526(99)00768-1`.

[82] M. Ranta, M. Hinkkanen, E. Dlala, A.-K. Repo, and J. Luomi, "Inclusion of hysteresis and eddy current losses in dynamic induction machine models," in *2009 IEEE International Electric Machines and Drives Conference*, Miami, FL, USA: IEEE, May 2009, pp. 1387–1392. DOI: `10.1109/IEMDC.2009.5075384`.

[83] L. Chua and K. Stromsmoe, "Lumped-circuit models for nonlinear inductors exhibiting hysteresis loops," *IEEE Transactions on Circuit Theory*, vol. 17, no. 4, pp. 564–574, 1970, ISSN: 0018-9324. DOI: `10.1109/TCT.1970.1083192`.

[84] J. Lunze, *Regelungstechnik. 1: Systemtheoretische Grundlagen, Analyse und Entwurf einschleifiger Regelungen*, 12th ed. Berlin Heidelberg, Germany: Springer Vieweg, 2020, ISBN: 978-3-662-60745-9.

[85] E. Fraga, C. Prados, and D.-X. Chen, "Practical model and calculation of AC resistance of long solenoids," *IEEE Transactions on Magnetics*, vol. 34, no. 1, pp. 205–212, 1998, ISSN: 00189464. DOI: `10.1109/20.650232`.

[86] D. Meeker, E. Maslen, and M. Noh, "An augmented circuit model for magnetic bearings including eddy currents, fringing, and leakage," *IEEE Transactions on Magnetics*, vol. 32, no. 4, pp. 3219–3227, 1996, ISSN: 00189464. DOI: `10.1109/20.508385`.

[87] M. Michel, *Leistungselektronik: Einführung in Schaltungen und deren Verhalten*, 5th ed. Berlin Heidelberg, Germany: Springer, 2011, ISBN: 978-3-642-15983-1.

[88] R. Mancini, *Op amps for everyone: design reference*, 2nd ed. Boston, USA: Newnes, 2003, ISBN: 978-0-7506-7701-1.

[89] N. König, E. Grasso, and M. Nienhaus, "Robust Electrical and Mechanical Parameter Identification of Low-Power PMSMs," in *Innovative Small Drives and Micro-Motor Systems; 11th GMM/ETG-Symposium*, Saarbrücken, Germany, Sep. 2017, pp. 1–6, ISBN: 978-3-8007-4461-9.

[90] N. König, E. Grasso, K. Schuhmacher, and M. Nienhaus, "Parameter identification of star-connected PMSMs by means of a sensorless technique," in *2018 Thirteenth International Conference on Ecological Vehicles and Renewable Energies (EVER)*, Monte-Carlo, Monaco, Apr. 2018, pp. 1–7. DOI: `10.1109/EVER.2018.8362359`.

[91] ARM, *Cortex-M4 instructions*. [Online]. Available: `https://developer.arm.com/documentation/ddi0439/b/CHDDIGAC` (visited on 03/26/2023).

[92] T. Kleineberg, *Modellierung nichtlinearer induktiver Bauelemente der Leistungselektronik* (Fortschritt-Berichte VDI Reihe 20, Rechnerunterstützte Verfahren 161), dissertation. Düsseldorf, Germany: VDI-Verl, 1995, ISBN: 978-3-18-316120-1.

[93] S. Agarlita, I. Boldea, F. Marignetti, and L. Tutelea, "Position sensorless control of a linear interior permanent magnet oscillatory machine, with experiments," in *2010 12th International Conference on Optimization of Electrical and Electronic Equipment*, Brasov, Romania: IEEE, May 2010, pp. 689–695. DOI: `10.1109/OPTIM.2010.5510567`.

[94] C. A. Hudson, N. S. Lobo, and R. Krishnan, "Sensorless Control of Single Switch-Based Switched Reluctance Motor Drive Using Neural Network," *IEEE Transactions on Industrial Electronics*, vol. 55, no. 1, pp. 321–329, 2008, ISSN: 0278-0046. DOI: `10.1109/TIE.2007.903965`.

[95] D. Schröder, *Intelligente Verfahren: Identifikation und Regelung nichtlinearer Systeme*, 1st ed. Berlin, Germany: Springer, 2010, ISBN: 978-3-642-11398-7.

[96] O. Nelles, *Nonlinear system identification: from classical approaches to neural networks and fuzzy models*. New York, NY, USA: Springer, 2001, ISBN: 978-3-540-67369-9.

[97] S. Rosenbaum, *Entwurf elektromagnetischer Aktoren unter Berücksichtigung von Hysterese* (Ilmenauer Schriften zur Mechatronik 2), dissertation. Ilmenau, Germany: Univ.-Verl. Ilmenau, 2011, ISBN: 978-3-86360-008-2.

[98] C.-D. Munz and T. Westermann, *Numerische Behandlung gewöhnlicher und partieller Differenzialgleichungen: ein interaktives Lehrbuch für Ingenieure*. Berlin Heidelberg, Germany: Springer, 2006, ISBN: 978-3-540-29867-0.

[99] K. Kuhnen, *Kompensation komplexer gedächtnisbehafteter Nichtlinearitäten in Systemen mit aktiven Materialien: Grundlagen - Erweiterte Methoden - Anwendungen* (Berichte aus der Steuerungs- und Regelungstechnik), habilitation thesis. Aachen, Germany: Shaker, 2008, ISBN: 978-3-8322-7610-2.

[100] K. Kuhnen, "Modeling, Identification and Compensation of Complex Hysteretic Nonlinearities: A Modified Prandtl-Ishlinskii Approach," *European Journal of Control*, vol. 9, no. 4, pp. 407–418, Jan. 2003, ISSN: 09473580. DOI: `10.3166/ejc.9.407-418`.

[101] J. Karki, *Fully-Differential Amplifiers*, Rev. E. Dallas, Texas, USA: Texas Instruments, 2016. [Online]. Available: `https://www.ti.com/lit/pdf/sloa054` (visited on 09/13/2023).

[102] B. Razavi, *Design of analog CMOS integrated circuits* (McGraw-Hill series in electrical and computer engineering), 1st. ed. Boston, USA: McGraw-Hill, 2000, ISBN: 978-0-07-118815-9.

[103] A. S. Sedra and K. C. Smith, *Microelectronic circuits* (The Oxford series in electrical and computer engineering), 4th ed. New York, NY, USA: Oxford University Press, 1998, ISBN: 978-0-19-511663-2.

[104] N. Koenig, A. Stanitzki, M. Nienhaus, and E. Grasso, "An Integrated Fast Resettable Integrator Circuit based on Switched Capacitors for Sensorless Control of PMSMs," in *IKMT 2022; 13. GMM/ETG-Symposium*, Linz, Austria, 2022, pp. 1–6, ISBN: 978-3-8007-5938-5.

[105] Anadigm, *AN231E04 Datasheet Rev 1.2 - Dynamically Reconfigurable dpASP*. [Online]. Available: `https://www.anadigm.com/_doc/ds231000-u001.pdf` (visited on 09/12/2023).

[106] Physik Instrumente (PI) GmbH, *M-403 Linear Stage*. [Online]. Available: `https://www.physikinstrumente.com/en/products/linear-stages/stages-with-stepper-dc-brushless-dc-bldc-motors/m-403-precision-translation-stage-701750/` (visited on 12/16/2019).

[107] Analog Devices, *AD8418 Datasheet and Product Info | Analog Devices*. [Online]. Available: `https://www.analog.com/en/products/ad8418.html#` (visited on 12/16/2019).

[108] R. Kieser, P. Reynisson, and T. J. Mulligan, "Definition of signal-to-noise ratio and its critical role in split-beam measurements," *ICES Journal of Marine Science*, vol. 62, no. 1, pp. 123–130, 2005, ISSN: 1095-9289. DOI: `10.1016/j.icesjms.2004.09.006`.

[109] Magnet-Schultz Memmingen, *Single acting solenoids type G TC A*. [Online]. Available: `https://www.magnet-schultz.com/en/solenoids/single-acting-solenoids-type-g-tc-a/` (visited on 12/16/2019).

[110] Red Magnetics, *ITS-LZ 1949-Z*. [Online]. Available: `https://red-magnetics.com/de/produktgruppen/hubmagnete/zylindermagnete/its-lz-1949-z/` (visited on 03/24/2020).

[111] L. Li, T. Shinshi, and A. Shimokohbe, "State Feedback Control for Active Magnetic Bearings Based on Current Change Rate Alone," *IEEE Transactions on Magnetics*, vol. 40, no. 6, pp. 3512–3517, 2004, ISSN: 0018-9464. DOI: `10.1109/TMAG.2004.836295`.

[112] TDK, *Ferrites and accessories - PM 87/70 - Core and accessories*. [Online]. Available: `https://www.tdk-electronics.tdk.com/inf/80/db/fer/pm_87_70.pdf` (visited on 09/12/2023).

[113] Y. Shtessel, C. Edwards, L. Fridman, and A. Levant, *Sliding mode control and observation* (Control Engineering). New York, NY, USA: Birkhauser, 2013, ISBN: 978-0-8176-4892-3.